

Liouvillian interpolation of the self-energy of cluster dynamical mean-field theories

Mathias Pelz,^{1,*} Jan von Delft,^{1,†} and Andreas Gleis^{2,‡}

¹*Arnold Sommerfeld Center for Theoretical Physics, Center for NanoScience, and Munich Center for Quantum Science and Technology, Ludwig-Maximilians-Universität München, 80333 Munich, Germany*

²*Department of Physics and Astronomy and Center for Condensed Matter Theory, Rutgers University, Piscataway, New Jersey 08854-8019, USA*

(Dated: February 19, 2026)

Two widely-used non-local extensions of dynamical mean field theory (DMFT), cellular DMFT (CDMFT) and the dynamical cluster approximation (DCA), both yield self-energies marred by having some unphysical properties: CDMFT yields real-space self-energies that are not translationally invariant, and DCA yields momentum-space self-energies with discontinuities in their momentum dependence. It is often desirable to remove these flaws by post-processing cluster DMFT results, using strategies called periodization for CDMFT and interpolation for DCA—for brevity, we refer to both cases as *interpolation*. However, traditional interpolation approaches struggle to capture intricate structures such as hole pockets in the hole-doped square-lattice Hubbard model, as highlighted in *Phys. Rev. B* **105**, 35117 (2022). Further, these approaches interpolate frequency-dependent functions, which may lead to causality violations. Here, we propose *Liouvillian interpolation*, a novel, intuitive, and robust scheme for interpolating cluster DMFT results. Our key idea is to interpolate frequency-*independent* matrix elements of the single-particle irreducible part of the Liouvillian, obtained from a continued-fraction expansion of the cDMFT self-energy. We demonstrate that the ingredients of such an expansion possess a more local Fourier expansion than the functions involved in traditional interpolation schemes, and that Liouvillian interpolation inherently conserves causality. We illustrate our method for the one-dimensional Hubbard model using CDMFT, and for the two-dimensional Hubbard model using four-patch DCA. For the latter, we find that \mathcal{L} -interpolation can (depending on doping) yield Fermi and Luttinger arcs which together form a closed surface.

DOI:

I. INTRODUCTION

Cluster dynamical mean-field theories (cDMFT) [1–14] are commonly used to describe strong but short-ranged non-local correlations beyond single-site dynamical mean-field theory (DMFT) [15]. They effectively capture strongly correlated phenomena that may be driven by short-ranged correlations, such as the pseudogap phase in cuprates [5, 11, 12, 16–20], certain types of heavy-fermion quantum criticality [21–23], strange metals [24–27], Hund’s coupling [28, 29] or multi-orbital systems [30, 31].

The most commonly used cDMFT methods are cellular DMFT (CDMFT) [2], which couples a real-space cluster of sites to self-consistent baths, thereby breaking translation symmetry; and the dynamical cluster approximation (DCA) [3, 4], which coarse-grains the Brillouin zone into patches and couples these to self-consistent baths, thereby introducing artificial discontinuities in momentum space. The lack of periodicity for CDMFT results (implying real-space discontinuities) and the lack of a smooth momentum dependence for DCA results are unphysical. Removing these flaws requires the cDMFT results to be post-processed. CDMFT results have to be periodized to restore real-space translational invariance;

loosely speaking, this amounts to interpolating across cluster boundaries to remove the real-space discontinuities associated with non-periodic behavior. DCA results have to be interpolated across DCA patch boundaries to restore a smooth momentum dependence [1, 8–12, 14]. For brevity, we will use “interpolation” as an umbrella term for both CDMFT periodization and DCA interpolation. It is to be understood that in the context of CDMFT, “interpolation” refers to “periodization”.

In this work, we will focus on interpolating the single-particle Green’s function, G , and related quantities like the self-energy, Σ , and the cumulant, M . In the momentum/frequency representation, they are related by

$$G_{\mathbf{k}}(\omega) = \frac{1}{\omega + \mu - \epsilon_{\mathbf{k}} - \Sigma_{\mathbf{k}}(\omega)}, \quad (1a)$$

$$M_{\mathbf{k}}(\omega) = \frac{1}{\omega + \mu - \Sigma_{\mathbf{k}}(\omega)}. \quad (1b)$$

Instead of G , Σ or M , we will generically write Q for the quantity to be interpolated. In general, $Q_{\mathbf{k}}$ and $\tilde{Q}_{\mathbf{r}}$, the momentum and position representations of Q , are related by a Fourier transformation. However, approximate methods such as CDMFT or DCA yield $\tilde{Q}_{\mathbf{r}}$ only for a limited range of \mathbf{r} values, say with $|\mathbf{r}| \leq R$, where the distance cutoff R is determined by the cluster size (for CDMFT) or the number of momentum patches (for DCA). Thus, interpolation schemes amount to approxi-

* mathias.pelz@lmu.de

† vondelft@lmu.de

‡ andreas.gleis@rutgers.edu

mating $Q_{\mathbf{k}}$ by a *truncated* Fourier Ansatz,

$$Q_{\mathbf{k}}(\omega) \simeq \sum_{\mathbf{r}, |\mathbf{r}| \leq R} \bar{Q}_{\mathbf{r}}(\omega) e^{-i\mathbf{k} \cdot \mathbf{r}}. \quad (2)$$

Here, $\bar{Q}_{\mathbf{r}}$ has to be estimated from quantities computed on the cluster (for CDMFT) or the Brillouin zone patches (for DCA). In the case of CDMFT, commonly used schemes for this purpose are superlattice averaging [11] or center-focused extrapolation [32]. Other related quantities are then derived from Q ; for example, when Σ is interpolated via Eq. (2), that also determines G and M .

It is common knowledge among practitioners of cDMFT that the quality and reliability of the interpolation scheme is quite sensitive to the choice of Q . A particularly striking example was recently pointed out by Verret *et al.* [33]. They analyzed the limitations of existing choices for Q in the context of a long-standing question on the pseudogap phase of underdoped cuprates: Does the Fermi surface exhibit hole or electron pockets, as deduced from various transport experiments [34, 35], or disconnected Fermi arcs, as indicated by angle-resolved photoemission spectroscopy (ARPES) [36, 37]? Verret *et al.* [33] have argued that “contrary to previous claims [11, 12, 16, 38], cDMFT schemes cannot discriminate between Fermi arcs and hole pockets” (with the implication that previous cDMFT work attempting to answer the aforementioned question is inconclusive). They illustrated this for a Yang-Rice-Zhang (YRZ) [39] toy-model self-energy with built-in hole pockets: when they approximated its self-energy in CDMFT fashion and then periodized it, their M - and G -periodization schemes both yielded Fermi arcs [33] instead of reproducing the hole pockets. Verret *et al.* argued that this failure is due to “neglecting the self-energy between clusters”. They then presented a so-called *compact tiling* scheme that includes estimates of these neglected parts, see Ref. 33 for details. For the YRZ toy model, compact tiling successfully recovers the expected hole pockets. However, their scheme was formulated in a manner not applicable to general cDMFT calculations.

The fact that the quality of interpolated cDMFT results depends strongly on the choice of Q can be expected on general grounds. In Eq. (2), the Fourier truncation at $|\mathbf{r}| \leq R$ introduces errors. To limit these, it is preferable for $\bar{Q}_{\mathbf{r}}(\omega)$ to have (i) a short-ranged dependence on \mathbf{r} , and (ii) a weak (or no) dependence on ω . Different choices for Q satisfy these criteria to different degrees, leading to errors of differing severity. Regarding (ii), we note that if $\bar{Q}_{\mathbf{r}}(\omega)$ does depend significantly on ω , then the truncation of the Fourier series can cause unintended (even unacceptable) modifications in the analytic structure of $Q_{\mathbf{k}}(\omega)$. An example is Σ -interpolation: if $\tilde{\Sigma}_{\mathbf{r}}(\omega)$ depends strongly on ω , the truncation to $|\mathbf{r}| \leq R$ can cause $\text{Im}\Sigma_{\mathbf{k}}(\omega)$ to become positive for some values of ω and \mathbf{k} , implying a violation of causality for $G_{\mathbf{k}}(\omega)$ [10, 38].

In this paper, we propose the Liouvillian, \mathcal{L} , as a new and previously unexplored quantity for interpolation (i.e. we choose $Q = \mathcal{L}$). Our scheme, which we

call \mathcal{L} -interpolation, is based on a general, exact relation between the self-energy and the Liouvillian: if the self-energy is expressed through a continued-fraction expansion (CFE), its CFE coefficients are matrix elements of the single-particle irreducible part of the Liouvillian in a Krylov space obtainable via a Lanczos scheme. For a lattice model, these matrix elements are generically translation-invariant and smooth functions of \mathbf{k} . However, when Liouvillian matrix elements are extracted from the CFE expansion of a self-energy computed using CDMFT or DCA, they either do not satisfy translation invariance or exhibit discontinuities in \mathbf{k} -space, respectively. Our \mathcal{L} -interpolation scheme restores translation invariance or smooth \mathbf{k} -dependence by interpolating the single-particle irreducible Liouvillian matrix elements obtained from CDMFT or DCA self-energies, respectively: using superlattice averaging [11] for CDMFT or a self-consistency condition for DCA, respectively, we obtain estimates for the matrix elements of $\tilde{\mathcal{L}}_{\mathbf{r}}$, and insert these into the truncated Fourier ansatz (2) for $\mathcal{L}_{\mathbf{k}}$. The resulting matrix elements of $\mathcal{L}_{\mathbf{k}}$ serve as interpolated CFE coefficients – we insert them into the CFE of the self-energy, thereby obtaining an interpolated self-energy and Green’s function.

\mathcal{L} -interpolation has two properties that are very favorable: (i) $\tilde{\mathcal{L}}_{\mathbf{r}}$ appears to be shorter-ranged than $\tilde{\Sigma}_{\mathbf{r}}$ or $\tilde{M}_{\mathbf{r}}$ (according to some case studies presented below). (ii) Since the Liouvillian is, by definition, independent of frequency, its interpolated version remains hermitian, thus ensuring causality for the resulting self-energy. From a more general perspective: interpolating \mathcal{L} corresponds to directly interpolating the time-evolution generator for operators. This ensures that unitarity of the time evolution and therefore causality are preserved.

For the phenomenological YRZ self-energy ansatz of Ref. 33, \mathcal{L} -interpolation (along with a suitable choice of $\tilde{\mathcal{L}}_{\mathbf{r}}$) is equivalent to compact tiling; indeed, compact tiling served as inspiration for our strategy to use Liouvillian matrix elements as the objects to be periodized.

This paper is structured as follows: In Sec. II, we discuss the basic properties of the Liouvillian and its relation to the single-particle Green’s function and self-energy. Section III introduces \mathcal{L} -interpolation in great detail. In Sec. IV, we use the 1d Hubbard model as a testbed for \mathcal{L} -interpolation of CDMFT results (where “interpolation” refers to periodization). Using matrix product state (MPS) techniques, we obtain numerically exact results for this model. In Sec. IV A we show that a truncated Fourier expansion of \mathcal{L} has much more favorable convergence properties than that of Σ or M . In Sec. IV B, we then show that \mathcal{L} -interpolation yields faster convergence with cluster size for this model than M - or Σ -interpolation.

In Sec. V, we illustrate the advantages of \mathcal{L} - over Σ - and M -interpolation for DCA results. These were obtained from a 4-patch DCA+NRG treatment of the 2-dimensional Hubbard model for three choices of doping, corresponding to Fermi-liquid, pseudo-gap and Mott

regimes. We show that \mathcal{L} -interpolation is the interpolation scheme that most convincingly mimics the original discontinuous DCA+NRG results for the shape and spectral weight distribution along the FS (see Fig. 16, whose rightmost column is the interpolation that best mimics the discontinuous structures of the leftmost one). Moreover, this section also contains the main physical result of this paper: remarkably, \mathcal{L} -interpolation can yield Fermi and Luttinger arcs that together form a closed surface (see Fig. 19), with a smooth crossover between Fermi and Luttinger arcs (see Figs. 17 and 18). The aforementioned figures vividly illustrate the capability of \mathcal{L} -interpolation to generate intricate structures in non-trivial contexts; we invite the reader to briefly preview them before studying the formal developments below.

Section VI offers a summary and outlook. The Appendices provide additional details and computational aspects of \mathcal{L} -interpolation, and (in App. G) an application to the pseudogap phase of the 2-dimensional Hubbard model treated using CDMFT and exact diagonalization (CDMFT+ED).

II. CFE REPRESENTATION OF LIOUVILLIAN DYNAMICS

The use of Liouvillian methods for obtaining CFEs of 2-point functions and their self-energies has a long history [40–49]. In this section, we recapitulate some central ideas and results. Our presentation, building on those of Refs. 46–49, is self-contained and emphasizes aspects relevant for the \mathcal{L} -interpolation strategy in later sections.

Concretely, we (re)derive two central results. The first is formal: (i) The CFE coefficients of a Green's function or its self-energy are given by matrix elements of the Liouvillian in an orthonormal Krylov basis obtained via a Lanczos scheme involving repeated applications of the Liouvillian; this can be shown by resolving the Green's function in this Krylov basis. The second central result is a numerical recipe: (ii) If the spectral function of the Green's function or its self-energy is assumed known (analytically or numerically), the CFE coefficients can be computed numerically using a Lanczos scheme to build a basis of polynomials that are orthonormal with respect to said spectral function. These polynomials can also be used to define residual functions for terminating a CFE exactly at any finite depth.

These findings are embodied in three sets of equations that constitute the main results of this section: Eqs. (28) and (31) express CFE coefficients of the self-energy through matrix elements of the single-particle irreducible part of the Liouvillian; Eqs. (38) show how to compute CFE coefficients numerically from a known spectral function; and Eqs. (43) do the same for residual functions that terminate the CFE exactly according to Eq. (42). Readers familiar with these results may choose to skip this section.

In subsequent sections we propose an interpolation

scheme based on both results (i) and (ii): taking cDMFT Green's functions or self-energies as input, we numerically compute their CFE coefficients via (ii), then interpolate these, arguing via (i) that this amounts to interpolating the Liouvillian itself, thereby ensuring causality.

A. Liouvillian: basic notions

We begin by recalling some basic definitions and properties involving the Liouvillian. Consider a quantum system with Hamiltonian H acting in a Hilbert space \mathbb{V} . Linear operators acting on \mathbb{V} form a vector space, too, to be denoted $\mathbb{W} = \mathbb{V} \otimes \mathbb{V}^*$. We use a round-bracket ket notation, $| \)$, for its elements, representing a linear operator O acting in \mathbb{V} by $|O\rangle \in \mathbb{W}$ (the so-called Choi-Jamiołkowski transformation [50, 51]).

The Heisenberg equation of motion for operators, $-i\partial_t O(t) = [H, O(t)]$, is linear in $O(t)$. Therefore, it can be expressed in the form $-i\partial_t |O(t)\rangle = \mathcal{L}|O(t)\rangle$, with solution

$$|O(t)\rangle = e^{i\mathcal{L}t}|O(0)\rangle, \quad (3)$$

where the Liouvillian $\mathcal{L} \in \mathbb{W} \otimes \mathbb{W}^*$ is a linear operator on \mathbb{W} whose action is defined through $\mathcal{L}O = [H, O]$, or

$$\mathcal{L}|O\rangle = |[H, O]\rangle. \quad (4)$$

For systems in thermal equilibrium, it is useful to define an inner product on \mathbb{W} through [49]

$$\langle A|B\rangle = \langle \{A^\dagger, B\} \rangle, \quad (5)$$

where $\{ \ , \ }$ denotes an anti-commutator, $\langle O \rangle = \text{Tr}[\rho O]$ a thermal average and $\rho = e^{-H/T}/Z$ the thermal density matrix at temperature $T \neq 0$. This inner product ($| \)$ of Eq. (5) is well-defined if ρ has full rank. That is true for $T \neq 0$, but not for $T = 0$. We discuss the latter case in App. A. Since $[\rho, H] = 0$, the Liouvillian is hermitian w.r.t. this inner product, $\langle A|\mathcal{L}B\rangle = \langle \mathcal{L}A|B\rangle$.

B. Liouvillian representation of Green's functions

We next recall how fermionic single-particle Green's functions and self-energies can be expressed in terms of the Liouvillian. We begin with some standard definitions.

We consider a system described by a general fermionic Hamiltonian, $H = H_0 + H_{\text{int}}$, containing quadratic and quartic parts,

$$H_0 = \sum_{\alpha\beta} \epsilon_{\alpha\beta} c_\alpha^\dagger c_\beta, \quad H_{\text{int}} = \frac{1}{4} \sum_{\alpha\beta\gamma\delta} U_{\alpha\gamma,\delta\beta} c_\alpha^\dagger c_\gamma^\dagger c_\delta c_\beta. \quad (6)$$

Here, the fermionic operators satisfy $\{c_\alpha, c_\beta^\dagger\} = \delta_{\alpha\beta}$, where $\alpha = 1, \dots, M$ is a composite single-particle index encompassing, e.g., spin, orbital, and position or momentum indices. Let $\tilde{\mathbf{G}}^{\text{R/A}}(t)$ and $\mathbf{G}^{\text{R/A}}(\omega)$ denote

$M \times M$ matrices of retarded/advanced single-particle Green's functions and their Fourier transforms, respectively, with elements

$$\tilde{G}_{\alpha\beta}^{\text{R/A}}(t) = \mp i\theta(\pm t) \langle \{c_\alpha(0), c_\beta^\dagger(-t)\} \rangle, \quad (7a)$$

$$G_{\alpha\beta}^{\text{R/A}}(\omega) = \int_{-\infty}^{\infty} dt e^{i\omega^\pm t} \tilde{G}_{\alpha\beta}^{\text{R/A}}(t), \quad (7b)$$

where $\omega^\pm = \omega \pm i0^+$, and $\mathbf{G}^{\text{A}}(\omega) = \mathbf{G}^{\text{R}\dagger}(\omega)$. The Fourier-domain Green's functions can be viewed as analytic continuations, $\mathbf{G}^{\text{R/A}}(\omega) = \mathbf{G}(z \rightarrow \omega^\pm)$, of a function $\mathbf{G}(z)$ defined through the spectral representation

$$\mathbf{G}(z) = \int_{-\infty}^{\infty} d\omega \frac{\mathbf{A}(\omega)}{z - \omega}, \quad z \in \mathbb{C}, \quad (8a)$$

$$\mathbf{A}(\omega) = \frac{i}{2\pi} [\mathbf{G}^{\text{R}}(\omega) - \mathbf{G}^{\text{A}}(\omega)], \quad (8b)$$

with a hermitian spectral function, $\mathbf{A}(\omega) = \mathbf{A}^\dagger(\omega)$.

The non-interacting Green's function reads $\mathbf{G}_0(z) = (\mathbf{z} - \boldsymbol{\epsilon})^{-1}$, with $\mathbf{z} = z\mathbf{1}$, where $\boldsymbol{\epsilon}$ and $\mathbf{1}$ are $M \times M$ matrices with elements $\epsilon_{\alpha\beta}$ and $\delta_{\alpha\beta}$, respectively. The full Green's function can be expressed through the Dyson equation,

$$\mathbf{G}(z) = [\mathbf{G}_0^{-1}(z) - \boldsymbol{\Sigma}(z)]^{-1} = \frac{\mathbf{1}}{\mathbf{z} - \boldsymbol{\epsilon} - \boldsymbol{\Sigma}(z)}, \quad (9)$$

thereby defining the self-energy $\boldsymbol{\Sigma}(z)$.

We now express the above functions in terms of the Liouvillian. First, note that Eq. (7a) can be written as

$$\tilde{G}_{\alpha\beta}^{\text{R/A}}(t) = \mp i\theta(\pm t) \langle c_\alpha^\dagger | e^{-i\mathcal{L}t} | c_\beta^\dagger \rangle. \quad (10)$$

For notational brevity, we gather all $|c_\alpha^\dagger\rangle$ into a row or *block* of M operators, denoted

$$|\mathbf{c}^\dagger\rangle = (|c_1^\dagger\rangle, \dots, |c_M^\dagger\rangle) \in \mathbb{W}^{\oplus M}. \quad (11)$$

(This choice is appropriate for Hamiltonians with U(1) charge symmetry, as in Eq. (6). Footnote [52] discusses the modifications required if H_{int} also contains $c^\dagger c^\dagger$ and cc , as needed to describe mean-field superconductivity.) The relations $\{c_\alpha, c_\beta^\dagger\} = \delta_{\alpha\beta}$ imply the $M \times M$ matrix equation $(\mathbf{c}^\dagger | \mathbf{c}^\dagger) = \mathbf{1}$. Then, Eqs. (7) can be expressed as

$$\tilde{\mathbf{G}}^{\text{R/A}}(t) = \mp i\theta(\pm t) (\mathbf{c}^\dagger | e^{-i\mathcal{L}t} | \mathbf{c}^\dagger), \quad (12)$$

$$\mathbf{G}^{\text{R/A}}(\omega) = (\mathbf{c}^\dagger | \frac{\mathbf{1}}{\omega^\pm - \mathcal{L}} | \mathbf{c}^\dagger). \quad (13)$$

The latter can be viewed as analytic continuation of

$$\mathbf{G}(z) = (\mathbf{c}^\dagger | \frac{\mathbf{1}}{z - \mathcal{L}} | \mathbf{c}^\dagger), \quad (14a)$$

having a spectral representation of the form (8), with

$$\mathbf{A}(\omega) = (\mathbf{c}^\dagger | \delta(\omega - \mathcal{L}) | \mathbf{c}^\dagger). \quad (14b)$$

The spectral function $\mathbf{A}(\omega)$ has unit weight, $\int d\omega \mathbf{A}(\omega) = \mathbf{1}$, as already follows from Eqs. (7) and (8).

C. The single-particle irreducible subspace $\mathbb{W}_{\bar{c}}$

In Eq. (12), $e^{-i\mathcal{L}t}$ acts on the subspace of fermionic single-particle creation operators, $\mathbb{W}_c = \text{span}\{|c_\beta^\dagger\rangle\}$. We call these ‘‘charge-1’’ operators, since when acting on particle number eigenstates, they increase the charge by +1. Since $e^{-i\mathcal{L}t}$ can be expressed as an infinite power series, the Green's function is governed by the ‘‘dynamically relevant charge-1’’ subspace that is spanned by all operators in \mathbb{W}_c and all operators obtainable from them through repeated action with the Liouvillian. We denote this subspace by $\mathbb{W}_1(\mathcal{L}) \subset \mathbb{W}$. Importantly (and in contrast to \mathbb{W}) it depends on the Liouvillian; we will henceforth refrain from indicating this explicitly. (For brevity, we will refer to \mathbb{W}_1 simply as the ‘‘charge-1’’ subspace, even though operators with charge +1 may exist that are not in \mathbb{W}_1 [53].) \mathbb{W}_1 may have additional subspace structure, depending on the symmetries of the system at hand. For example, in a system with U(1) spin symmetry or translation symmetry, we could, in principle, define separate subspaces for spin \uparrow and \downarrow operators, or for operators with different momenta \mathbf{k} , respectively.

To express the self-energy through the Liouvillian, we need to exploit additional structure. We decompose the charge-1 operator space as $\mathbb{W}_1 = \mathbb{W}_c \oplus \mathbb{W}_{\bar{c}}$, where $\mathbb{W}_{\bar{c}}$ is the orthogonal complement of \mathbb{W}_c in \mathbb{W}_1 . It contains all charge-1 operators that are *single-particle irreducible*, i.e. orthogonal to \mathbb{W}_c . For example, if the Hamiltonian contains a quartic term such that $|c_\alpha^\dagger c_\beta c_\gamma^\dagger\rangle \in \mathbb{W}_1$, then the operator $|O_{\alpha\beta\gamma}\rangle = |c_\alpha^\dagger c_\beta c_\gamma^\dagger\rangle - |c_\alpha^\dagger\rangle \langle c_\beta c_\gamma^\dagger| - |c_\gamma^\dagger\rangle \langle c_\alpha^\dagger c_\beta|$ is in $\mathbb{W}_{\bar{c}}$, since $(c_\delta^\dagger | O_{\alpha\beta\gamma}\rangle) = 0$. We denote the projectors to the operator spaces \mathbb{W}_c and $\mathbb{W}_{\bar{c}}$ by

$$\mathcal{P}_c = |\mathbf{c}^\dagger\rangle \langle \mathbf{c}^\dagger| = \sum_\alpha |c_\alpha^\dagger\rangle \langle c_\alpha^\dagger|, \quad (15a)$$

$$\mathcal{P}_{\bar{c}} = 1 - \mathcal{P}_c = |\bar{\mathbf{c}}^\dagger\rangle \langle \bar{\mathbf{c}}^\dagger| = \sum_{\bar{\alpha}} |\bar{c}_{\bar{\alpha}}^\dagger\rangle \langle \bar{c}_{\bar{\alpha}}^\dagger|, \quad (15b)$$

where $\{|\bar{c}_{\bar{\alpha}}^\dagger\rangle\}$ is an arbitrary orthonormal basis of $\mathbb{W}_{\bar{c}} = \text{span}\{|\bar{c}_{\bar{\alpha}}^\dagger\rangle\}$. The Liouvillian can thus be expressed as

$$\mathcal{L} = \sum_{x, \bar{x} \in \{c, \bar{c}\}} \mathcal{L}_{x\bar{x}} = \sum_{\mathbf{x}, \bar{\mathbf{x}} \in \{c, \bar{c}\}} |\mathbf{x}^\dagger\rangle \langle \mathcal{L} |_{\mathbf{x}\bar{\mathbf{x}}} \langle \bar{\mathbf{x}}^\dagger|, \quad (16)$$

Here, $\mathcal{L}_{x\bar{x}} = \mathcal{P}_x \mathcal{L} \mathcal{P}_{\bar{x}}$ are projections of \mathcal{L} to the subspaces $\mathbb{W}_x, \mathbb{W}_{\bar{x}}$, and the blocks $[\mathcal{L}]_{\mathbf{x}\bar{\mathbf{x}}} = (\mathbf{x}^\dagger | \mathcal{L} | \bar{\mathbf{x}}^\dagger)$ are their representation in the bases spanning these subspaces. W.r.t. these, the Liouvillian has a 2×2 block structure, $(\begin{smallmatrix} cc & c\bar{c} \\ \bar{c}c & \bar{c}\bar{c} \end{smallmatrix})$.

Since $\mathcal{P}_{\bar{c}} |\mathbf{c}^\dagger\rangle = 0$, $(\mathbf{c}^\dagger | \mathcal{P}_{\bar{c}} = 0$, the Green's function $\mathbf{G}(z)$ of Eq. (14a) equals $[(z - \mathcal{L})^{-1}]_{cc}$, the cc block of $(z - \mathcal{L})^{-1}$. It can be found using the matrix identity (C1):

$$\begin{aligned} \mathbf{G}(z) &= (\mathbf{c}^\dagger | \left[z - \mathcal{L}_{cc} - \mathcal{L}_{c\bar{c}} \frac{1}{z - \mathcal{L}_{\bar{c}\bar{c}}} \mathcal{L}_{\bar{c}c} \right]^{-1} | \mathbf{c}^\dagger) \quad (17) \\ &= \left[\mathbf{z} - (\mathbf{c}^\dagger | \mathcal{L}_{cc} | \mathbf{c}^\dagger) - (\mathbf{c}^\dagger | \mathcal{L}_{c\bar{c}} \frac{1}{z - \mathcal{L}_{\bar{c}\bar{c}}} \mathcal{L}_{\bar{c}c} | \mathbf{c}^\dagger) \right]^{-1}. \end{aligned}$$

Comparing this to the Dyson equation (9), we obtain an

expression for the self-energy involving the Liouvillian:

$$\Sigma(z) = \Sigma^{\text{HF}} + \Sigma^{\text{dyn}}(z), \quad (18a)$$

$$\Sigma^{\text{HF}} = \epsilon_0 - \epsilon, \quad \epsilon_0 = (\mathbf{c}^\dagger | \mathcal{L}_{\text{cc}} | \mathbf{c}^\dagger), \quad (18b)$$

$$\Sigma^{\text{dyn}}(z) = (\mathbf{c}^\dagger | \mathcal{L}_{\text{c}\bar{c}} \frac{1}{z - \mathcal{L}_{\bar{c}\bar{c}}} \mathcal{L}_{\bar{c}\text{c}} | \mathbf{c}^\dagger). \quad (18c)$$

The z -independent part, Σ^{HF} , is the Hartree-Fock (HF) term. Since $\langle \{c_\alpha, [H_0, c_\beta^\dagger]\} \rangle = \epsilon_{\alpha\beta}$, its elements are

$$[\Sigma^{\text{HF}}]_{\alpha\beta} = \langle \{c_\alpha, [H_{\text{int}}, c_\beta^\dagger]\} \rangle = \sum_{\gamma\delta} \langle c_\gamma^\dagger c_\delta \rangle U_{\alpha\gamma, \delta\beta}. \quad (19)$$

Evidently, they are governed by the single-particle density matrix [54]. By contrast, the dynamical part of the self-energy, $\Sigma^{\text{dyn}}(z)$, is determined by the one-particle dynamics in the single-particle irreducible subspace $\mathbb{W}_{\bar{c}}$. From Eq. (18c), it is immediately evident that it has the same analytic properties as $\mathbf{G}(z)$.

We can further simplify Eq. (18c) by defining a set of operators that are normalized versions of $\mathcal{L}_{\bar{c}\text{c}} | \mathbf{c}^\dagger$. Their definition involves the *principal square root* of a matrix, hence we briefly digress to recall its definition and properties. For a positive semidefinite matrix \mathbf{M} , the principal square root $\mathbf{M}^{\frac{1}{2}}$ is the unique positive semidefinite hermitian matrix satisfying $\mathbf{M}^{\frac{1}{2}} \mathbf{M}^{\frac{1}{2}} = \mathbf{M}$. Given the eigendecomposition $\mathbf{M} = \mathbf{U} \mathbf{D} \mathbf{U}^\dagger$, the principal square root is obtained as $\mathbf{M}^{\frac{1}{2}} = \mathbf{U} \mathbf{D}^{\frac{1}{2}} \mathbf{U}^\dagger$.

If \mathbf{M} is full rank (all eigenvalues nonzero), the inverse of $\mathbf{M}^{\frac{1}{2}}$ is $\mathbf{M}^{-\frac{1}{2}} = \mathbf{U} \mathbf{D}^{-\frac{1}{2}} \mathbf{U}^\dagger$. If \mathbf{M} is rank-deficient (some eigenvalues zero), the principal square root can be expressed as $\mathbf{M}^{\frac{1}{2}} = \tilde{\mathbf{U}} \tilde{\mathbf{D}}^{\frac{1}{2}} \tilde{\mathbf{U}}^\dagger$, where $\tilde{\mathbf{D}}$, $\tilde{\mathbf{U}}$ and $\tilde{\mathbf{U}}^\dagger$ are truncated versions of \mathbf{D} , \mathbf{U} and \mathbf{U}^\dagger , obtained by dropping the columns and/or rows corresponding to zero eigenvalues. Then, the inverse of the principal square root can be defined only in the image space of $\tilde{\mathbf{U}} \tilde{\mathbf{U}}^\dagger$, namely as the pseudoinverse $\mathbf{M}^{-\frac{1}{2}} = \tilde{\mathbf{U}} \tilde{\mathbf{D}}^{-\frac{1}{2}} \tilde{\mathbf{U}}^\dagger$. Moreover, then $\mathbf{M}^{-\frac{1}{2}} \mathbf{M}^{\frac{1}{2}} = \tilde{\mathbf{M}}^{\frac{1}{2}} \tilde{\mathbf{M}}^{-\frac{1}{2}} = \tilde{\mathbf{U}} \tilde{\mathbf{U}}^\dagger$ is not a unit matrix, but a projector onto the subspace spanned by the eigenvectors with nonzero eigenvalues.

Returning to Eq. (18c), we define a block (or row vector) of single-particle irreducible operators $|\mathbf{q}_1\rangle$ as

$$|\mathbf{q}_1\rangle = \mathcal{L}_{\bar{c}\text{c}} | \mathbf{c}^\dagger \rangle \mathbf{t}_1^{-1} \quad (20a)$$

$$\mathbf{t}_1 \mathbf{t}_1 = (\mathbf{c}^\dagger | \mathcal{L}_{\bar{c}\bar{c}} \mathcal{L}_{\bar{c}\text{c}} | \mathbf{c}^\dagger). \quad \mathbf{t}_1 = \mathbf{t}_1^\dagger \geq 0, \quad (20b)$$

Here, the notation $\mathbf{t}_1 = \mathbf{t}_1^\dagger \geq 0$ is shorthand for stating that the *weight matrix* \mathbf{t}_1 is a hermitian positive definite matrix. Thus, Eq. (20b) defines \mathbf{t}_1 as the principal square root of the positive semidefinite hermitian matrix $\mathbf{M} = (\mathbf{c}^\dagger | \mathcal{L}_{\bar{c}\bar{c}} \mathcal{L}_{\bar{c}\text{c}} | \mathbf{c}^\dagger)$. Note that the right spaces of the operators $|\mathbf{q}_1\rangle$ and $|\mathbf{c}^\dagger\rangle$ are characterized by the same set of (physically motivated) spin and orbital quantum numbers, since $\mathbf{U} \mathbf{D}^{-\frac{1}{2}} \mathbf{U}^\dagger$ or $\tilde{\mathbf{U}} \tilde{\mathbf{D}}^{-\frac{1}{2}} \tilde{\mathbf{U}}^\dagger$ involve transformations out of and back into the right spaces of $|\mathbf{c}^\dagger\rangle$. This important property motivates the use of the principal square root here. If \mathbf{M} is full rank, Eq. (20a)

yields a block (or row vector) of M orthonormal operators $|\mathbf{q}_1\rangle \in \mathbb{W}_{\bar{c}}^M$, with $(\mathbf{q}_1 | \mathbf{q}_1) = \mathbf{1}$.

In many cases, \mathbf{M} is rank deficient for the simple reason that some of the single-particle orbitals are non-interacting; then, \mathbf{M} is zero on the entire block of non-interacting orbitals. In these cases, the rank deficiency of \mathbf{M} simply reflects the well-known fact that the single-particle irreducible self-energy of non-interacting orbitals is zero. Prominent—and for our work very relevant—examples are impurity models, where the bath orbitals are non-interacting, and \mathbf{M} is zero on the entire bath block.

If \mathbf{M} is rank deficient in the space of interacting orbitals, we take \mathbf{t}_1^{-1} to be the pseudoinverse of \mathbf{t}_1 in that space, such that $(\mathbf{q}_1 | \mathbf{q}_1) = \tilde{\mathbf{U}} \tilde{\mathbf{U}}^\dagger$. If \mathbf{t}_1 has rank 0, then $|\mathbf{q}_1\rangle = 0$. In the present work, we never encountered a partial rank-deficiency in the space of interacting operators: \mathbf{t}_1 was either full rank or had rank 0 in this space.

Using the definitions (20), we can express $\Sigma^{\text{dyn}}(z)$ as

$$\Sigma^{\text{dyn}}(z) = \mathbf{t}_1 \mathbf{S}(z) \mathbf{t}_1, \quad (21a)$$

$$\mathbf{S}(z) = (\mathbf{q}_1 | \frac{\mathbf{1}}{z - \mathcal{L}_{\bar{c}\bar{c}}} | \mathbf{q}_1). \quad (21b)$$

Hence, the frequency dependence of the self-energy is determined by $\mathbf{S}(z)$, a propagator in the single-particle irreducible subspace $\mathbb{W}_{\bar{c}}$. Let us introduce a spectral representation for $\mathbf{S}(z)$ analogous to Eqs. (8a) and (14b) for $\mathbf{G}(z)$ and $\mathbf{A}(\omega)$,

$$\mathbf{S}(z) = \int_{-\infty}^{\infty} d\omega \frac{\mathbf{W}(\omega)}{z - \omega}, \quad (22a)$$

$$\mathbf{W}(\omega) = (\mathbf{q}_1 | \delta(\omega - \mathcal{L}_{\bar{c}\bar{c}}) | \mathbf{q}_1), \quad (22b)$$

with $\int d\omega \mathbf{W}(\omega) = \mathbf{1}$ and $\mathbf{W}(\omega) = \mathbf{W}^\dagger(\omega)$. Correspondingly, if we express the retarded/advanced self-energies $\Sigma^{\text{R/A}}(\omega) = \Sigma(\omega^\pm)$ as $\Sigma'(\omega) \mp i\pi \Sigma''(\omega)$, then

$$\Sigma''(\omega) = \frac{i}{2\pi} [\Sigma^{\text{R}}(\omega) - \Sigma^{\text{A}}(\omega)] = \mathbf{t}_1 \mathbf{W}(\omega) \mathbf{t}_1, \quad (23a)$$

$$\Sigma'(\omega) = \Sigma^{\text{HF}} + P \int_{-\infty}^{\infty} d\omega' \frac{\Sigma''(\omega')}{z - \omega'}. \quad (23b)$$

Note that $\int d\omega \Sigma''(\omega) = \mathbf{t}_1 \mathbf{t}_1$, which identifies \mathbf{t}_1 as the principal square root of the total spectral weight of the retarded self-energy. We will call $\mathbf{W}(\omega)$ the *normalized spectral function* and \mathbf{t}_1 the *weight matrix* of $\Sigma^{\text{dyn}}(z)$.

Equations (17), (18) and (21a) together imply

$$\mathbf{G}(z) = \frac{1}{z - \epsilon_0 - \mathbf{t}_1 \mathbf{S}(z) \mathbf{t}_1}. \quad (24)$$

Together with Eq. (21b), this constitutes the first step of CFEs of the Green's function and self-energy, respectively, as explained in more detail in the next subsection.

The above relations are general and exact. When dealing with fermionic many-body systems, \mathbb{W}_{c} can usually be handled with reasonable effort, whereas $\mathbb{W}_{\bar{c}}$ has to

be dealt with in an approximate manner. The Hartree-Fock approximation treats the self-energy solely within $\mathbb{W}_{\bar{c}}$, approximating Σ by Σ^{HF} . It thus sets $\Sigma^{\text{dyn}} = 0$ and completely ignores $\mathbb{W}_{\bar{c}}$. For long-ranged interactions, Σ^{HF} is non-local, for on-site interactions it is local. This is also true within DMFT. Additionally, DMFT incorporates single-particle irreducible contributions from $\mathbb{W}_{\bar{c}}$ by including Σ^{dyn} , but approximates it as local. Thus, $\mathcal{L}_{\bar{c}\bar{c}}$ and \mathbf{t}_1 are approximated as local in DMFT.

Cluster extensions of DMFT additionally incorporate non-local but short-ranged matrix elements in $\mathcal{L}_{\bar{c}\bar{c}}$ and \mathbf{t}_1 . In CDMFT, matrix elements are fully considered within each real-space cluster, while inter-cluster matrix elements are neglected. As a result, translation symmetry is broken. DCA, on the other hand, tiles the Brillouin zone (BZ) into N_p patches and approximates $\mathcal{L}_{\bar{c}\bar{c}}$ and \mathbf{t}_1 as constant within each patch. As a result, DCA is translation invariant, but the self-energy is not a smooth function of \mathbf{k} . Our goal in this work is to reinstate the translation invariance in CDMFT or a smooth \mathbf{k} -dependence in DCA by interpolating (periodizing or interpolating, respectively) \mathbf{t}_1 and the matrix elements of $\mathcal{L}_{\bar{c}\bar{c}}$.

In the remaining subsections of this section, we show how a matrix representation of $\mathcal{L}_{\bar{c}\bar{c}}$ within $\mathbb{W}_{\bar{c}}$ can be constructed, yielding a CFE for $\mathbf{S}(z)$ and thus also for $\Sigma^{\text{dyn}}(z)$. Then, we will switch perspective, assume that the spectral function $\mathbf{W}(\omega)$ of $\mathbf{S}(z)$ is known analytically or numerically, and show how a CFE for the latter can be constructed, thereby also obtaining a CFE for $\Sigma^{\text{dyn}}(z)$. In Sec. III we will then interpolate the self-energy by interpolating its CFE coefficients.

D. CFE for the self-energy

A CFE for the dynamical part of the self-energy, $\Sigma^{\text{dyn}}(z) = \mathbf{t}_1 \mathbf{S}(z) \mathbf{t}_1$, can be obtained by representing $\mathbf{S}(z)$ in a Krylov space constructed via an iterative Lanczos procedure [49, 55]. According to Eq. (21), $\mathbf{S}(z)$ involves the projection of the Liouvillian to the single-particle irreducible subspace, $\mathcal{L}_{\bar{c}\bar{c}}$. We thus define the Krylov space $\mathbb{K}_N = \text{span}\{|\mathbf{q}_1\rangle, \mathcal{L}_{\bar{c}\bar{c}}|\mathbf{q}_1\rangle, \dots, \mathcal{L}_{\bar{c}\bar{c}}^N|\mathbf{q}_1\rangle\}$, with $|\mathbf{q}_1\rangle$ given by Eq. (20a), and use an $(N-1)$ -step *block*-Lanczos procedure to obtain an orthonormal basis of operator blocks such that $\mathbb{K}_N = \text{span}\{|\mathbf{q}_1\rangle, |\mathbf{q}_2\rangle, \dots, |\mathbf{q}_N\rangle\}$ and

$$(\mathbf{q}_n|\mathbf{q}_{n'}) = [\mathbb{1}]_{nn'} = \delta_{nn'} \mathbf{1}. \quad (25)$$

The blocks for $n \geq 2$ are constructed iteratively by repeating four substeps that together constitute one step:

$$(1) \quad |\tilde{\mathbf{q}}_n\rangle = \mathcal{L}_{\bar{c}\bar{c}}|\mathbf{q}_{n-1}\rangle, \quad \epsilon_{n-1} = (\mathbf{q}_{n-1}|\tilde{\mathbf{q}}_n\rangle), \quad (26a)$$

$$(2) \quad |\mathbf{q}_n^\perp\rangle = |\tilde{\mathbf{q}}_n\rangle - \sum_{n'=0}^{n-1} |\mathbf{q}_{n'}\rangle (\mathbf{q}_{n'}|\tilde{\mathbf{q}}_n\rangle), \quad (26b)$$

$$(3) \quad \mathbf{t}_n \mathbf{t}_n = (\mathbf{q}_n^\perp|\mathbf{q}_n^\perp), \quad \mathbf{t}_n = \mathbf{t}_n^\dagger \geq 0, \quad (26c)$$

$$(4) \quad |\mathbf{q}_n\rangle = |\mathbf{q}_n^\perp\rangle \mathbf{t}_n^{-1} \quad (26d)$$

(1) applies $\mathcal{L}_{\bar{c}\bar{c}}$ to $|\mathbf{q}_{n-1}\rangle$ to obtain $|\tilde{\mathbf{q}}_n\rangle$ and computes its overlap with $|\mathbf{q}_{n-1}\rangle$; (2) orthogonalizes it w.r.t. all previous blocks to obtain $|\mathbf{q}_n^\perp\rangle$; (3) defines the $M \times M$ weight matrix \mathbf{t}_n as the principal square root of the matrix $(\mathbf{q}_n^\perp|\mathbf{q}_n^\perp)$ (which is positive semidefinite, since $\mathcal{L}_{\bar{c}\bar{c}}$ is hermitian); and (4) normalizes $|\mathbf{q}_n^\perp\rangle$ to obtain $|\mathbf{q}_n\rangle$, where \mathbf{t}_n^{-1} is the pseudoinverse of \mathbf{t}_n . The reasons for defining \mathbf{t}_n using the principal square root are the same as those discussed for the construction of $|\mathbf{q}_1\rangle$ above. If \mathbf{t}_n has rank 0, the iterative procedure terminates.

Using the convenient definition $|\mathbf{q}_0\rangle = 0$, the generated basis operators satisfy a three-term recursion relation,

$$\mathcal{L}_{\bar{c}\bar{c}}|\mathbf{q}_n\rangle = |\mathbf{q}_n\rangle \epsilon_n + |\mathbf{q}_{n+1}\rangle \mathbf{t}_{n+1} + |\mathbf{q}_{n-1}\rangle \mathbf{t}_n, \quad n \geq 1. \quad (27)$$

If at step $N-1$ one finds $|\mathbf{q}_N\rangle = 0$, the Lanczos iteration terminates automatically; otherwise one terminates it by hand after $N-1$ steps. Equation (27) implies that in the Krylov basis $\{|\mathbf{q}_1\rangle, \dots, |\mathbf{q}_N\rangle\}$, the single-particle irreducible projection of the Liouvillian is represented by a block-tridiagonal matrix (also known as Jacobi matrix),

$$[\mathbb{L}_N]_{\bar{c}\bar{c}} = \begin{pmatrix} \epsilon_1 & \mathbf{t}_2 & \mathbf{0} & \cdots & \mathbf{0} & \mathbf{0} & \mathbf{0} \\ \mathbf{t}_2 & \epsilon_2 & \mathbf{t}_3 & \cdots & \mathbf{0} & \mathbf{0} & \mathbf{0} \\ \mathbf{0} & \mathbf{t}_3 & \epsilon_3 & \cdots & \mathbf{0} & \mathbf{0} & \mathbf{0} \\ \vdots & \vdots & \vdots & \ddots & \vdots & \vdots & \vdots \\ \mathbf{0} & \mathbf{0} & \mathbf{0} & \cdots & \epsilon_{N-2} & \mathbf{t}_{N-1} & \mathbf{0} \\ \mathbf{0} & \mathbf{0} & \mathbf{0} & \cdots & \mathbf{t}_{N-1} & \epsilon_{N-1} & \mathbf{t}_N \\ \mathbf{0} & \mathbf{0} & \mathbf{0} & \cdots & \mathbf{0} & \mathbf{t}_N & \epsilon_N \end{pmatrix}. \quad (28)$$

Its N^2 blocks are all $M \times M$ matrices, given by

$$[[\mathbb{L}_N]_{\bar{c}\bar{c}}]_{nn'} = (\mathbf{q}_n|\mathcal{L}_{\bar{c}\bar{c}}|\mathbf{q}_{n'}) = \begin{cases} \epsilon_n, & n' = n, \\ \mathbf{t}_{n+1}, & n' = n+1, \\ \mathbf{t}_n, & n' = n-1, \\ \mathbf{0} & \text{otherwise.} \end{cases} \quad (29)$$

Within \mathbb{K}_N , expression (21b) for $\mathbf{S}(z)$ is represented as

$$\mathbf{S}(z) \simeq [([\mathbb{Z}_N]_{\bar{c}\bar{c}} - [\mathbb{L}_N]_{\bar{c}\bar{c}})^{-1}]_{n=1, n'=1}. \quad (30)$$

where $\mathbb{Z}_N = z \mathbb{1}_N$ equals z times a block unit matrix, with $[\mathbb{1}_N]_{nn'} = \delta_{nn'} \mathbf{1}$. Using Eq. (C8), a formula for the 11- (upper-left) block of the inverse of a tridiagonal block matrix, we obtain the desired CFE (with $\mathbf{z}_n = \mathbf{z} - \epsilon_n$):

$$\mathbf{S}(z) \simeq \frac{\mathbf{1}}{\mathbf{z}_1 - \mathbf{t}_2 \frac{\mathbf{1}}{\mathbf{z}_2 - \cdots - \mathbf{t}_N \frac{\mathbf{1}}{\mathbf{z}_N}} \mathbf{t}_2}. \quad (31)$$

We have thus established that the CFE coefficients ϵ_n and \mathbf{t}_n of $\mathbf{S}(z)$ and hence of $\Sigma^{\text{dyn}}(z)$ are matrix elements of the single-particle irreducible Liouvillian $\mathcal{L}_{\bar{c}\bar{c}}$. The CFE (31) becomes exact for sufficiently large N , provided that the moment problem defined by the measure $\mathbf{W}(\omega)d\omega$ is determinate. This is the case if the support of $\mathbf{W}(\omega)$ is bounded, or if $\mathbf{W}(\omega)$ decays fast enough at high frequencies, see App. B for more details.

E. Computing CFE coefficients via polynomials

Above, we found that the CFE coefficients of $\mathbf{S}(z)$ correspond to matrix elements $(\mathbf{q}_n | \mathcal{L}_{\bar{c}\bar{c}} | \mathbf{q}_{n'})$ of the single-particle-irreducible projection of the Liouvillian. Since each Lanczos block $|\mathbf{q}_n\rangle$ is a linear combination of powers of $\mathcal{L}_{\bar{c}\bar{c}}$ applied to the initial block $|\mathbf{q}_1\rangle$, all such matrix elements are linear combinations of diagonal matrix elements of the form $(\mathbf{q}_1 | \mathcal{L}_{\bar{c}\bar{c}}^m | \mathbf{q}_1)$. Now, the latter correspond to moments of the spectral function $\mathbf{W}(\omega)$ of $\mathbf{S}(z)$, due to an identity following from Eq. (22b):

$$(\mathbf{q}_1 | \mathcal{L}_{\bar{c}\bar{c}}^m | \mathbf{q}_1) = \int d\omega \mathbf{W}(\omega) \omega^m. \quad (32)$$

It follows that if $\mathbf{W}(\omega)$ is known explicitly (analytically or numerically), the CFE coefficients of $\mathbf{S}(z)$ can be computed directly from the moments of $\mathbf{W}(\omega)$. This can be done by constructing a set of orthonormal vector-valued polynomials [42, 48, 49] using a Lanczos scheme completely analogous to that described in the previous subsection [55–58]. Below, we review this construction.

The block Lanczos scheme in Sec. IID is initialized by a length- M block or row vector of operators, $|\mathbf{q}_1\rangle$. Its entries, all vectors in $\mathbb{W}_{\bar{c}}$, are by definition mutually orthonormal, $(\mathbf{q}_1 | \mathbf{q}_1) = \mathbf{1}$. Each block of Lanczos vectors $|\mathbf{q}_n\rangle$ can be written as a linear combination of the form

$$|\mathbf{q}_n\rangle = \sum_{\bar{n}=0}^{n-1} \mathcal{L}_{\bar{c}\bar{c}}^{\bar{n}} |\mathbf{q}_1\rangle \mathbf{C}_{\bar{n}n}, \quad (33)$$

where for each $\bar{n}n$, $\mathbf{C}_{\bar{n}n}$ is an $M \times M$ matrix that right-multiplies the length- M row vector of operators $|\mathbf{q}_1\rangle$. When this representation is inserted into the orthonormality relations (25) and the matrix elements of Eq. (29), both $(\mathbf{q}_n | \mathbf{q}'_n)$ and $(\mathbf{q}_n | \mathcal{L}_{\bar{c}\bar{c}} | \mathbf{q}'_n)$ become linear combinations of matrix elements $(\mathbf{q}_1 | \mathcal{L}_{\bar{c}\bar{c}}^m | \mathbf{q}_1)$ involving various powers m of $\mathcal{L}_{\bar{c}\bar{c}}$. Using Eq. (32) to express these through moments of $\mathbf{W}(\omega)$, Eqs. (25) and (29) take the form

$$[\mathbb{1}]_{nn'} = \int d\omega \mathbf{p}_n^{(1)\dagger}(\omega) \mathbf{W}(\omega) \mathbf{p}_{n'}^{(1)}(\omega), \quad (34a)$$

$$[\mathbb{L}_{\bar{c}\bar{c}}]_{nn'} = \int d\omega \mathbf{p}_n^{(1)\dagger}(\omega) \mathbf{W}(\omega) \omega \mathbf{p}_{n'}^{(1)}(\omega), \quad (34b)$$

where we have defined the matrix polynomials

$$\mathbf{p}_n^{(1)}(\omega) = \sum_{\bar{n}=0}^{n-1} \omega^{\bar{n}} \mathbf{C}_{\bar{n}n}. \quad (35)$$

(The reason for the superscript (1) on $\mathbf{p}_n^{(1)}(\omega)$ will become clear below.) For each n , $\mathbf{p}_n^{(1)}(\omega)$ is an $M \times M$ matrix. Its columns, enumerated by $\alpha = 1, \dots, M$, are length- M column-vector-valued polynomials of degree $n-1$, which we denote by $p_{n,\alpha}^{(1)} : \mathbb{R} \rightarrow \mathbb{C}^M$, $\omega \mapsto p_{n,\alpha}^{(1)}(\omega)$. Note that $p_{n,\alpha}^{(1)}$ is constructed from column α of the matrix $\mathbf{C}_{\bar{n}n}$, which via Eq. (33) also defines entry α of the block

$|\mathbf{q}_n\rangle = (|q_{n,1}\rangle, \dots, |q_{n,M}\rangle)$. This yields a one-to-one correspondence, $p_{n,\alpha}^{(1)} \leftrightarrow |q_{n,\alpha}\rangle$, between length- M column-vector-valued polynomials and operators in $\mathbb{W}_{\bar{c}}$. The matrix $\mathbf{p}_n^{(1)}$ can thus be also viewed as a length- M row vector of column-vector-valued polynomials, associated with the length- M row vector of operators $|\mathbf{q}_n\rangle$.

To compactify the notation, let

$$\langle f, g \rangle = \int d\omega f^\dagger(\omega) \mathbf{W}(\omega) g(\omega) \quad (36)$$

denote the inner product, with matrix-valued measure $\mathbf{W}(\omega)d\omega$, of two length- M column-vector-valued functions, $f : \mathbb{R} \rightarrow \mathbb{C}^M$, $\omega \mapsto f(\omega)$, and likewise for g . Then, equations (34) can be expressed as

$$\langle \mathbf{p}_n^{(1)}, \mathbf{p}_{n'}^{(1)} \rangle = \mathbb{1}_{nn'}, \quad (37a)$$

$$\langle \mathbf{p}_n^{(1)}, \hat{\mathcal{L}}_{\bar{c}\bar{c}} \mathbf{p}_{n'}^{(1)} \rangle = [\mathbb{L}_{\bar{c}\bar{c}}]_{nn'}, \quad (37b)$$

where $\hat{\mathcal{L}}_{\bar{c}\bar{c}}$ is the Liouvillian in function space, acting as $\hat{\mathcal{L}}_{\bar{c}\bar{c}} f(\omega) = \omega f(\omega)$. For given nn' , Eq. (37a) is an $M \times M$ matrix equation whose element $\alpha\alpha'$ reads $\langle p_{n,\alpha}^{(1)}, p_{n',\alpha'}^{(1)} \rangle = \delta_{nn'} \delta_{\alpha\alpha'}$; similarly for Eq. (37b).

Equation (37a) states that the $N \cdot M$ vector-valued polynomials $\{p_{n,\alpha}^{(1)}\}$ defined by the columns of all $\mathbf{p}_n^{(1)}(\omega)$, $n=1, \dots, N$, are mutually orthonormal w.r.t. the matrix-valued measure $\mathbf{W}(\omega)d\omega$. (The superscript on $\mathbf{p}_n^{(1)}$ signifies that these are “associated polynomials of the first kind” relative to another set of orthonormal polynomials, namely those defined w.r.t. the measure $\mathbf{A}(\omega)d\omega$, see App. B.) The polynomials $\{p_{n,\alpha}^{(1)}\}$ thus form a basis for the space of all length- M column-vector-valued polynomials of degree $N-1$. Equation (37b) states that all matrix elements of $\mathbb{L}_{\bar{c}\bar{c}}$, and hence all CFE coefficients of $\mathbf{S}(z)$, can be expressed as matrix elements of the Liouvillian $\hat{\mathcal{L}}_{\bar{c}\bar{c}}$ in this basis.

For a given $\mathbf{W}(\omega)$, the relations (37), together with the initial condition $\mathbf{p}_1^{(1)}(\omega) = \mathbf{1}$, fully define the basis $\{p_{n,\alpha}^{(1)}\}$. It can be constructed iteratively via a block-Lanczos procedure (in complete analogy to that for $|\mathbf{q}_n\rangle$) which also generates to matrix elements $[\mathbb{L}_{\bar{c}\bar{c}}]_{nn'}$. It involves (1) multiplication by ω , (2) orthogonalization, (3) identification of a normalization matrix, and (4) normalization:

$$(1) \quad \tilde{\mathbf{p}}_n^{(1)}(\omega) = \omega \mathbf{p}_{n-1}^{(1)}(\omega), \quad \boldsymbol{\epsilon}_{n-1} = \langle \mathbf{p}_{n-1}^{(1)}, \tilde{\mathbf{p}}_n^{(1)} \rangle, \quad (38a)$$

$$(2) \quad \mathbf{p}_n^{(1)\perp}(\omega) = \tilde{\mathbf{p}}_n^{(1)}(\omega) - \sum_{n'=0}^{n-1} \mathbf{p}_{n'}^{(1)}(\omega) \langle \mathbf{p}_{n'}^{(1)}, \tilde{\mathbf{p}}_n^{(1)} \rangle, \quad (38b)$$

$$(3) \quad \mathbf{t}_n \mathbf{t}_n = \langle \mathbf{p}_n^{(1)\perp}, \mathbf{p}_n^{(1)\perp} \rangle, \quad \mathbf{t}_n = \mathbf{t}_n^\dagger \geq 0, \quad (38c)$$

$$(4) \quad \mathbf{p}_n^{(1)}(\omega) = \mathbf{p}_n^{(1)\perp}(\omega) \mathbf{t}_n^{-1}. \quad (38d)$$

(On the right of Eq. (38b), the second term involves matrix multiplication of two $M \times M$ matrices, the matrix of polynomials $\mathbf{p}_{n'}^{(1)}(\omega)$ and the inner product matrix $\langle \mathbf{p}_{n'}^{(1)}, \tilde{\mathbf{p}}_n^{(1)} \rangle$.) Along the way, we obtain the CFE coefficients $\boldsymbol{\epsilon}_{n-1}$ from Eq. (38a), and \mathbf{t}_n as the principal square root of $\langle \mathbf{p}_n^{(1)\perp}, \mathbf{p}_n^{(1)\perp} \rangle$ in Eq. (38c), as in Eq. (26d).

The resulting polynomials and CFE coefficients satisfy a three-term recurrence relation analogous to Eq. (27):

$$\omega \mathbf{p}_n^{(1)} = \mathbf{p}_n^{(1)} \epsilon_n + \mathbf{p}_{n+1}^{(1)} \mathbf{t}_{n+1} + \mathbf{p}_{n-1}^{(1)} \mathbf{t}_n, \quad n \geq 1, \quad (39)$$

with $\mathbf{p}_0^{(1)}(\omega) = \mathbf{0}$, $\mathbf{p}_1^{(1)}(\omega) = \mathbf{1}$.

Equations (21) and (22) together imply that the dynamical part of the self-energy can be expressed as

$$\begin{aligned} \Sigma^{\text{dyn}}(z) &= \mathbf{t}_1 (\mathbf{p}_1^{(1)}, (z - \hat{\mathcal{L}}_{\bar{c}\bar{c}})^{-1} \mathbf{p}_1^{(1)}) \mathbf{t}_1 \\ &= \mathbf{t}_1 [(z - \mathbb{L}_{\bar{c}\bar{c}})^{-1}]_{11} \mathbf{t}_1. \end{aligned} \quad (40)$$

The same argument that led from Eq. (30) to (31) then gives an approximate depth- N CFE (41) for $\Sigma^{\text{dyn}}(z)$ (with $\mathbf{z}_n = \mathbf{z} - \epsilon_n$):

$$\Sigma^{\text{dyn}}(z) \simeq \mathbf{t}_1 \frac{\mathbf{1}}{\mathbf{z}_1 - \mathbf{t}_2 \frac{\mathbf{1}}{\mathbf{z}_2 - \dots - \mathbf{t}_N \frac{\mathbf{1}}{\mathbf{z}_N} \mathbf{t}_N}} \mathbf{t}_1. \quad (41)$$

If the self-energy spectrum $\mathbf{W}(\omega)$ is discrete with a finite number of δ -peaks, as is the case for a finite-size system, $\Sigma^{\text{dyn}}(z)$ has an exact finite-depth CFE representation of the form (41). Otherwise, Eq. (41) is an approximation.

F. Exact termination of CFE

To replace Eq. (41) by an exact depth- N CFE, we subtract an $M \times M$ matrix function, the *residual function* $\mathbf{R}_N(z)$, from the denominator at depth N and *define* it by the requirement that the following equation is exact:

$$\Sigma^{\text{dyn}}(z) = \mathbf{t}_1 \frac{\mathbf{1}}{\mathbf{z}_1 - \mathbf{t}_2 \frac{\mathbf{1}}{\mathbf{z}_2 - \dots - \mathbf{t}_N \frac{\mathbf{1}}{\mathbf{z}_N - \mathbf{R}_N(z)} \mathbf{t}_N}} \mathbf{t}_1. \quad (42)$$

In other words, the residual function $\mathbf{R}_N(z)$ by definition terminates the CFE at level N in an exact manner. As shown in App. D, once the matrix polynomials $\mathbf{p}_{N-1}^{(1)}(\omega)$ and $\mathbf{p}_N^{(1)}(\omega)$ are known, they can be used to compute, $\mathbf{R}_{N-1}(z)$, which terminates the CFE exactly at depth $N-1$, as follows:

$$\mathbf{R}_{N-1}(z) = \mathbf{I}_N(z) - \mathbf{F}_N^L(z) \mathbf{G}_N^{-1}(z) \mathbf{F}_N^R(z), \quad (43a)$$

$$\mathbf{G}_N(z) = \int d\omega \mathbf{p}_{N-1}^{(1)\dagger}(\omega) \mathbf{W}(\omega) \mathbf{p}_{N-1}^{(1)}(\omega) / (z - \omega), \quad (43b)$$

$$\mathbf{F}_N^L(z) = \int d\omega \mathbf{p}_N^{(1)\perp\dagger}(\omega) \mathbf{W}(\omega) \mathbf{p}_{N-1}^{(1)}(\omega) / (z - \omega), \quad (43c)$$

$$\mathbf{F}_N^R(z) = \int d\omega \mathbf{p}_{N-1}^{(1)\dagger}(\omega) \mathbf{W}(\omega) \mathbf{p}_N^{(1)\perp}(\omega) / (z - \omega), \quad (43d)$$

$$\mathbf{I}_N(z) = \int d\omega \mathbf{p}_N^{(1)\perp\dagger}(\omega) \mathbf{W}(\omega) \mathbf{p}_N^{(1)\perp}(\omega) / (z - \omega). \quad (43e)$$

The CFE (42) can also be constructed iteratively via a sequence of depth-1 CFEs, each terminated by a residual function that serves as starting point for the next iteration. Initialize the process using $\mathbf{R}_0(z) = \Sigma^{\text{dyn}}(z)$ as input. Then, iteratively proceed as follows for $n \geq 1$: (a) Using $\mathbf{R}_{n-1}(z)$ as input, find its normalized spectral function $\mathbf{W}_{n-1}(\omega)$ and weight matrix \mathbf{t}_n , as follows:

$$\mathbf{R}_{n-1}''(\omega) = \frac{i}{2\pi} [\mathbf{R}_{n-1}(\omega^+) - \mathbf{R}_{n-1}^\dagger(\omega^+)], \quad (44a)$$

$$\mathbf{t}_n \mathbf{t}_n = \int d\omega \mathbf{R}_{n-1}''(\omega), \quad \mathbf{t}_n = \mathbf{t}_n^\dagger \geq 0, \quad (44b)$$

$$\mathbf{W}_{n-1}(\omega) = \mathbf{t}_n^{-1} \mathbf{R}_{n-1}''(\omega) \mathbf{t}_n^{-1}. \quad (44c)$$

(b) Use a one-step Lanczos scheme with measure $\mathbf{W}_{n-1}(\omega) d\omega$ to compute ϵ_n . (c) Express $\mathbf{R}_{n-1}(z)$ via the depth-1 version of Eq. (42), with $\{\Sigma^{\text{dyn}}, \mathbf{t}_1, \mathbf{z}_1, \mathbf{R}_1\}$ there replaced by $\{\mathbf{R}_{n-1}, \mathbf{t}_n, \mathbf{z}_n, \mathbf{R}_n\}$:

$$\mathbf{R}_{n-1}(z) = \mathbf{t}_n \frac{\mathbf{1}}{\mathbf{z}_n - \mathbf{R}_n(z)} \mathbf{t}_n. \quad (45)$$

(Concretely: Let us use a superscript (n) to tag objects obtained from the n -th one-step Lanczos scheme with measure $\mathbf{W}_{n-1}(\omega) d\omega$. Step (b) yields $\mathbf{p}_1^{(n)}(\omega) = \mathbf{1}$, $\tilde{\mathbf{p}}_2^{(n)} = \omega \mathbf{1}$, $\epsilon_1^{(n)}$, $\mathbf{p}_2^{(n)\perp} = \omega \mathbf{1} - \epsilon_1^{(n)}$. Step (c) yields $\mathbf{R}_1^{(n)}$ via Eqs. (43), with $\{\mathbf{W}, \mathbf{p}_{N-1}^{(1)}, \mathbf{p}_N^{(1)\perp}, \mathbf{R}_{N-1}\}$ there replaced by $\{\mathbf{W}_{n-1}, \mathbf{1}, \omega \mathbf{1} - \epsilon_1^{(n)}, \mathbf{R}_1^{(n)}\}$. Finally, set $\epsilon_n = \epsilon_1^{(n)}$ and $\mathbf{R}_n = \mathbf{R}_1^{(n)}$.) Concatenating N depth-1 CFEs of the form (45) yields a CFE of the form (42). The resulting CFE coefficients are identical to those obtained via an N -step Lanczos scheme.

To conclude this subsection, we note that a CFE for the self-energy implies a CFE for the corresponding Green's function: inserting Eqs. (18a) and (42) for the self-energy into the Dyson equation (9) for $\mathbf{G}(z)$, we obtain

$$\mathbf{G}(z) = \frac{\mathbf{1}}{\mathbf{z}_0 - \mathbf{t}_1 \frac{\mathbf{1}}{\mathbf{z}_1 - \mathbf{t}_2 \frac{\mathbf{1}}{\mathbf{z}_2 - \dots - \mathbf{t}_N \frac{\mathbf{1}}{\mathbf{z}_N - \mathbf{R}_N(z)} \mathbf{t}_N}} \mathbf{t}_1}. \quad (46)$$

This CFE can also be obtained directly by using a Lanczos scheme with measure $\mathbf{A}(\omega) d\omega$ to construct an orthogonal set of matrix polynomials $\{\mathbf{p}_n(\omega), n = 0, \dots, N\}$, initiated with $\mathbf{p}_0(\omega) = \mathbf{1}$. These polynomials differ from the $\{\mathbf{p}_n^{(1)}(\omega), n = 1, \dots, N\}$ obtained using the measure $\mathbf{W}(\omega) d\omega$, but the CFE coefficients $\epsilon_{n \geq 1}$ and $\mathbf{t}_{n \geq 2}$ are the same, as elaborated in App. B.

G. Quantum impurity models: separating hybridization function and self-energy

Quantum impurity models involve a small number N_d of impurity orbitals and a large number N_b of bath or-

bitals. We assemble their creation operators into length- N_d and length- N_b row vectors, denoted $|\mathbf{d}^\dagger\rangle$ and $|\mathbf{b}^\dagger\rangle$, respectively, and combine them as $|\mathbf{c}^\dagger\rangle = (|\mathbf{d}^\dagger\rangle, |\mathbf{b}^\dagger\rangle)$, a row vector of length $M = N_d + N_b$. Its entries span the single-particle subspace, $\mathbb{W}_c = \mathbb{W}_d \oplus \mathbb{W}_b$, of the impurity model. In analogy to Eq. (15a), we define the projectors

$$\mathcal{P}_d = |\mathbf{d}^\dagger\rangle\langle\mathbf{d}^\dagger|, \quad \mathcal{P}_b = |\mathbf{b}^\dagger\rangle\langle\mathbf{b}^\dagger|, \quad \mathcal{P}_c = 1 - \mathcal{P}_c, \quad (47)$$

and denote the corresponding projections of the Liouvillian by $\mathcal{L}_{xx'} = \mathcal{P}_x \mathcal{L} \mathcal{P}_{x'}$, with $x, x' \in \{d, b, \bar{c}\}$. This more finely grained decomposition $\mathbb{W} = \mathbb{W}_d \oplus \mathbb{W}_b \oplus \mathbb{W}_{\bar{c}}$ induces a 3×3 block structure on \mathcal{L} , akin to Eq. (16), having blocks $[\mathcal{L}]_{\mathbf{x}\bar{\mathbf{x}}} = (\mathbf{x}^\dagger | \mathcal{L} | \bar{\mathbf{x}}^\dagger)$ with $\mathbf{x}, \bar{\mathbf{x}} \in \{\mathbf{d}, \mathbf{b}, \bar{\mathbf{c}}\}$. Since the bath is non-interacting, the action of \mathcal{L} on $|\mathbf{b}^\dagger\rangle$ yields another single-particle operator, never reaching the single-particle irreducible space $\mathbb{W}_{\bar{c}}$, i.e. $\mathcal{L}|\mathbf{b}^\dagger\rangle \in \mathbb{W}_c$ and $\mathcal{L}_{\bar{c}\mathbf{b}} = \mathcal{L}_{\mathbf{b}\bar{c}} = 0$. Since $\mathbb{W}_{\bar{c}}$ is reached only when \mathcal{L} acts on impurity orbitals, the dynamical part of single-particle irreducible self-energy, $\Sigma^{\text{dyn}}(z)$, is non-zero only for impurity orbitals, cf. Eq. (20). For impurity models, the right space of $|\mathbf{q}_1\rangle$ is thus implicitly constrained to the impurity block, where it is non-zero, and likewise for $\Sigma^{\text{dyn}}(z)$.

The full single-particle Green's function, $\mathbf{G} = (\mathbf{c}^\dagger | (z - \mathcal{L})^{-1} | \mathbf{c}^\dagger)$, is an $M \times M$ matrix containing both impurity and bath blocks. However, one typically only works with the impurity Green's function, $\mathbf{G}_{dd} = (\mathbf{d}^\dagger | (z - \mathcal{L})^{-1} | \mathbf{d}^\dagger)$, an $N_d \times N_d$ matrix. Its form, found via Eq. (C4), is

$$\mathbf{G}_{dd}(z) = \left[\mathbf{z} - \epsilon_0 - \mathbf{\Delta}(z) - \Sigma^{\text{dyn}}(z) \right]^{-1}, \quad (48a)$$

$$\epsilon_0 = (\mathbf{d}^\dagger | \mathcal{L} | \mathbf{d}^\dagger), \quad (48b)$$

$$\mathbf{\Delta}(z) = (\mathbf{d}^\dagger | \mathcal{L}_{db} \frac{1}{z - \mathcal{L}_{bb}} \mathcal{L}_{bd} | \mathbf{d}^\dagger), \quad (48c)$$

$$\Sigma^{\text{dyn}}(z) = (\mathbf{d}^\dagger | \mathcal{L}_{d\bar{c}} \frac{1}{z - \mathcal{L}_{\bar{c}\bar{c}}} \mathcal{L}_{\bar{c}d} | \mathbf{d}^\dagger). \quad (48d)$$

The hybridization function $\mathbf{\Delta}(z)$ encodes all relevant information about the impurity-bath coupling.

For the \mathcal{L} -interpolation strategy to be presented in Sec. III, we are only interested in the Liouvillian matrix elements in the single-particle irreducible subspace, to be extracted from $\Sigma^{\text{dyn}}(z)$. These matrix elements cannot be extracted by a direct CFE of $\mathbf{G}_{dd}(z)$, since that mixes single-particle reducible contributions from $\mathbf{\Delta}(z)$ with single-particle irreducible ones from $\Sigma^{\text{dyn}}(z)$. However, the contribution of $\mathbf{\Delta}(z)$ can be subtracted either explicitly (as discussed in App. G) or implicitly, using Kugler's symmetric improved estimator strategy [59, 60] (as done for the results of Secs. IV and V).

H. CFE for NRG spectra

If the self-energy of a quantum impurity model is computed using NRG, as is the case for several results presented in later sections, a complication arises: The spectral function $\mathbf{W}(\omega)$ obtained from NRG possesses long

tails due to the log-Gaussian broadening used to obtain smooth spectral functions from discrete ones. As a result, the moment problem of the measure $\mathbf{W}(\omega)d\omega$ is indeterminate (see App. B), a problem artificially introduced by log-Gaussian broadening. This implies that it is not possible to uniquely determine the self-energy from its CFE coefficients without additional information. Below, we describe how such additional high-frequency information can be introduced via a regularized CFE.

Even without the problem of indeterminate moments, it is often desirable for the regularization scheme to be geared towards extracting low-energy information. Many-body systems often exhibit features that are separated by several orders of magnitude in frequency, and resolving all of those features would require a CFE with exponentially large depth N —unfeasible in numerical practice. Instead, we need a “logarithmic CFE”, featuring CFE coefficients whose magnitudes decrease exponentially with depth N , thus naturally terminating the CFE when N becomes large.

A strategy for constructing CFEs that both regularizes high-energy tails and yields exponentially decreasing CFE coefficients has been described in Ref. 61. There, a logarithmic CFE (log-CFE) was constructed for the hybridization function of an impurity model. This was achieved by an iterative procedure analogous to using Eq. (45), with one crucial difference: after each step the spectrum of the residual function $\mathbf{R}_n(z)$ is split into a high-energy part and a low-energy part, called, “fast” (F) and “slow” (S) modes, respectively, and only the slow modes are used for the next iteration. Here, we adapt that scheme to construct a logarithmic CFE of our self-energy via N one-step Lanczos schemes combined with fast/slow splitting.

We initialize the procedure by setting $\mathbf{R}_0^S(z) = \Sigma^{\text{dyn}}(z)$, i.e. we declare the input self-energy to be “all slow modes”. For iterations $n \geq 1$, we proceed as before for steps (a) to (c), now using $\mathbf{R}_{n-1}^S(z)$ as input, to compute \mathbf{t}_n , ϵ_n and $\mathbf{R}_n(z)$ and obtain the depth-1 CFE

$$\mathbf{R}_{n-1}^S(z) = \mathbf{t}_n \frac{1}{z_n - \mathbf{R}_n(z)} \mathbf{t}_n. \quad (49)$$

Thereafter comes a new step: (d) We split $\mathbf{R}_n(z)$ into “fast” and “slow” contributions, $\mathbf{R}_n(z) = \mathbf{R}_n^F(z) + \mathbf{R}_n^S(z)$, built from the high- or low-energy part of its spectrum,

$$\mathbf{R}_n^{\text{F/S}}(z) = \int_{-\infty}^{\infty} d\omega \frac{w_n^{\text{F/S}}(\omega) \mathbf{R}_n''(\omega)}{z - \omega}. \quad (50)$$

Here, the so-called splitting functions $w_n^{\text{F/S}}(\omega)$ satisfy $w_n^F(\omega) + w_n^S(\omega) = 1$ and monotonically increase/decrease with $|\omega|$ (see below). Then, we use only the slow-mode part, $\mathbf{R}_n^S(z)$, as input for the next iteration. Iterating,

we obtain an exact CFE of the following form:

$$\Sigma^{\text{dyn}}(z) = \begin{array}{ccc} & & \mathbf{t}_1 \\ & \xrightarrow{\quad 1 \quad} & \\ \mathbf{t}_1 & & \\ \xrightarrow{\quad \mathbf{z}_1 - \mathbf{R}_1^{\text{F}}(z) - \mathbf{t}_2 \quad} & & \mathbf{t}_2 \\ & \xrightarrow{\quad 1 \quad} & \\ & & \mathbf{t}_2 \\ & \xrightarrow{\quad \mathbf{z}_2 - \mathbf{R}_2^{\text{F}}(z) - \mathbf{t}_3 \quad} & \\ & & \mathbf{t}_3 \\ & \xrightarrow{\quad \vdots \quad} & \\ & & \mathbf{t}_N \\ & \xrightarrow{\quad 1 \quad} & \\ & & \mathbf{t}_N \\ & \xrightarrow{\quad \mathbf{z}_N - \mathbf{R}_N(z) \quad} & \end{array} \quad (51)$$

Each level contains an explicit fast-mode contribution $\mathbf{R}_n^{\text{F}}(z)$, except the last level, containing the full $\mathbf{R}_N(z)$. Note that $\mathbf{R}_n^{\text{F}}(z)$ will, in general, contain an imaginary part; therefore, some amount of broadening is present at each level, yielding a self-energy with a continuous spectrum. The fact that $\mathbf{R}_n^{\text{F}}(z)$ does not feed into the next iteration in effect regularizes the contribution from high-energy tails of the spectrum of $\mathbf{R}_n(z)$. Nevertheless, the representation (51) is exact—the fast-slow splitting does not neglect any information, it just distributes high- and low-energy information to different parts of the CFE.

To achieve a *logarithmic* CFE whose CFE coefficients decrease exponentially with N , we choose

$$w_n^{\text{S}}(\omega) = \frac{1}{1 + |\omega/\Omega_n|^\tau}, \quad \Omega_n = \Omega_{\text{max}} \Lambda^{1-n}. \quad (52)$$

This box-shaped function has height 1, half-width Ω_n and box corners whose rounding is controlled by $\tau > 2$. The scale Ω_n decreases exponentially with n , and we choose $\Lambda = (\Omega_{\text{max}}/\Omega_{\text{min}})^{1/(N-1)}$ such that Ω_n ranges between specified maximal and minimal values, $\Omega_1 = \Omega_{\text{max}}$ and $\Omega_N = \Omega_{\text{min}}$. The splitting function has weight $\int d\omega w_n^{\text{S}}(\omega) \sim \Lambda^{-n}$, resulting in exponentially decreasing CFE coefficients, $\epsilon_n, \mathbf{t}_n \sim \Lambda^{-n}$ and the weight of the spectrum of \mathbf{R}_n^{F} likewise scales $\sim \Lambda^{-n}$ (see Fig. 10 below, and App. E3 for numerical details.)

III. LIOUVILLIAN INTERPOLATION

In this section, we outline the basic ideas underlying Liouvillian interpolation. We start with a brief discussion of cDMFT approximations and traditional interpolation schemes, then introduce our \mathcal{L} -interpolation scheme. Technical steps are spelled out in detail in Appendix E.

A. Cluster DMFT approximations

We begin with some general remarks. For computations in a real-space basis of N_{latt} lattice sites with M orbitals per site, the self-energy matrix $\tilde{\Sigma}(z)$ is a $N_{\text{latt}}M \times N_{\text{latt}}M$ matrix built from $N_{\text{latt}} \times N_{\text{latt}}$ blocks $[\tilde{\Sigma}(z)]_{\mathbf{r},\mathbf{r}'}$ labeled by site indices, with each block having dimension $M \times M$. If $\tilde{\Sigma}(z)$ is expressed through a block-CFE, its CFE coefficients $\tilde{\epsilon}_n$ and $\tilde{\mathbf{t}}_n$ (i.e. Liouvillian matrix elements) are matrices too, built from $N_{\text{latt}} \times N_{\text{latt}}$ blocks $[\tilde{\epsilon}_n]_{\mathbf{r},\mathbf{r}'}$ and $[\tilde{\mathbf{t}}_n]_{\mathbf{r},\mathbf{r}'}$, each of dimension $M \times M$.

For translationally invariant systems $[\tilde{\Sigma}(z)]_{\mathbf{r},\mathbf{r}'}$ depends only on the difference vector $\boldsymbol{\delta} = \mathbf{r} - \mathbf{r}'$, as do $[\tilde{\epsilon}_n]_{\mathbf{r},\mathbf{r}'}$ and $[\tilde{\mathbf{t}}_n]_{\mathbf{r},\mathbf{r}'}$. Then the Fourier transform block-diagonalizes $\tilde{\Sigma}$ w.r.t. spatial indices:

$$\Sigma_{\mathbf{k}}(z) = \sum_{\boldsymbol{\delta}} [\tilde{\Sigma}(z)]_{\boldsymbol{\delta},\mathbf{0}} e^{-i\mathbf{k}\cdot\boldsymbol{\delta}}. \quad (53)$$

Here, $\Sigma_{\mathbf{k}}(z)$ is shorthand for the diagonal elements of a block-diagonal matrix with elements $[\Sigma(z)]_{\mathbf{k},\mathbf{k}'} = \delta_{\mathbf{k}\mathbf{k}'} \Sigma_{\mathbf{k}}(z)$ obtained by viewing the Fourier transform as a basis transformation $\Sigma = \mathbf{U}\tilde{\Sigma}\mathbf{U}^\dagger$ with matrix entries $[\mathbf{U}]_{\mathbf{k},\mathbf{r}} = e^{-i\mathbf{k}\cdot\mathbf{r}}/\sqrt{N_{\text{latt}}}$. The sum runs over all distinct difference vectors $\boldsymbol{\delta}$ between two lattice sites. (Since the lattice includes site $\mathbf{0}$, this is equivalent to summing over all lattice sites.) For given \mathbf{k} , $\Sigma_{\mathbf{k}}(z)$ is an $M \times M$ matrix, as are its CFE coefficients,

$$\epsilon_{\mathbf{k}n} = \sum_{\boldsymbol{\delta}} [\tilde{\epsilon}_n]_{\boldsymbol{\delta},\mathbf{0}} e^{-i\mathbf{k}\cdot\boldsymbol{\delta}}, \quad \mathbf{t}_{\mathbf{k}n} = \sum_{\boldsymbol{\delta}} [\tilde{\mathbf{t}}_n]_{\boldsymbol{\delta},\mathbf{0}} e^{-i\mathbf{k}\cdot\boldsymbol{\delta}}. \quad (54)$$

In conventional single-site DMFT, the ‘‘impurity’’ is a single lattice site self-consistently embedded in its surrounding, the real-space self-energy is local, $[\tilde{\Sigma}(z)]_{\mathbf{r},\mathbf{r}'} = \delta_{\mathbf{r},\mathbf{r}'} \Sigma(z)$, and the momentum-space self-energy is \mathbf{k} -independent, $\Sigma_{\mathbf{k}}(z) = \Sigma(z)$. The same is true for its $n > 0$ CFE coefficients: $[\tilde{\epsilon}_n]_{\boldsymbol{\delta},\mathbf{0}} = \delta_{\boldsymbol{\delta},\mathbf{0}} \epsilon_n$ and $\epsilon_{\mathbf{k}n} = \epsilon_n$, likewise for $\tilde{\mathbf{t}}_n$ and $\mathbf{t}_{\mathbf{k}n}$. Single-DMFT thus approximates the single-particle irreducible part of the Liouvillian of the lattice model by that of an effective impurity model.

For cellular DMFT (CDMFT), the real-space lattice is tiled into identical clusters, each containing N_c sites. The ‘‘impurity’’ is one of these clusters, which we denote by \mathcal{C} , and the real-space self-energy $[\tilde{\Sigma}(z)]_{\mathbf{r},\mathbf{r}'}$ is taken to be localized on \mathcal{C} (with open boundary conditions): it contains non-local contributions only when both position arguments are on the same cluster, while intercluster terms are set to zero: $[\tilde{\Sigma}(z)]_{\mathbf{r},\mathbf{r}'} \neq 0$ only when $\mathbf{r}, \mathbf{r}' \in \mathcal{C}$. Therefore, the same is true for its $n > 0$ CFE coefficients $[\tilde{\epsilon}_n]_{\mathbf{r},\mathbf{r}'}$ and $[\tilde{\mathbf{t}}_n]_{\mathbf{r},\mathbf{r}'}$. CDMFT thus explicitly breaks translation invariance.

By contrast, the dynamical cluster approximation (DCA) retains translational invariance at the cost of using coarse-grained momentum variables. The Brillouin zone (BZ) is partitioned into equally-sized patches labeled by patch momenta \mathbf{K} . The momentum-space self-energy is block-diagonal in \mathbf{K} , with diagonal blocks $\Sigma_{\mathbf{K}}(z)$, each of dimension $M \times M$. They are taken to depend only on the patch momentum \mathbf{K} and are \mathbf{k} -independent within each patch, with discontinuous jumps between patches. $\Sigma_{\mathbf{K}}(z)$ mimics the patch average of $\Sigma_{\mathbf{k}}(z)$. The same is true for its CFE coefficients, denoted $\epsilon_{\mathbf{K}n}$ and $\mathbf{t}_{\mathbf{K}n}$.

interpolation schemes seek to restore translational invariance for CDMFT self-energies or a smooth momentum dependence for DCA self-energies. (As mentioned earlier, for CDMFT, our use of ‘‘interpolation’’ should be understood to refer to ‘‘periodization’’.) In Sec. III C, we

propose \mathcal{L} -interpolation as a unifying scheme, applicable to both CDMFT and DCA, capable of achieving these goals. Before that, in Sec. III B we briefly review the traditional schemes, Σ -, M -, and G -interpolation, since we will later present results comparing the performance of all these schemes.

B. Traditional interpolation

CDMFT: When applying traditional interpolation to our CDMFT data, we use a superlattice average [11] to guarantee causality. The superlattice is constructed translating a cluster \mathcal{C} to tile the original lattice, treating \mathcal{C} as a super-site carrying internal degrees of freedom. To interpolate a z -dependent $[\tilde{\mathbf{Q}}(z)]_{\mathbf{r},\mathbf{r}'}$ obtained from CDMFT as a real-space matrix, where $\tilde{\mathbf{Q}}$ stands for the self-energy $\tilde{\Sigma}$, cumulant $\tilde{\mathbf{M}}$ or Green's function $\tilde{\mathbf{G}}$, we make the CDMFT interpolation Ansatz

$$\mathbf{Q}_{\mathbf{k}}(z) \simeq \sum_{\delta} \bar{\mathbf{Q}}_{\delta}(z) e^{-i\mathbf{k}\cdot\delta}. \quad (55)$$

We estimate $\bar{\mathbf{Q}}_{\delta}(z)$ using a superlattice average [11]

$$\bar{\mathbf{Q}}_{\delta}(z) = \frac{1}{N_c} \sum_{\mathbf{r}' \in \mathcal{C}} [\tilde{\mathbf{Q}}(z)]_{\mathbf{r}',\mathbf{r}'+\delta}, \quad (56)$$

where the sum runs over a cluster with N_c sites. For $\tilde{\mathbf{Q}} = \tilde{\Sigma}$ or $\tilde{\mathbf{M}}$ (but not for $\tilde{\mathbf{G}}$), terms in Eq. (56) having $\mathbf{r}' + \delta \notin \mathcal{C}$ are zero. For $\tilde{\mathbf{Q}} = \tilde{\Sigma}$ or $\tilde{\mathbf{M}}$ (but not $\tilde{\mathbf{G}}$), we therefore have $\bar{\mathbf{Q}}_{\delta} = \mathbf{0}$ if $|\delta|$ exceeds the cluster size. For $\tilde{\mathbf{Q}} = \tilde{\Sigma}$ or $\tilde{\mathbf{M}}$, Eq. (55) thus is equivalent to a short-range-truncated Fourier Ansatz of the form (2), while for $\tilde{\mathbf{Q}} = \tilde{\mathbf{G}}$, Eq. (55) involves no short-ranged truncation.

Superlattice averaging as described above leads to causal self-energies or Green's functions [11]. However, these may become non-causal if the superlattice average is replaced, for instance, by a cluster average, i.e. if in Eq. (56) $1/N_c$ is replaced by $1/N_{\delta}$, where N_{δ} is the number of pairs of sites in the cluster having distance δ .

DCA: In DCA, the Brillouin zone (BZ) is partitioned into N_p disjoint patches labeled by a set of representative momenta $\{\mathbf{K}\}$. We write $V_{\text{BZ}} = \cup_{\mathbf{K}} V_{\mathbf{K}}$ for the union of their domains, and $\sum_{\mathbf{K}} |V_{\mathbf{K}}| = |V_{\text{BZ}}|$ for the sum of their volumes. The output of DCA computations are translationally invariant, momentum patch-averaged quantities.

$$\mathbf{Q}_{\mathbf{K}}(z) = \begin{cases} \Sigma_{\mathbf{K}}(z), \\ \mathbf{M}_{\mathbf{K}}(z) = [z + \mu - \Sigma_{\mathbf{K}}(z)]^{-1}. \end{cases} \quad (57)$$

These must be combined to yield a function $\mathbf{Q}_{\mathbf{k}}(z)$ defined throughout the BZ. ‘‘Bare’’ (non-interpolated) DCA does this using step functions, $\mathbf{Q}_{\mathbf{k}}(z) = \sum_{\mathbf{K}} \theta_{\mathbf{k},\mathbf{K}} \mathbf{Q}_{\mathbf{K}}(z)$, where $\theta_{\mathbf{k},\mathbf{K}} = 1$ if \mathbf{k} lies in patch \mathbf{K} and zero otherwise, resulting in artificial discontinuities in momentum space. The interpolation of $\mathbf{Q}_{\mathbf{K}}(z)$ amounts

to smearing out the discontinuities through an DCA interpolation Ansatz of the form

$$\mathbf{Q}_{\mathbf{k}}(z) = \sum_{\mathbf{K}} \alpha_{\mathbf{k},\mathbf{K}} \mathbf{Q}_{\mathbf{K}}(z), \quad (58)$$

where for each patch \mathbf{K} the ‘‘form factor’’ $\alpha_{\mathbf{k},\mathbf{K}}$ is an interpolation function of \mathbf{k} defined on the entire BZ. Various choices for the form factors can be found in the literature, including splines [5] and low-order Fourier-Ansätze [62]. If $\mathbf{Q}_{\mathbf{K}}(z)$ depends on z (e.g. when it stands for $\Sigma_{\mathbf{K}}(z)$ or $\mathbf{M}_{\mathbf{K}}(z)$), interpolation can cause causality problems; a heuristic strategy for ameliorating these is to choose the form factors such that $\alpha_{\mathbf{k},\mathbf{K}} = 1$ [1, 6, 7].

Canonical DCA interpolation: For Liouvillian interpolation, the quantities to be interpolated are z -independent Liouvillian matrix elements, hence causality concerns do not arise (with one small caveat, discussed later). This affords us the freedom to focus on a formulation of a truncated Fourier expansion that is particularly well suited for our purposes. We will call it ‘‘canonical’’ DCA interpolation, since it ensures that the resulting $\mathbf{Q}_{\mathbf{k}}(z)$ possesses three canonical (clearly desirable) properties: (i) $\mathbf{Q}_{\mathbf{k}}(z)$ is invariant under the point-group symmetry operations (rotations, reflections, inversions) that leave the patches invariant. (ii) Averaging $\mathbf{Q}_{\mathbf{k}}(z)$ over patch \mathbf{K}' yields $\mathbf{Q}_{\mathbf{K}'}(z)$, i.e. $\int_{V_{\mathbf{K}'}} \frac{d\mathbf{k}}{|V_{\mathbf{K}'}|} \mathbf{Q}_{\mathbf{k}}(z) = \mathbf{Q}_{\mathbf{K}'}(z)$. (iii) If $\mathbf{Q}_{\mathbf{K}}(z)$ does not depend on \mathbf{K} , $\mathbf{Q}_{\mathbf{K}}(z) = \mathbf{Q}(z)$, then $\mathbf{Q}_{\mathbf{k}}(z) = \mathbf{Q}(z)$. Below, we present a form factor construction that ensures these canonical properties. It expresses the form factors as linear combinations of lattice harmonics, using only ones that are invariant under the symmetry operations that leave all patches invariant. This construction is not new, but, for completeness, we explain its rationale nevertheless. (For some background on the definition of lattice harmonics, see App. F.)

For canonical DCA interpolation, we expand $\alpha_{\mathbf{k},\mathbf{K}}$ as

$$\alpha_{\mathbf{k},\mathbf{K}} = \sum_{j=1}^{N_p} \phi_{\mathbf{k},j} \Psi_{j,\mathbf{K}}. \quad (59)$$

Here, the $\phi_{\mathbf{k},j}$ are real-valued lattice harmonics chosen according to a criterion described below; j enumerates the chosen ones in order of increasing complexity, with $\phi_{\mathbf{k},1} = 1$; and the $\Psi_{j,\mathbf{K}}$ are real expansion coefficients, to be determined in manner described below.

To ensure property (i), we include in Eq. (59) only lattice harmonics $\phi_{\mathbf{k},j}$ that are invariant under the point group symmetries of the patches; that immediately implies the same for $\alpha_{\mathbf{k},\mathbf{K}}$. (The choice of $\phi_{\mathbf{k},j}$ may also depend on additional details of the chosen patching scheme and the physics it attempts to capture. A concrete example is given in Sec. V, where we consider 4-patch DCA results for a Hubbard model on a 2D square lattice and use $\phi_{\mathbf{k},j}$ functions constructed via Eq. (F4) in App. F.)

To ensure property (ii), we impose the condition

$$\int_{V_{\mathbf{K}'}} \frac{d\mathbf{k}}{|V_{\mathbf{K}'}|} \alpha_{\mathbf{k},\mathbf{K}} = \delta_{\mathbf{K}',\mathbf{K}}. \quad (60)$$

Inserting Ansatz (59) into condition (60) we obtain

$$\sum_{j=1}^{N_p} \Phi_{\mathbf{K}',j} \Psi_{j,\mathbf{K}} = \delta_{\mathbf{K}',\mathbf{K}}, \quad (61)$$

where the coefficients $\Phi_{\mathbf{K}',j} = \int_{V_{\mathbf{K}'}} \frac{d\mathbf{k}}{|V_{\mathbf{K}'}|} \phi_{\mathbf{k},j}$ encode information about patch shapes. Viewing Eq. (61) as an $N_p \times N_p$ matrix equation, $\Phi \cdot \Psi = \mathbb{1}$, we find $\Psi_{j,\mathbf{K}} = (\Phi^{-1})_{j,\mathbf{K}}$ (assuming Φ^{-1} exists). This completes the construction of the form factors $\alpha_{\mathbf{k},\mathbf{K}}$. Note that they are unchanged if the $\phi_{\mathbf{k},j}$ functions are replaced by linearly transformed combinations $\sum_{j'} \phi_{\mathbf{k},j'} T_{j'j}$ (assuming T is invertible), because by Eq. (61) that would just result in inversely transformed coefficients $\sum_{j''} T_{j''j}^{-1} \Psi_{j'',\mathbf{K}}$.

Property (iii) holds, too, since the form factors satisfy

$$\sum_{\mathbf{K}} \alpha_{\mathbf{k},\mathbf{K}} = 1 \quad (62)$$

by construction. This can be seen as follows. The only lattice harmonic whose BZ integral is nonzero is the constant one: $\int_{\text{BZ}} d\mathbf{k} \phi_{\mathbf{k},j} = |V_{\text{BZ}}| \delta_{j,1}$. Therefore,

$$\sum_{\mathbf{K}'} |V_{\mathbf{K}'}| \Phi_{\mathbf{K}',j} = \sum_{\mathbf{K}'} \int_{V_{\mathbf{K}'}} d\mathbf{k} \phi_{\mathbf{k},j} = |V_{\text{BZ}}| \delta_{j,1}. \quad (63)$$

Moreover, defining $\psi_j = \sum_{\mathbf{K}} \Psi_{j,\mathbf{K}}$, we find from Eq. (61),

$$\sum_{\mathbf{K}'} |V_{\mathbf{K}'}| \sum_{j=1}^{N_p} \Phi_{\mathbf{K}',j} \psi_j = \sum_{\mathbf{K}',\mathbf{K}} |V_{\mathbf{K}'}| \delta_{\mathbf{K}',\mathbf{K}} = |V_{\text{BZ}}|. \quad (64)$$

Inserting Eq. (63) into (64) we find $\psi_1 = 1$. Summing Eq. (61) over $\sum_{\mathbf{K}}$ we obtain $\sum_j \Phi_{\mathbf{K}',j} \psi_j = 1$, and since $\Phi_{\mathbf{K}',1} \psi_1 = 1 \cdot 1$, this implies $\sum_{j>1} \Phi_{\mathbf{K}',j} \psi_j = 0$. This linear combination of columns of Φ , which are linearly independent since was assumed to Φ^{-1} exist, can vanish only if all coefficients $\psi_{j>1}$ vanish, implying $\psi_j = \delta_{j,1}$. Thus $\sum_{\mathbf{K}} \alpha_{\mathbf{k},\mathbf{K}} = \sum_j \phi_{\mathbf{k},j} \psi_j = \phi_{\mathbf{k},1} = 1$, proving Eq. (62).

Finally, we remark that the interpolation Ansatz of Eqs. (58) and (59) for $\mathbf{Q}_{\mathbf{k}}(z)$ and $\alpha_{\mathbf{k},\mathbf{K}}$ can be expressed as a truncated Fourier expansion having the form of Eq. (2), see App. F for details.

If canonical DCA interpolation is used to interpolate the self-energy or the cumulant, the resulting functions $\mathbf{Q}_{\mathbf{k}}(z)$ and $\mathbf{M}_{\mathbf{k}}(z)$ may exhibit frequency-dependent ringing effects that lead to violations of causality [63]. One possible remedy is to use a modified version of Eq. (59),

$$\alpha_{\mathbf{k},\mathbf{K}}^{\text{mod}} = \sum_{j=1}^{N_p} \frac{1}{N_j} \phi_{\mathbf{k},j} \Psi_{j,\mathbf{K}}, \quad (65)$$

where ϕ and Ψ are defined as above, and N_j is the number of sites in the real-space orbit O_j associated with $\phi_{\mathbf{k},j}$ (see App. F, Eq. (F4) for details). The factor $1/N_j$ reduces the contribution of the non-local Fourier coefficients $\phi_{\mathbf{k},j>1}$ relative to the local one, $\phi_{\mathbf{k},1}$, thereby counteracting their causality-violating tendencies. However,

it must be acknowledged that this prescription is somewhat arbitrary and spoils the above-mentioned canonical property (ii).

An alternative fix to ensure causality, already mentioned above, is to drop Eq. (60) and instead enforce $[\alpha_{\mathbf{k},\mathbf{K}}]_{\mathbf{k}=\mathbf{K}} = 1$ [1, 6, 7]. However, this prescription, too, involves arbitrariness, since the choice $\mathbf{k} = \mathbf{K}$ singles out one point in the patch and contains no information about the actual shape of the patch. Moreover, typically it does not guarantee canonical property (ii).

By contrast, when DCA interpolation is performed by \mathcal{L} -interpolation, as presented in the next sections, such problems do not arise. Since \mathcal{L} is Hermitian and its matrix elements are frequency-independent, \mathcal{L} -interpolation respects causality by construction. It can thus be used in conjunction with canonical DCA interpolation, thus also ensuring the canonical properties (i)-(iii).

C. \mathcal{L} -interpolation

Conceptually, our \mathcal{L} -interpolation scheme is very simple: we compute the dynamical part of the self-energy, construct its CFE coefficients, and interpolate the latter using the same strategy as in Sec. III B—but now applied to n -dependent coefficients instead of z -dependent functions, which makes all the difference for ensuring causality. Concretely, we proceed as follows.

CDMFT: Using the Lanczos scheme of Sec. II E, we construct the CFE of the dynamical part of the CDMFT self-energy, $[\Sigma^{\text{dyn}}(z)]_{\mathbf{r},\mathbf{r}'}$ (see App. E 1 for numerical details), obtaining the corresponding hermitian CFE coefficients $[\tilde{\epsilon}_n]_{\mathbf{r},\mathbf{r}'}$ and $[\tilde{\mathbf{t}}_n]_{\mathbf{r},\mathbf{r}'}$. From these we estimate hermitian, real-space Liouvillian matrix elements of the lattice model using superlattice averaging as in Eq. (56):

$$\bar{\epsilon}_{\delta n} = \frac{1}{N_c} \sum_{\mathbf{r}' \in C} [\tilde{\epsilon}_n]_{\mathbf{r},\mathbf{r}'+\delta}, \quad \bar{\mathbf{t}}_{\delta n} = \frac{1}{N_c} \sum_{\mathbf{r}' \in C} [\tilde{\mathbf{t}}_n]_{\mathbf{r},\mathbf{r}'+\delta}. \quad (66)$$

They are cluster-range-limited, vanishing if $|\delta|$ exceeds the cluster size. Note that $\bar{\epsilon}_{\delta n} = \bar{\epsilon}_{-\delta n}^\dagger$ since by construction, $\epsilon_n = \epsilon_n^\dagger$, implying $[\tilde{\epsilon}_n]_{\mathbf{r},\mathbf{r}'} = [\tilde{\epsilon}_n^\dagger]_{\mathbf{r}',\mathbf{r}}$ for its matrix elements. Likewise for \mathbf{t}_n .

Finally, we define CDMFT-interpolated CFE coefficients in analogy to Eq. (55):

$$\epsilon_{\mathbf{k}n} \simeq \sum_{\delta} \bar{\epsilon}_{\delta n} e^{-i\mathbf{k}\cdot\delta}, \quad \mathbf{t}_{\mathbf{k}n} \simeq \sum_{\delta} \bar{\mathbf{t}}_{\delta n} e^{-i\mathbf{k}\cdot\delta}. \quad (67)$$

By construction, we have $\epsilon_{\mathbf{k}n} = \epsilon_{\mathbf{k}n}^\dagger$, $\mathbf{t}_{\mathbf{k}n} = \mathbf{t}_{\mathbf{k}n}^\dagger$.

The reason why in this work we use using superlattice averaging in Eq. (66) to estimate $\bar{\epsilon}_{\delta n}$ and $\bar{\mathbf{t}}_{\delta n}$ is that this provided the most favorable comparisons to benchmark results obtained using MPS methods (see Sec. IV). However, instead of superlattice averaging, one could in Eq. (66) also use cluster averaging, or some other scheme, as long as $\bar{\epsilon}_{\delta n} = \bar{\epsilon}_{-\delta n}^\dagger$ and $\bar{\mathbf{t}}_{\delta n} = \bar{\mathbf{t}}_{-\delta n}^\dagger$, ensuring that

$\epsilon_{\mathbf{k}n}$ and $\mathbf{t}_{\mathbf{k}n}$ and therefore also the CDMFT-interpolated Liouvillian are hermitian, leading to causal Green's functions and self-energies after interpolation. This is in stark contrast to periodization schemes based on frequency-dependent quantities such as the self-energy or the cumulant, as discussed above.

DCA: Here, we use the Lanczos scheme of Sec. II E to construct CFE coefficients $\epsilon_{\mathbf{K}n}$ and $\mathbf{t}_{\mathbf{K}n}$ from the dynamical part of the patch self-energies $\Sigma_{\mathbf{K}}^{\text{dyn}}(z)$. We then apply the canonical DCA interpolation of Sec. III B to the CFE coefficients, with $\alpha_{\mathbf{k},\mathbf{K}}$ constructed according to Eqs. (59)–(61), to define DCA-interpolated coefficients,

$$\epsilon_{\mathbf{k}n} = \sum_{\mathbf{K}} \alpha_{\mathbf{k},\mathbf{K}} \epsilon_{\mathbf{K}n}, \quad \mathbf{t}_{\mathbf{k}n} = \sum_{\mathbf{K}} \alpha_{\mathbf{k},\mathbf{K}} \mathbf{t}_{\mathbf{K}n}. \quad (68)$$

They are hermitian, since the CFE coefficients $\epsilon_{\mathbf{K}n}$ and $\mathbf{t}_{\mathbf{K}n}$ are hermitian by construction, and the $\alpha_{\mathbf{k},\mathbf{K}}$ are real.

Having constructed the interpolated coefficients $\epsilon_{\mathbf{k}n}$ and $\mathbf{t}_{\mathbf{k}n}$ from CDMFT or DCA as described above, we are ready to assemble the corresponding interpolated dynamical self-energy $\Sigma_{\mathbf{k}}^{\text{dyn}}(z)$. If the Lanczos iteration for finding CFE coefficients terminates automatically, i.e. for a discrete $\mathcal{L}_{\bar{c}\bar{c}}$ that is fully represented by Eq. (28), the CFE (41) is an exact representation of $\Sigma^{\text{dyn}}(z)$. Its interpolated version, and in turn the interpolated self-energy $\Sigma_{\mathbf{k}}(z)$, follows from inserting the interpolated matrix elements $\epsilon_{\mathbf{k}n}$ and $\mathbf{t}_{\mathbf{k}n}$ into Eq. (41), thereby defining

$$\Sigma_{\mathbf{k}}^{\text{dyn}}(z) = \mathbf{t}_{\mathbf{k}1} \frac{1}{z_{\mathbf{k}1} - \mathbf{t}_{\mathbf{k}2} \frac{1}{z_{\mathbf{k}2} - \dots - \mathbf{t}_{\mathbf{k}N} \frac{1}{z_{\mathbf{k}N}} \mathbf{t}_{\mathbf{k}N}}} \mathbf{t}_{\mathbf{k}1}, \quad (69)$$

with $\mathbf{z}_{\mathbf{k}n} = \mathbf{z} - \epsilon_{\mathbf{k}n}$. If the CFE is terminated by a residual function $\mathbf{R}_N(z)$ as in Eq. (42), we construct its interpolated version $\mathbf{R}_{\mathbf{k}N}(z)$ via the traditional for CDMFT or DCA approaches of Sec. III B, using

$$[\tilde{\mathbf{Q}}(z)]_{\mathbf{r},\mathbf{r}'} = [\tilde{\mathbf{R}}_N(z)]_{\mathbf{r},\mathbf{r}'}, \quad \mathbf{Q}_{\mathbf{K}}(z) = \mathbf{R}_{\mathbf{K}N}(z), \quad (70)$$

respectively, and set $\mathbf{z}_{\mathbf{k}N} = \mathbf{z} - \epsilon_{\mathbf{k}N} - \mathbf{R}_{\mathbf{k}N}(z)$ in (69). For an NRG self-energy whose CFE involves F/S-splitting (cf. Sec. II H), we similarly interpolate the fast-mode terms $[\tilde{\mathbf{R}}_n^{\text{F}}(z)]_{\mathbf{r},\mathbf{r}'}$ or $\mathbf{R}_{\mathbf{K}n}^{\text{F}}(z)$ for CDMFT or DCA, and set $\mathbf{z}_{\mathbf{k}n} = \mathbf{z} - \epsilon_{\mathbf{k}n} - \mathbf{R}_{\mathbf{k}n}^{\text{F}}(z)$ for $n < N$ in (69).

We note that our suggestion to interpolate the z -dependent functions $\mathbf{R}_n^{(\text{F})}(z)$ using traditional schemes, can, in principle, lead to similar causality violations for $\Sigma_{\mathbf{k}}^{\text{dyn}}(z)$ as those discussed in Sec. III B for traditional periodizations of $\Sigma_{\mathbf{k}}(z)$ or $\mathbf{M}_{\mathbf{k}}(z)$. However, for the computations performed for this work, we find that the functions $\mathbf{R}_n^{(\text{F})}(z)$ are quite local, and that essentially all significantly non-local features of $\Sigma^{\text{dyn}}(z)$ are encoded in ϵ_n and \mathbf{t}_n , see Sec. V A. As a result, we did not encounter any violations of causality. (In case DCA computations

do yield causality violations, we recommend using $\alpha_{\mathbf{k},\mathbf{K}}^{\text{mod}}$ of Eq. (65) when interpolating $\mathbf{R}_n^{(\text{F})}(z)$, thereby reducing the contribution of non-local Fourier coefficients.)

D. Discrete self-energies: interpolation before broadening

If the impurity solver used within cDMFT discretizes the bath, then both spectral functions and self-energies are discrete functions of frequency. They have to be broadened to estimate the corresponding continuous functions of the impurity model with a continuous bath. For some impurity solvers, such as NRG, discrete spectral functions are computed and broadened, but discrete self-energies are typically unavailable (see, however, Ref. 60). If discrete self-energies *are* available, it is advantageous to apply interpolation schemes directly to the discrete ones and broaden them *after* interpolation. We have done that for the CDMFT data in Sec. IV B, which was computed with a tangent-space Krylov (TaSK) impurity solver [64] where discrete self-energies are available. The same goes for the exact diagonalization data shown in App. G.

The discrete self-energy has a finite CFE, which can usually be computed exactly (otherwise, the discussion that follows does not apply). Interpolating the CFE coefficients according to our discussion above yields periodic self-energy with a discrete frequency dependence. To obtain a continuous frequency dependence, we simply broaden the discrete periodic self-energy for every \mathbf{k} -point with the same broadening scheme used within the cDMFT calculation.

We close this section with a final remark. After the dynamical part of the cDMFT self-energy has been interpolated, DMFT defines the lattice Green's function as

$$\mathbf{G}_{\mathbf{k}}(z) = \frac{1}{\mathbf{z} - \epsilon_{\mathbf{k}} - \Sigma_{\mathbf{k}}^{\text{HF}} - \Sigma_{\mathbf{k}}^{\text{dyn}}(z)}. \quad (71)$$

Here $\epsilon_{\mathbf{k}}$, representing the free single-particle Hamiltonian, is exact and does not require interpolation. The Hartree-Fock term $\Sigma_{\mathbf{k}}^{\text{HF}}$, unlike $\epsilon_{\mathbf{k}}$, depends on the density matrix used to evaluate inner products. For purely local interactions, as treated in this work, the HF term is local and identical to that of the impurity model, $\Sigma_{\mathbf{k}}^{\text{HF}} = \Sigma^{\text{HF}}$, so it does not need to be interpolated. With non-local interactions, however, the HF term does acquire a \mathbf{k} -dependence (even without interpolation) that is only partially captured by the impurity model: it arises from lattice expectation values computed via \mathbf{k} -sums over corresponding lattice Green's functions. However, for CDMFT/DCA, these lattice expectation values are generally not fully periodic/continuous, leading to a non-periodic/npn-continuous HF contribution. To resolve this, we propose to recompute the HF term after interpolating the single-particle irreducible matrix elements, and to iterate this until self-consistency.

IV. BENCHMARK: CDMFT INTERPOLATION IN THE 1D HUBBARD MODEL

This section is devoted to benchmarking the \mathcal{L} -interpolation of CDMFT data in a context in which essentially exact reference data is also available. By comparing the results of G -, Σ -, M - and \mathcal{L} -interpolation schemes to the reference data, we establish which interpolation schemes perform best. (Reminder: in this section, “interpolation” stands for “periodization”, i.e. real-space interpolation.)

We consider the one-dimensional Hubbard model,

$$H = - \sum_{\ell\sigma} (c_{\ell\sigma}^\dagger c_{\ell+1\sigma} + \text{h.c.}) - \mu \sum_{\ell\sigma} n_{\ell\sigma} + U \sum_{\ell} n_{\ell\uparrow} n_{\ell\downarrow}, \quad (72)$$

for a chain of L sites. This model is challenging for DMFT-type approaches, which are controlled by the inverse dimensionality of the lattice model. On the other hand, this model can be efficiently treated using matrix product state (MPS) techniques. In Sec. IV A, we use MPS techniques to compute and investigate the full frequency *and* momentum dependence of its single-particle spectral function and self-energy. These results are numerically (almost) exact, and we will view them as “ground truth” for this model. We use our MPS results (i) to show that \mathcal{L} is indeed more short-ranged than Σ or M ; and (ii) as benchmark data against which we subsequently, in Sec. IV B, compare interpolated CDMFT results obtained using several different schemes: G -, Σ -, M - and \mathcal{L} -interpolation.

A. MPS analysis

For our MPS-based analysis, we compute the ground state of Hubbard chain of $L = 50$ sites with $U = 5$ and $\mu = -U/2$ (half-filling) using the density matrix renormalization group (DMRG). We then compute the single-particle spectral function $A_k(\omega)$ associated with the retarded correlator

$$\tilde{G}_k^{\text{R}}(t) = -i\theta(t) \langle \{c_k(0), c_k^\dagger(-t)\} \rangle, \quad (73)$$

where $c_k = \frac{1}{\sqrt{L}} \sum_{\ell=1}^L e^{-ik\ell} c_{\ell\sigma}$, using the tangent-space Krylov (TaSK) approach [64]. TaSK yields the spectral function in the form of a discrete Lehmann representation, $A_k^{\text{disc}}(\omega)$. The eigenstates and eigenenergies involved therein are computed via a Lanczos scheme that constructs a Krylov basis within the 1-site tangent space of the ground state. $A_k^{\text{disc}}(\omega)$ is a discrete function of ω (since the chain has finite length). We broaden it to obtain $A_k(\omega)$ as a smooth function of ω . For details see App. H and Ref. 64.

From $A_{\mathbf{k}}(\omega)$ we compute $G_{\mathbf{k}}(\omega)$ (8a), and then $\Sigma_{\mathbf{k}}(\omega)$ and $M_{\mathbf{k}}(\omega)$ via Eqs. (1). The resulting spectral function $A_k(\omega)$, self-energy $\Sigma_k(\omega)$ and cumulant $M_k(\omega)$ are

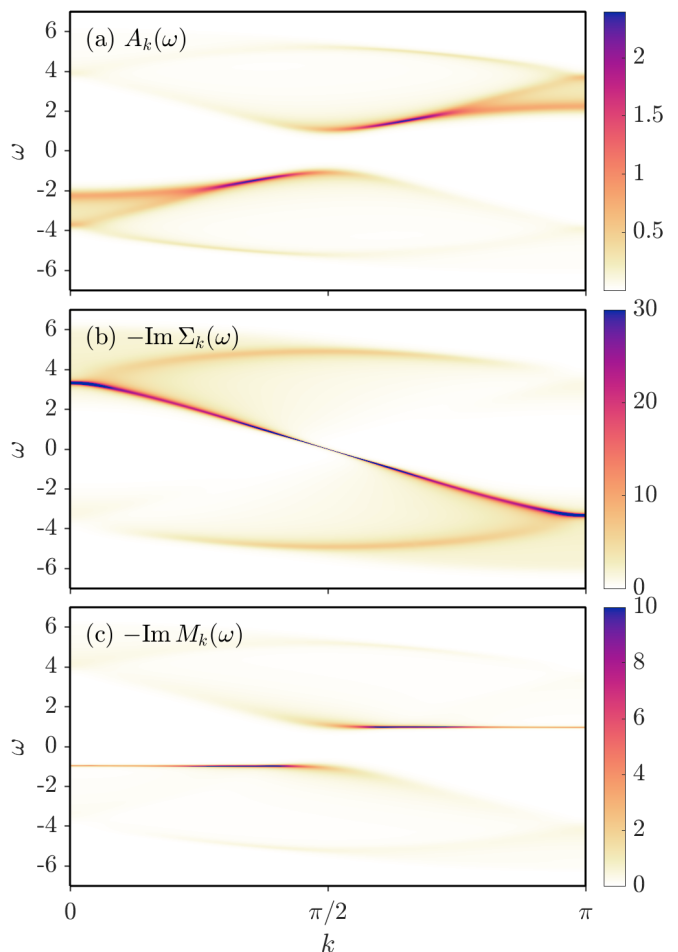


FIG. 1. (a) Spectral function, (b) self-energy and (c) cumulant computed with the TaSK method for a $L = 50$ Hubbard model.

shown in Figs. 1(a), (b) and (c), respectively. As expected, $A_k(\omega)$ exhibits a Mott gap while $\Sigma_k(\omega)$ has a dispersive pole. The main feature of $M_k(\omega)$, on the other hand, is a k -independent peak at negative frequencies for $0 \leq k \leq \pi/2$ and another flat peak at positive frequencies at $\pi/2 \leq k \leq \pi$. Thus, the features of $M_k(\omega)$ are significantly less dispersive than those of both $A_k(\omega)$ and $\Sigma_k(\omega)$. As a result, M -interpolation is expected to yield better results than Σ -interpolation for the present parameters where the model is in a Mott phase. This aligns with findings in the literature [11].

In order to test more quantitatively which interpolation scheme may yield the best outcomes, we Fourier-transform to position space and compute the Fourier coefficients

$$\tilde{\Sigma}_r(\omega) = \frac{1}{L} \sum_k e^{ikr} \Sigma_k(\omega), \quad \tilde{M}_r(\omega) = \frac{1}{L} \sum_k e^{ikr} M_k(\omega). \quad (74)$$

For $r \leq 5$, the Fourier coefficients $\tilde{\Sigma}_r(\omega)$ and $\tilde{M}_r(\omega)$ are shown in Fig. 3(a) and (b), respectively. The maximal

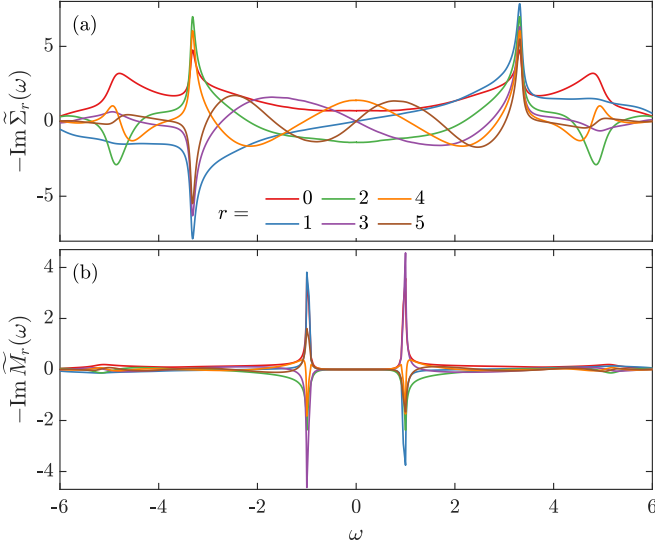


FIG. 2. The first six Fourier coefficients of the imaginary part of (a) the self-energy of Fig. 1(b) and (b) the cumulant of Fig. 1(c).

absolute amplitude of $\tilde{M}_r(\omega)$ clearly decays faster with increasing r than that of $\tilde{\Sigma}_r(\omega)$. This suggests that here M -interpolation will outperform Σ -interpolation. Indeed, we confirm this explicitly below.

Now consider the truncated Fourier series,

$$\Sigma_k^{[R]}(\omega) = \sum_{r=0}^R \tilde{\Sigma}_r(\omega) \cos(kr), \quad (75a)$$

$$M_k^{[R]}(\omega) = \sum_{r=0}^R \tilde{M}_r(\omega) \cos(kr). \quad (75b)$$

Here, r plays the role of δ from Sec. III. (Compared

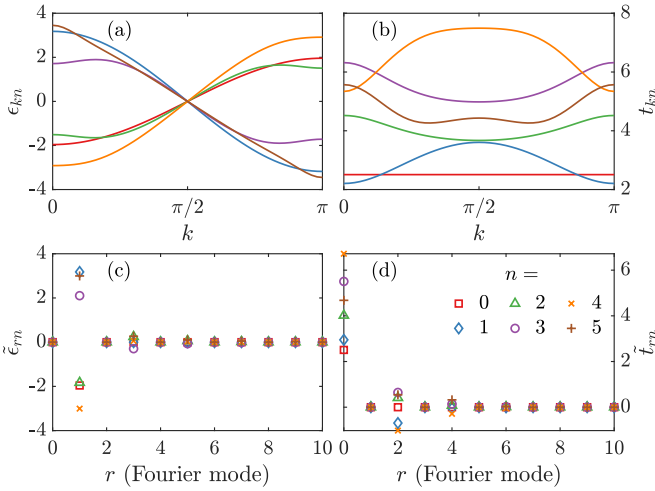


FIG. 3. (a,b) Matrix elements ϵ_{kn} and t_{kn} of \mathcal{L} , extracted via CFE from the spectral data in Fig. 1. (c,d) The corresponding Fourier coefficients $\tilde{\epsilon}_{rn}$ and \tilde{t}_{rn} up to order $r = 10$. The color scheme of panel (d) applies to all panels.

to Eq. (53), we combined terms with $e^{\pm ikr}$ in the sum above, so that the magnitude of the non-local coefficients $\tilde{\Sigma}_r(\omega)$ with $r > 0$ is directly comparable to the local coefficient $\tilde{\Sigma}_0(\omega)$, and similarly for M .) Such truncated Fourier series will generically lead to non-causal features (positive imaginary parts for $\Sigma_k(\omega)$ or $M_k(\omega)$) due to ringing [63] because the truncation discards ω -dependent terms. Consider, for instance, approximating $\Sigma_k(\omega)$ by the first two terms of its Fourier expansion,

$$\Sigma_k^{[1]}(\omega) = \tilde{\Sigma}_0(\omega) + \cos(k) \tilde{\Sigma}_1(\omega). \quad (76)$$

As shown in Fig. 2, there exist frequencies where $-\text{Im}\tilde{\Sigma}_0(\omega) < -\text{Im}\tilde{\Sigma}_1(\omega)$. At these frequencies, the approximation $\Sigma_k^{[1]}(\omega)$ will be non-causal at $k = \pi$, because $-\text{Im}\Sigma_{k=\pi}^{[1]}(\omega) = -\text{Im}[\tilde{\Sigma}_0(\omega) - \tilde{\Sigma}_1(\omega)] < 0$. In general, $\Sigma_k^{[1]}(\omega)$ will have non-causal features whenever $|\text{Im}\tilde{\Sigma}_0(\omega)| < |\text{Im}\tilde{\Sigma}_1(\omega)|$, and likewise for $M_k^{[1]}(\omega)$. Less severe truncation by keeping more Fourier coefficients (thus considering longer-ranged terms) gradually reduces non-causal features. We discuss this in more detail below, together with Fig. 4.

As just discussed, non-causal behavior can arise when truncating Fourier series with ω -dependent coefficients. This problem can be avoided by adopting a strategy in which all Fourier series to be truncated involve only ω -independent coefficients. To this end, we consider the CFE representation of $G_k(\omega^+)$, which amounts to a change of variables from ω to n : it encodes the ω dependence explicitly in a continued fraction involving ω -independent CFE coefficients ϵ_{kn} and t_{kn} . Fourier representations of the k dependence of ϵ_{kn} and t_{kn} can then be safely truncated without yielding non-causal behavior.

To illustrate this, we have computed a CFE for $G_{\mathbf{k}}(\omega^+)$ starting from our TaSK result for the discrete spectral function $A_k^{\text{disc}}(\omega)$, using the strategy discussed after Eq. (46). Figures 3(a) and 3(b) show the resulting Liouillian matrix elements ϵ_{kn} and t_{kn} , respectively, for $n \leq 5$. For fixed n they are smooth functions of k . Their Fourier coefficients,

$$\tilde{\epsilon}_{rn} = \int_{-\pi}^{\pi} \frac{dk}{2\pi} (2 - \delta_{r,0}) \cos(kr) \epsilon_{kn}, \quad (77a)$$

$$\tilde{t}_{rn} = \int_{-\pi}^{\pi} \frac{dk}{2\pi} (2 - \delta_{r,0}) \cos(kr) t_{kn} \quad (77b)$$

turn out to decay quickly with r . This can be seen from Figs. 3(c) and 3(d), showing the Fourier coefficients $\tilde{\epsilon}_{rn}$ and \tilde{t}_{rn} , respectively. We find that $\tilde{\epsilon}_{rn} = 0$ for even r while $\tilde{t}_{rn} = 0$ for odd m (because particle-hole symmetry implies $\epsilon_{k,n} = -\epsilon_{k+\pi,n}$ and $t_{k,n} = t_{k+\pi,n}$). We find that the magnitude of the Fourier coefficients decays monotonically with r , $|\tilde{\epsilon}_{1,n}| > |\tilde{\epsilon}_{3,n}| > \dots$ and $|\tilde{t}_{0,n}| > |\tilde{t}_{2,n}| > \dots$. This suggests that the Fourier series, defined as

$$\epsilon_{kn}^{[R]} = \sum_{r=0}^R \tilde{\epsilon}_{rn} \cos(kr), \quad t_{kn}^{[R]} = \sum_{r=0}^R \tilde{t}_{rn} \cos(kr), \quad (78)$$

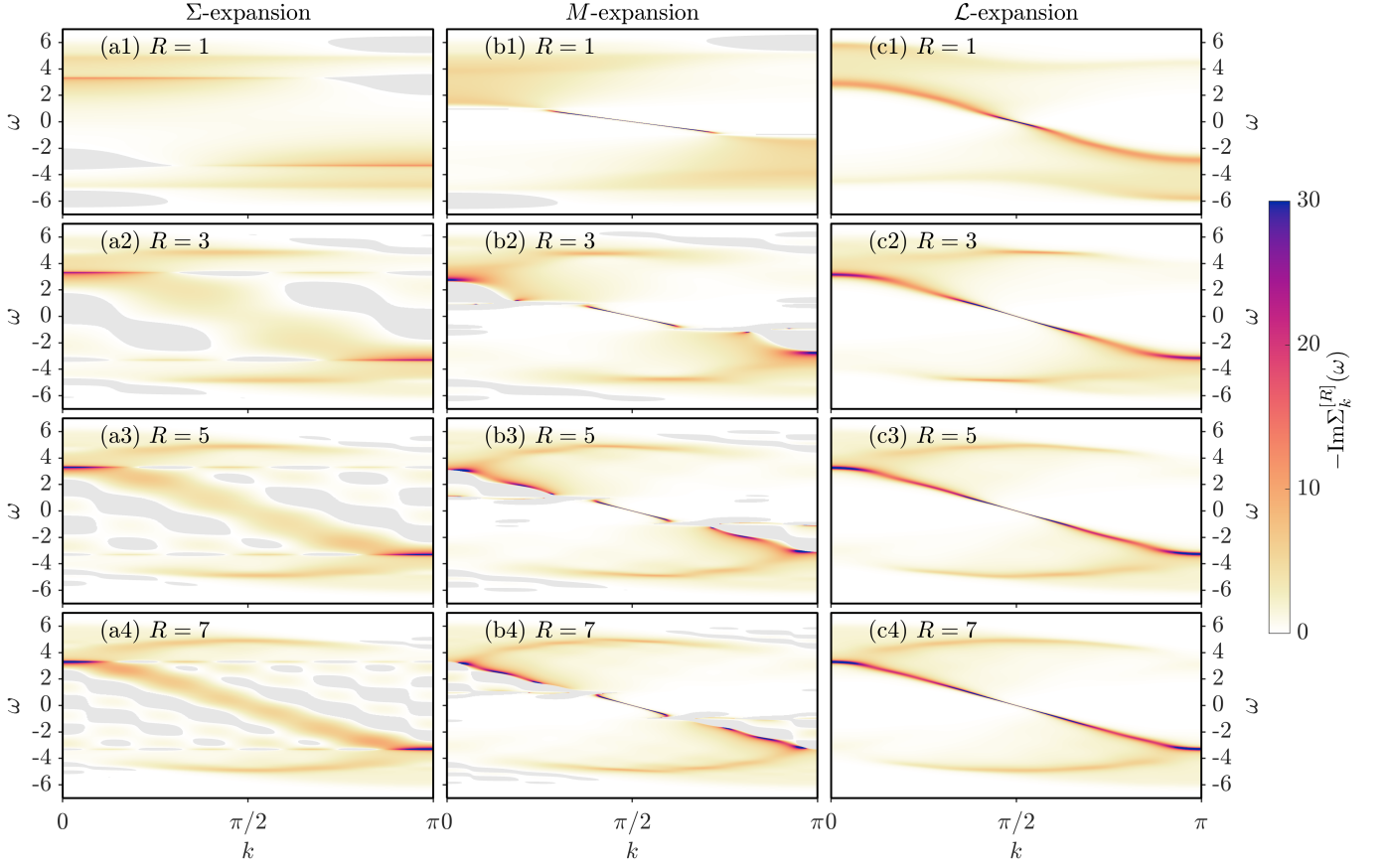


FIG. 4. Self-energy $\Sigma_k^{[R]}(\omega)$ obtained from truncating the Fourier series of Σ -, M - or \mathcal{L} -expansions at $r \leq R$ as described in the text. Regions where $-\text{Im}\Sigma_k^{[R]}(\omega) < 0$ (non-causal behavior) are depicted gray.

converge smoothly, and that truncating them will not cause significant ringing artifacts. Note that even if ringing does occur, the resulting spectral functions and self-energies are still guaranteed to be causal, in stark contrast to the truncated Fourier series of $\Sigma_k(\omega)$ or $M_k(\omega)$. The reason is that *any* approximation of ϵ_{kn} or t_{kn} that leaves ϵ_{kn} real leads to a hermitian \mathcal{L} and therefore to causal spectra.

Our discussion so far suggests that a truncated Fourier expansion of \mathcal{L} has much more favorable convergence properties than a truncated expansion of Σ or M . We verify this explicitly in Fig. 4, where we investigate how $\Sigma_k^{[R]}(\omega)$, obtained via Σ , M or \mathcal{L} expansions involving truncated ($r \leq R$) summations, evolves when the expansion order R is increased.

The first column, Figs. 4(a1-a4), shows the evolution with R of the self-energy $\Sigma_k^{[R]}(\omega)$, represented by the truncated Fourier series Eq. (75a). In Fig. 4(a1) with $R = 1$, only the first two coefficients are retained, i.e. Eq. (76). This corresponds to neglecting any contributions to the self-energy beyond nearest neighbors, similar to 2-site CDMFT/DCA. Clearly, the approximated self-energy in Fig. 4(a1) does not capture the main features of the actual self-energy shown in Fig. 1(b). The disper-

sive Mott pole, the most distinctive feature of the self-energy in Fig. 1(b), is not captured at all by the truncated Fourier expansion of $\Sigma_k(\omega)$. Further, as discussed earlier, the truncated Fourier expansion yields non-causal artifacts (positive imaginary part) due to ringing, shown as gray areas. With increasing expansion order [Fig. 4(a2-a4)], the correct features are better captured, but convergence is very slow in the expansion order. Even for $R = 7$, which corresponds to considering up to 7 nearest-neighbors (as one would do for 8-site CDMFT/DCA), the self-energy is not fully converged and still shows non-causal features due to ringing.

The second column, Fig. 4(b1-b4), shows the evolution with R of the self-energy $\Sigma_k^{[R]}(\omega) = \omega + \mu - [M_k^{[R]}(\omega)]^{-1}$ when $M_k^{[R]}(\omega)$ is represented by the Fourier expansion (75b) truncated at $r \leq R$. In contrast to the truncated Σ expansion, the truncated M expansion captures the dispersive pole of the self-energy already at the lowest order shown, $R = 1$. However, a low-order truncation also leads to significant non-causal ringing artifacts, appearing prominently in the vicinity of the dispersive pole. Further, the shape of the pole dispersion is not very well captured at low orders. Even at the highest order shown, $R = 7$ in Fig. 4(b4), the self-energy is not captured very

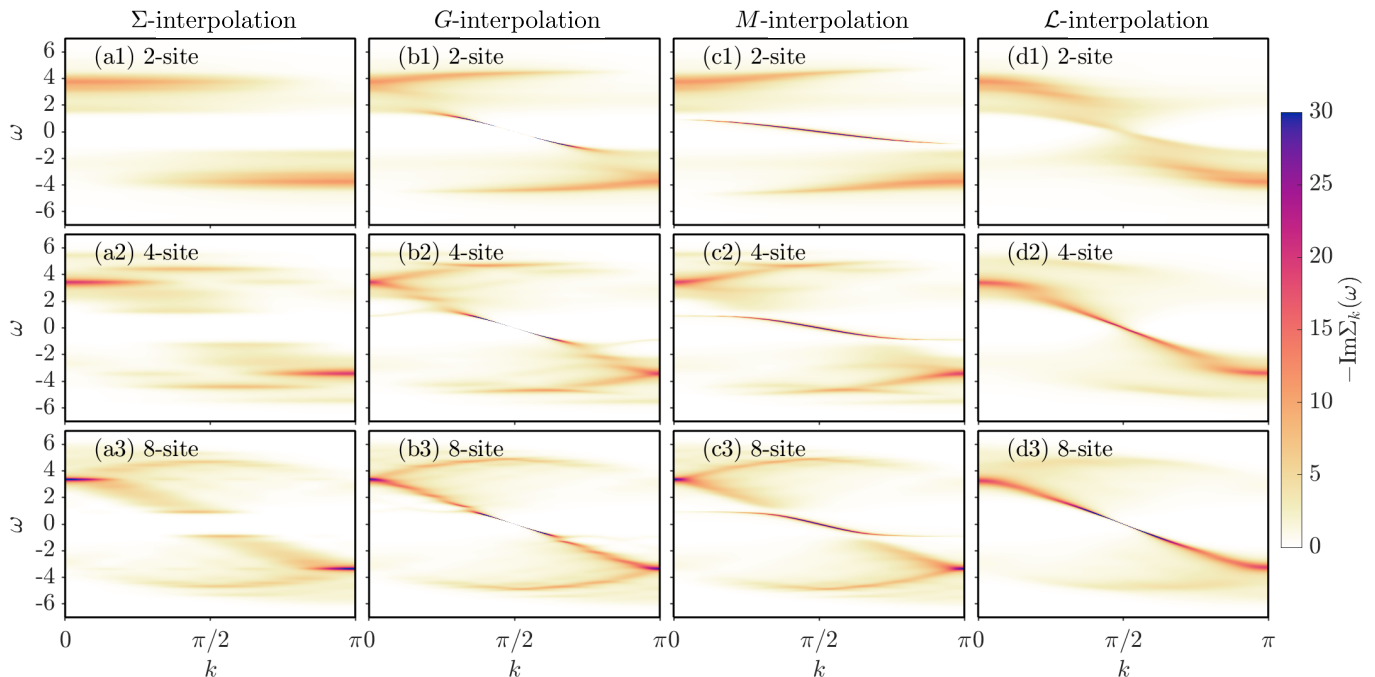


FIG. 5. Interpolated CDMFT self-energies for different cluster sizes N_c , obtained using four different interpolation schemes.

well, and there are still non-causal ringing artifacts left (though to a lesser extent than for the Σ expansion). Overall, truncating the Fourier expansion of M leads to somewhat better results than truncating that of Σ .

The third column, Fig. 4(c1-c4), shows a self-energy $\Sigma_k^{[R]}(\omega)$ obtained as follows: using $A_k^{\text{disc}}(\omega)$ as input, we performed a finite-depth CFE expansion of $G_k(\omega)$ to obtain the Liouvillian matrix elements ϵ_{kn} and t_{kn} ; these were Fourier transformed via Eq. (77) to obtain $\tilde{\epsilon}_{rn}$ and \tilde{t}_{rn} , from which we constructed R -truncated Fourier expansions $\epsilon_{kn}^{[R]}$ and $t_{kn}^{[R]}$ [Eq. (78)]. We used these to compute $\Sigma_k^{[R]}(\omega)$ via the CFE (41) while using the broadening scheme of Ref. 64, Sec. S-2.2, henceforth to be called “CFE+Gaussian broadening”.

As can be seen from Fig. 4(c1-c4), non-causal features are absent at any truncation order, in stark contrast to the truncated Σ or M expansion. Further, the correct dispersion of the self-energy pole is already captured at the lowest order, $R = 1$, with higher orders revealing more and more details. Qualitative convergence is reached at $R = 3$ (as one would use for 4-site CDMFT/DCA). At order $R = 5$ and beyond, the self-energy appears to be quite well converged, changes beyond this order are only minor.

To summarize, our analysis of numerically (almost) exact MPS data reveals that truncating the Fourier expansion of \mathcal{L} matrix elements leads to faster and more controlled convergence than truncating that of Σ or M . Additionally, truncating the \mathcal{L} expansion leads to causal spectra at all expansion orders, in stark contrast to truncating the Σ or M expansion where non-causal features

appear at low orders. Therefore, we can expect \mathcal{L} -interpolation to outperform Σ or M -interpolation. We explicitly explore this in Sec. IV B.

B. Cellular DMFT

To illustrate how \mathcal{L} -interpolation performs compared to M or Σ interpolation when applied to cDMFT data, we perform CDMFT calculations for the 1d Hubbard model analyzed in the previous section. The cluster impurity model that we solve with CDMFT contains as impurity an open-boundary Hubbard chain of N_c sites (thus N_c is the cell size); its two outermost sites on the left and right hybridize with two self-consistent baths with continuous spectra [2]. We discretize each bath using the “mean method” from Ref. 65 and map the discretized impurity model to a chain geometry, with each bath represented by 64 spinful orbitals. For the chain so obtained we use DMRG to compute the ground state. Then, we combine TaSK with a discrete version [60] of the equations of motion approach of Ref. 66 to compute a *discrete* version of the impurity self-energy, a $N_c \times N_c$ matrix-valued function with elements $[\tilde{\Sigma}_{\text{imp}}^{\text{disc}}(\omega)]_{\ell,\ell'}$, whose ω -dependence is represented by a sum of δ -peaks. (Due to CDMFT self-consistency, this also corresponds to the discrete lattice self-energy, $\tilde{\Sigma}_{\text{lattice}}^{\text{disc}}(\omega)$.) We then use $\tilde{\Sigma}_{\text{imp}}^{\text{disc}}(\omega)$ for two purposes. On the one hand, we use CFE+Gaussian broadening to obtain a smooth version of the impurity self-energy, $\tilde{\Sigma}_{\text{imp}}(\omega)$. We then take the latter as input for traditional Σ -, G -, M -interpolation employing super-

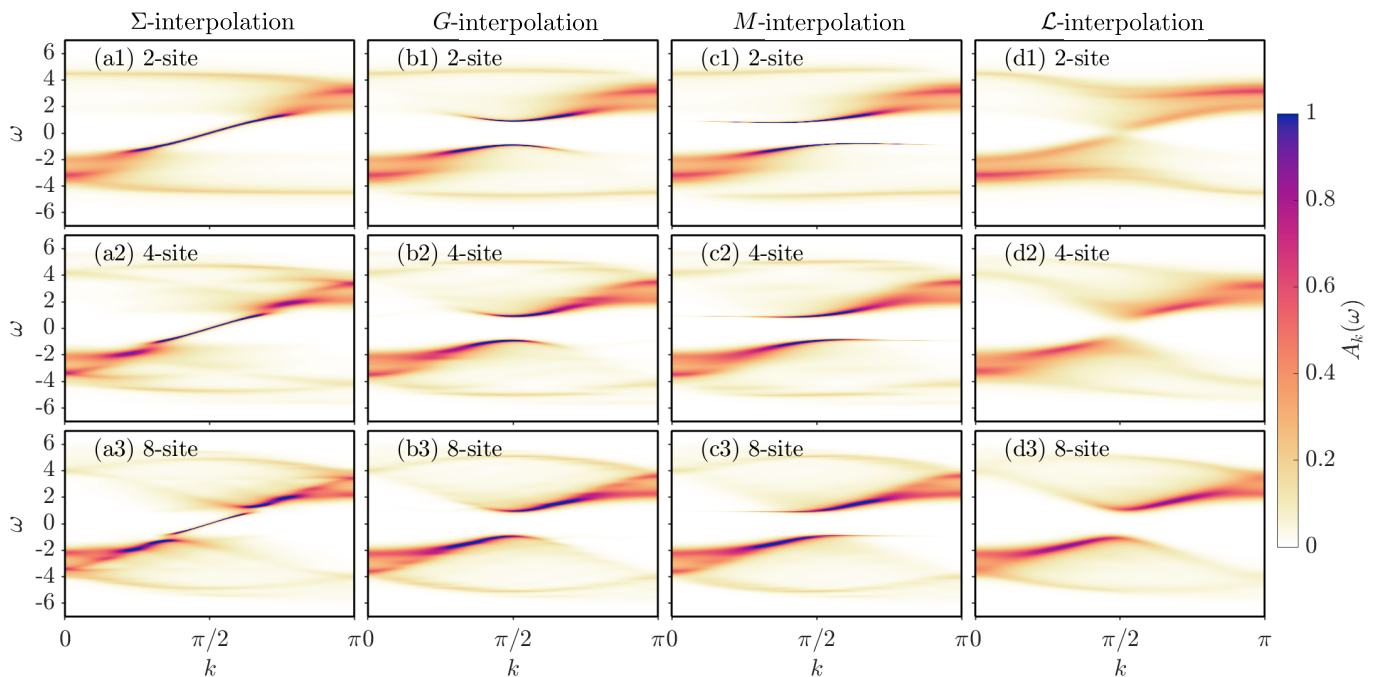


FIG. 6. Spectral function from different interpolation schemes for different cluster sizes.

lattice averaging [Eqs. (55), (56)], using for $\tilde{\mathbf{Q}}(\omega)$ either the broadened $\tilde{\Sigma}(\omega)$, or corresponding functions $\tilde{\mathbf{G}}(\omega)$ or $\tilde{\mathbf{M}}(\omega)$ obtained from the former in standard manner (Eqs. (7) and (6) of Ref. 33). On the other hand, for \mathcal{L} -interpolation, we compute the CFE of the discrete $\tilde{\Sigma}_{\text{imp}}^{\text{disc}}(\omega)$ to obtain the single-particle irreducible Liouvillian matrix elements $\tilde{\epsilon}_n$ and $\tilde{\mathbf{t}}_n$. Next, we \mathcal{L} -interpolate them, using the superlattice average (66) to obtain $\bar{\epsilon}_{rn}$, $\bar{\mathbf{t}}_{rn}$, and Eq. (67) to obtain ϵ_{kn} and \mathbf{t}_{kn} . We use these in Eq. (69) to construct an \mathcal{L} -interpolated self-energy $\Sigma_k(\omega)$ while using CFE+Gaussian broadening (see App. H for details). This, finally, is the estimate produced by \mathcal{L} -interpolated CDMFT for the lattice self-energy, to be compared to the self-energy computed in Sec. IV A.

In the following, we compare lattice self-energies (Fig. 5), spectral functions (Fig. 7) and cumulants (Fig. 7), for three different cluster sizes, $N_c \in \{2, 4, 8\}$, in each case obtained in four different ways, via Σ , G , M and \mathcal{L} -interpolation. The self-energies are shown in Fig. 5(a1-a3). Even at the largest cluster size, the Σ -interpolation fails to reproduce the dispersive pole of the self-energy, i.e. it fails to correctly capture the Mott physics in this model. This behavior is in line with the analysis of the truncated Fourier series in Fig. 4, where we have seen that a large number of Fourier coefficients are required to capture the dispersive pole. Σ -interpolation is based on the assumption that the self-energy is weakly k -dependent, and for the 1d Hubbard model, this is simply not the case.

Figures 5(b1-b3) and (c1-c3) show the self-energy resulting from G - and M -interpolation, respectively. Both interpolation schemes work very well in producing the

dispersive Mott pole, even for the small 2-site cluster. However, for the larger clusters (4-site and 8-site), stripy structures show up which are artifacts of the interpolation. These stripy structures are more pronounced for G -interpolation than for M -interpolation. For the 2-site cluster, G -interpolation seems to perform better than M -interpolation in reproducing the features of the self-energy, in particular the slope of the dispersive pole. The reason for that exceptional performance of the G and M schemes at small N_c is the very weak k -dependence of the cumulant in this model. However, if the cumulant would be strongly k -dependent (for instance, if it had a dispersive pole), then G and M -interpolation are expected to encounter issues similar to Σ -interpolation in the present case. The 1d Mott insulator is therefore a case where the G and M -interpolation performs very well, but there is no guarantee that this is generically the case.

Figures 5(d1-d3) show the self-energy resulting from \mathcal{L} -interpolation. The dispersive pole of the self-energy, which is one of its main features, is captured for all cluster sizes. However, the pole strength is not correctly captured for the small clusters, which results in an incorrect size of the Mott gap. The information on the correct self-energy pole weight therefore seems to reside in longer-ranged matrix elements of \mathcal{L} , a conclusion which can also be drawn from Fig. 4.

Figures 6 and 7 show the spectral functions and cumulants corresponding to the self-energies in Fig. 5. The Σ -interpolated spectral functions and cumulants display a dispersive pole even for the largest cluster size, a result that is evidently incorrect. The G and M schemes both produce the correct Mott gap in G and M , even for the

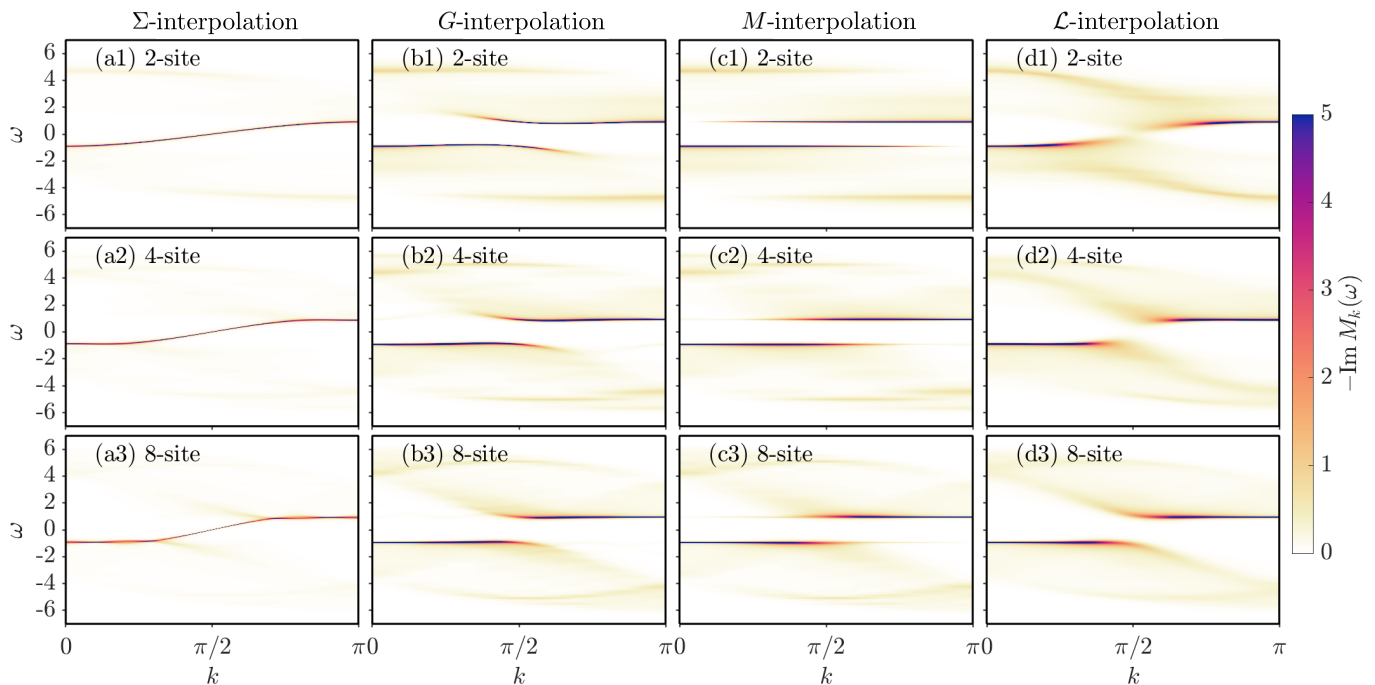


FIG. 7. Cumulant from different interpolation schemes for different cluster sizes.

smallest cluster size. Further, when using these interpolation schemes, the qualitative features of G and M compare quite well with the DMRG result for the 1d Mott insulator. \mathcal{L} -interpolation, on the other hand, has trouble reproducing the correct size of the Mott gap at small cluster sizes, which is due to the incorrect weight of the self-energy pole. For the largest $N_c = 8$ cluster, however, \mathcal{L} -interpolation reproduces the correct Mott gap and the qualitative features of both M and G compare very well with the DMRG result. For $N_c = 8$, \mathcal{L} interpolation further provides smoother spectral features than the G or M schemes, with fewer interpolation artifacts.

To summarize, the Fourier series of matrix elements ϵ_{kn} and \mathbf{t}_{kn} , of a numerically (almost) exact model, decay more rapidly than the Σ and M expansion of the same data. The conservation of causality of the \mathcal{L} -interpolation becomes also evident within these examples. Our \mathcal{L} -interpolation yields a fully causal interpolation that converges faster with cDMFT cluster size, which is confirmed by a benchmark test of the 1d Hubbard model using CDMFT+TaSK with several cluster sizes N_c .

V. DCA OF THE 2D HUBBARD MODEL

This section deals focuses on the interpolation of DCA results (i.e. in this section, “interpolation” means \mathbf{k} -space interpolation). We obtain the input data for our interpolations from a 4-patch DCA+NRG treatment of the two-dimensional Hubbard model for three choices of doping, corresponding to Fermi-liquid, pseudo-gap and Mott insulator regimes. A thorough analysis of our DCA+NRG

results for this model will be published separately [67]. Here, we focus on interpolation rather than physical implications. We compare the non-interpolated discontinuous DCA results to smooth interpolated versions obtained from M -, Σ - and \mathcal{L} -interpolations, focusing on data sets for which different interpolation schemes turn out to yield strikingly different results. Our analysis contains a striking physical result: \mathcal{L} -interpolation can (depending on doping) resolve Fermi and Luttinger arcs which together form a closed surface, with a smooth crossover between Fermi and Luttinger arcs.

A. Model and periodization

We study the two-dimensional Hubbard model,

$$H = -\sum_{\mathbf{r}\mathbf{r}'\sigma} t_{\mathbf{r}\mathbf{r}'} c_{\mathbf{r}\sigma}^\dagger c_{\mathbf{r}'\sigma} - \mu \sum_{\mathbf{r}\sigma} n_{\mathbf{r}\sigma} + U \sum_{\mathbf{r}} n_{\mathbf{r}\uparrow} n_{\mathbf{r}\downarrow}, \quad (79)$$

where $t_{\mathbf{r}\mathbf{r}'}$ contains nearest- and next-nearest-neighbor hopping t and t' , respectively. The terms in the Hamiltonian are illustrated in Fig. 8(a). For the results presented below, we use $t = 1$ as our energy unit, set $t' = -0.3t$, $U = 7t$, use temperature $T = 10^{-10}t$, and adjust μ to vary the doping δ , which is our tuning parameter.

We obtain approximate solutions using 4-patch DCA, using the “star patching” scheme of Ref. 68, as illustrated in Fig. 8(b). To solve the cluster impurity model, we use the MuNRG implementation [69, 70] of the numerical renormalization group (NRG) [66, 71–74], which is based on the QSpace tensor library [75–79]. We exploit U(1) charge and SU(2) spin rotation symmetry, use a

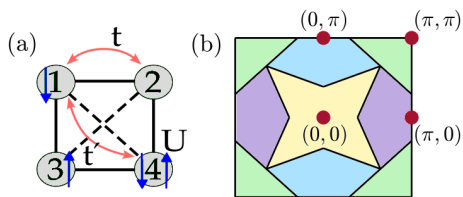


FIG. 8. (a) Illustration of hopping and interaction terms in the 2d Hubbard model. (b) Star patching geometry with patch momenta $\mathbf{K} \in \{(0,0), (0,\pi), (\pi,0), (\pi,\pi)\}$.

discretization parameter of $\Lambda_{\text{NRG}} = 8$, no z -shifting, and keep up to $N_{\text{keep}} = 10^5$ $U(1) \times \text{SU}(2)$ multiplets. Further, we use an interleaved Wilson chain geometry [80, 81], fully interleaving the bath modes associated with the different patches (labeled by their patch momenta) in the following order: $\mathbf{K}_1 = (0,0)$, $\mathbf{K}_2 = (\pi,0)$, $\mathbf{K}_3 = (0,\pi)$, $\mathbf{K}_4 = (\pi,\pi)$. We broaden discrete NRG data using a log-Gaussian broadening scheme [69] with broadening parameter $\sigma = 0.7$ there, and use Kugler’s symmetric estimator approach [66] to compute the self-energies $\Sigma_{\mathbf{K}}(\omega)$.

Although interleaving breaks the expected symmetry between the $(\pi,0)$ and $(0,\pi)$ patches, the resulting broadened self-energy functions $\Sigma_{(\pi,0)}(\omega)$ and $\Sigma_{(0,\pi)}(\omega)$ are essentially identical, differing by less than 10^{-3} . Therefore, we enforced the symmetry between them in the DMFT loop, setting $\Sigma_{(0,\pi)}(\omega) \leftarrow \Sigma_{(\pi,0)}(\omega)$ before proceeding to the next DMFT iteration.

To extract the Liouvillian matrix elements $\epsilon_{\mathbf{K}n}$ and $t_{\mathbf{K}n}$ associated with each patch, we use the log-CFE described in Sec. IIH. We set $\Lambda = 1.2$ and $\tau = 5$ for the splitting function $w_n^S(\omega)$, see Eq. (52). Further, we set $\Omega_{\text{min}} = 10^{-9}$ (smaller values of Ω_{min} lead to low-frequency inaccuracies due to double precision), and choose Ω_{max} such that $\mathbf{A}_{\text{disc}}(\omega)$, the discrete spectral function output of our NRG impurity solver, satisfies its spectral sum rule to within 10^{-5} , i.e. $\mathbf{1} - \sum_{|\omega_i| < \Omega_{\text{max}}} \mathbf{A}_{\text{disc}}(\omega_i) < \mathbf{1} \cdot 10^{-5}$. This ensures that we capture essentially the entire support of the spectral function $\mathbf{A}(\omega)$; note that this choice amounts to cutting off over-broadened self-energy tails. For numerical details, and a discussion on how the interpolated results depend on τ and Λ , see App. E3.

Figure 9 shows exemplary DCA patch self-energies (dashed lines) and their CFE representations (solid lines), confirming that our log-CFE accurately represents the cluster self-energies. Figures 10(a,b) show the corresponding Liouvillian matrix elements $\epsilon_{\mathbf{K}n}$ and $t_{\mathbf{K}n}$, demonstrating that they decrease exponentially with n . Figure 10(c) shows the imaginary part of the fast modes, $R_{\mathbf{K}n}^{\text{F}''}(\omega) = -\frac{1}{\pi} \text{Im} R_{\mathbf{K}n}^{\text{F}}(\omega)$, for several choices of n , with individual patch momenta distinguished by line color. The lines for the different patches show some slight differences for $n = 1$ but overlap increasingly well with decreasing n . This implies that the \mathbf{K} -dependence of $R_{\mathbf{K}n}^{\text{F}''}(\omega)$ is weak and becomes ever weaker with increasing n . This property, which appears to arise generically for log-CFEs, is important for reducing the likelihood of

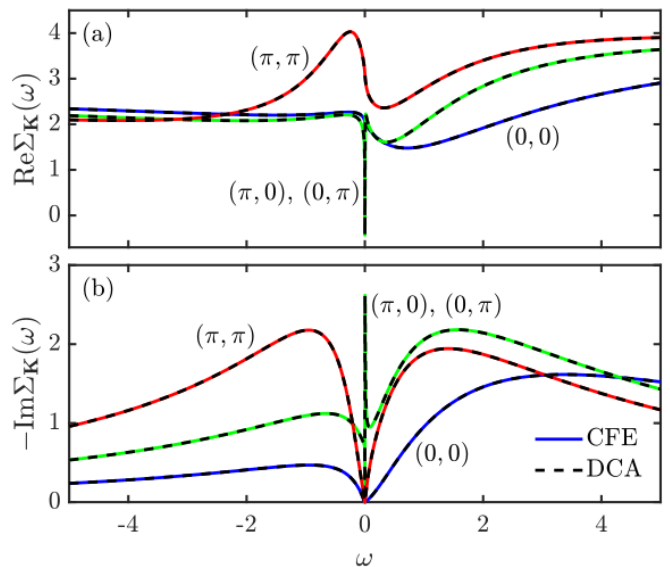


FIG. 9. (a) Real and (b) imaginary parts of the original DCA patch self-energy $\Sigma_{\mathbf{K}}(\omega)$ (dashed lines) and its log-CFE representation (51) (colored lines), for the patch momenta $\mathbf{K}_1 = (0,0)$ (blue), $\mathbf{K}_2 = (\pi,0)$ and $\mathbf{K}_3 = (0,\pi)$ (green), and $\mathbf{K}_4 = (\pi,\pi)$ (red). The excellent agreement between colored and dashed curves demonstrates that the log-CFE accurately represents the DCA results.

causality problems to arise when interpolating fast-mode functions, as will be elaborated below.

Our choice of $\tau = 5$ results in a rather sharp split between fast and slow modes. The dependence on τ is discussed in detail in App. E3. The fact that $|\epsilon_{\mathbf{K}n}|$ shows a very much stronger patch dependence than $R_{\mathbf{K}n}^{\text{F}''}(\omega)$ means that most of the \mathbf{k} -dependence of the interpolation will enter through the Liouvillian matrix elements.

Having obtained the Liouvillian matrix elements, our next step is to interpolate them using canonical DCA interpolation, as described in Sec. III B. For the star patching illustrated in Fig. 8, the $N_p = 4$ patches are invariant under x - and y -reflections, but not under $\pi/2$ rotations about the origin. The lowest few lattice harmonics that are invariant under these symmetry operations are constructed explicitly in App. F. They have the form

$$\begin{aligned} \phi_{\mathbf{k},1} &= 1, & \phi_{\mathbf{k},3} &= \cos k_x - \cos k_y, \\ \phi_{\mathbf{k},2} &= \cos k_x + \cos k_y, & \phi_{\mathbf{k},4} &= \cos k_x \cos k_y. \end{aligned} \quad (80)$$

leading to

$$\Psi_{j,\mathbf{K}} \simeq \begin{pmatrix} 0.2500 & 0.2500 & 0.2500 & 0.2500 \\ 0.4010 & 0.0092 & 0.0092 & -0.4194 \\ 0.0000 & 0.4050 & -0.4050 & 0.0000 \\ 0.7591 & -0.6645 & -0.6645 & 0.5698 \end{pmatrix} \quad (81)$$

for the coefficients appearing in Eq. (59) for the canonical DCA interpolation functions $\alpha_{\mathbf{k},\mathbf{K}}$. The latter are then used to interpolate $\epsilon_{\mathbf{K}n}$, $t_{\mathbf{K}n}$, and $R_{\mathbf{K}n}^{\text{F}}(z)$ via Eq. (58).

The interpolation functions $\alpha_{\mathbf{k},\mathbf{K}}$ are depicted in the first row of Fig. 11. They exhibit large positive weights in

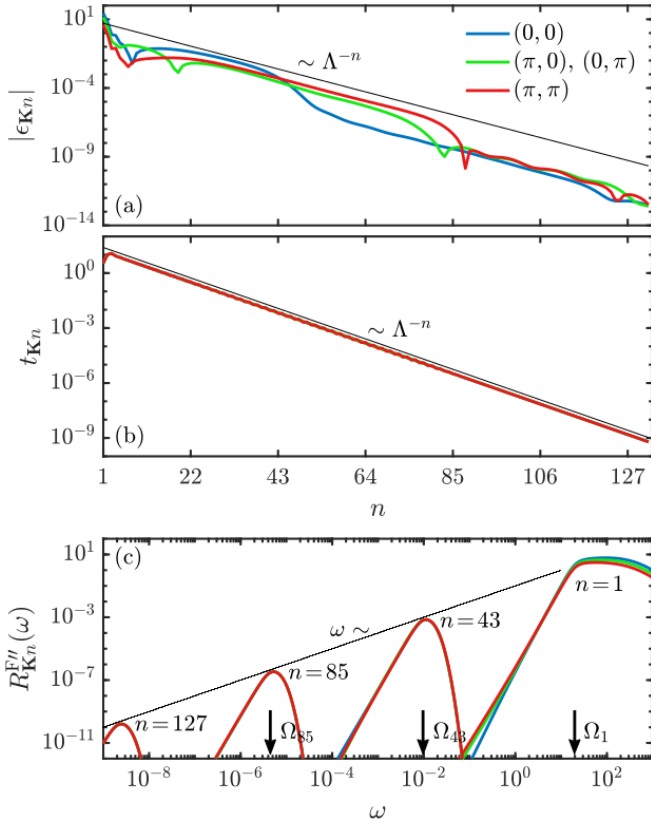


FIG. 10. (a,b) The Liouvillian matrix elements $|\epsilon_{\mathbf{K}_n}|$ and $t_{\mathbf{K}_n}$ obtained from a log-CFE with $\Lambda = 1.2$ and $\tau = 5$. (c) The spectral part of four fast modes $R_{\mathbf{K}_n}^{F''}(\omega)$ with $n \in \{1, 43, 85, 127\}$; arrows indicate the corresponding energy scales Ω_n (cf. Eq. (52)). Thin black lines indicate the scaling behavior. As in Fig. 9, colors distinguish patch momenta.

the centers of their respective patches and fall off towards the other patches. Importantly, to fulfill the patch average condition (60), they become negative in the centers of some other patches. As an aside, we note that this can cause $\mathbf{Q}_{\mathbf{k}}(\omega) = \sum_{\mathbf{K}} \alpha_{\mathbf{k},\mathbf{K}} \mathbf{Q}_{\mathbf{K}}(\omega)$ to be negative for some combinations of \mathbf{k} and ω even if all $\mathbf{Q}_{\mathbf{K}}(\omega)$ are strictly positive functions of ω . This may lead to causality violations in some situations, e.g. when used for Σ - or M -interpolation. In sections VB and VC below, where we compare \mathcal{L} -, Σ - and M -interpolation, we sidestep the potential causality issues of Σ - and M -interpolation by implementing the latter two schemes using the modified interpolation functions $\alpha_{\mathbf{k},\mathbf{K}}^{\text{mod}}$ of Eq. (65) (instead of $\alpha_{\mathbf{k},\mathbf{K}}$). There, the non-local Fourier modes $\phi_{\mathbf{k},j>1}$ are rescaled by a factor $1/N_j$ (defined in App. F), which counteracts their causality-violating tendencies. The resulting functions $\alpha_{\mathbf{k},\mathbf{K}}^{\text{mod}}$ are shown in the second row of Fig. 11. They are positive everywhere, as desired; however, they also exhibit a much weaker momentum dependence compared to $\alpha_{\mathbf{k},\mathbf{K}}$, and they do not preserve the patch average since Eq. (60) is not fulfilled. (We have also explored using other interpolation function for Σ - and M -interpolation, e.g. ones satisfying $\alpha_{\mathbf{K},\mathbf{K}} = 1$, so that setting $\mathbf{k} = \mathbf{K}$

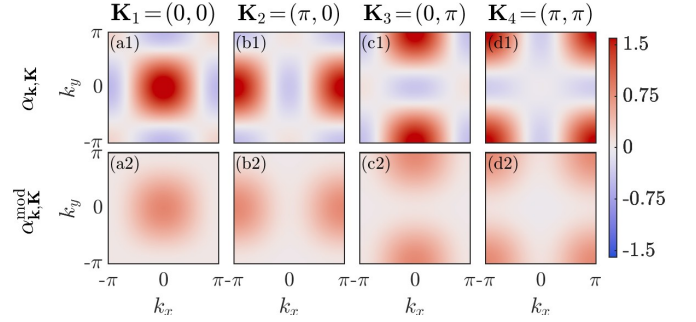


FIG. 11. (a1-d1) The canonical DCA interpolation functions $\alpha_{\mathbf{k},\mathbf{K}}$ of Eq. (59), and (a2-d2) the modified interpolation functions $\alpha_{\mathbf{k},\mathbf{K}}^{\text{mod}}$ of Eq. (65), for the star patching geometry of Fig. 8(b). All plots employ the same diverging color scale. The $\alpha_{\mathbf{k},\mathbf{K}}^{\text{mod}}$ functions are strictly positive due to the reduced non-local contributions.

in the interpolated $Q_{\mathbf{k}}(z)$ reproduces the original patch function $Q_{\mathbf{K}}(z)$. These yielded minor quantitative but no qualitative differences from the results shown below, obtained using $\alpha_{\mathbf{k},\mathbf{K}}^{\text{mod}}$.)

Returning to \mathcal{L} -interpolation, we reiterate that we used the canonical DCA interpolation functions $\alpha_{\mathbf{k},\mathbf{K}}$ not only for obtaining $\epsilon_{\mathbf{k}n}$ and $t_{\mathbf{k}n}$, but also for $R_{\mathbf{k}n}^F(z)$. This did not lead to any causality problems, since the \mathbf{K} -dependence of the $R_{\mathbf{k}n}^F(z)$ functions obtained from our log-CFE is so weak (cf. Fig. 10(c)).

B. Interpolated Spectra

In this section, we compare results for spectral functions $A_{\mathbf{k}}(\omega)$ and imaginary parts of the self-energy $\Sigma_{\mathbf{k}}(\omega)$ obtained from different interpolation schemes. We consider results at three values of doping, corresponding to a Fermi liquid (FL) at doping $\delta = 0.25$, the pseudogap phase (PG) at $\delta = 0.21$, and a Mott insulator (MI) at $\delta = 0.00$. We plot both $\Sigma_{\mathbf{k}}(\omega)$ and $A_{\mathbf{k}}(\omega)$ along the path $\Gamma = (0, 0) \rightarrow X = (0, \pi) \rightarrow M = (\pi, \pi) \rightarrow \Pi = (\pi/2, \pi/2) \rightarrow \Gamma = (0, 0)$ in the Brillouin zone ($\Gamma X M \Pi \Gamma$), with momentum \mathbf{k} on the abscissa and frequency ω on the ordinate. The corresponding Fermi surfaces (FS) are presented in the next section.

The spectral functions $A_{\mathbf{k}}(\omega)$ are presented in Fig. 12, where we compare the non-interpolated “raw” DCA data in column (a) with that obtained after Σ , M and \mathcal{L} -interpolation in columns (b), (c) and (d), respectively. The rows correspond to the different regimes, with the Fermi liquid ($\delta = 0.25$) in the top row, pseudogap ($\delta = 0.21$) in the middle row, and Mott insulator ($\delta = 0.00$) in the bottom row. We checked that the filling is preserved by all three interpolation schemes.

In the Fermi liquid, the self-energy is only weakly \mathbf{K} -dependent. interpolation therefore does not strongly depend on the method, and interpolated results closely match the non-interpolated data.

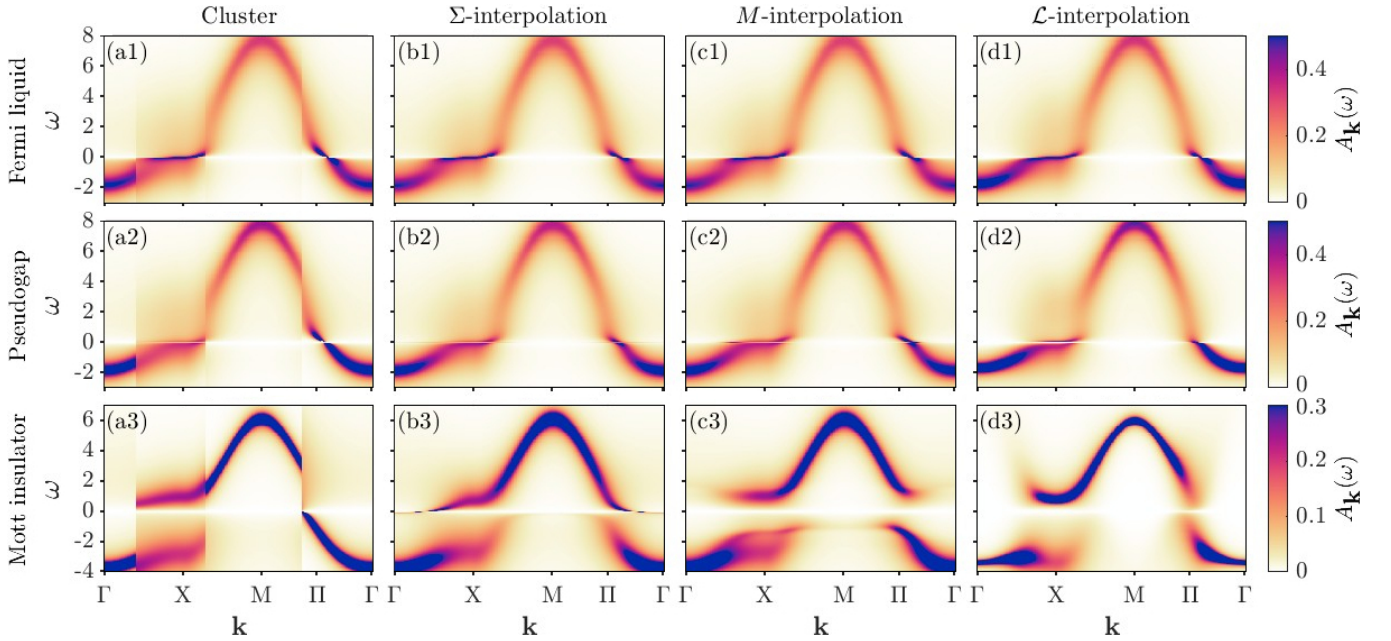


FIG. 12. Spectral function $A_{\mathbf{k}}(\omega)$ of DCA+NRG computations performed using the 4-patch star geometry of Fig. 9, for $t = 1$, $t' = -0.3t$, $T = 10^{-10}t$, and $U = 7t$. $A_{\mathbf{k}}(\omega)$ is plotted as functions of frequency ω and momentum \mathbf{k} along the path $\Gamma = (0, 0) \rightarrow X = (0, \pi) \rightarrow M = (\pi, \pi) \rightarrow \Pi = (\pi/2, \pi/2) \rightarrow \Gamma = (0, 0)$ in the Brillouin zone. For column (a) no interpolation was used, for (b-d) Σ -, M - and \mathcal{L} -interpolation are used, respectively. The first, second and third row depict a Fermi liquid, pseudogap and Mott insulator, respectively, for doping $\delta = 0.25$, $\delta = 0.21$ and $\delta = 0.00$.

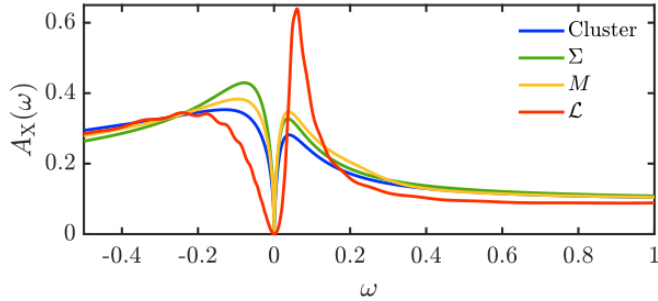


FIG. 13. Spectral function $A_{\mathbf{k}}(\omega)$ at $\mathbf{k} = X$ corresponding to $\delta = 0.21$ emphasizing the gap opening at X for the different interpolation depicted by colors.

In the pseudogap regime, by contrast, the self-energy exhibits strong \mathbf{k} -dependence, and interpolation results depend significantly on the employed method. In this regime, a small gap opens in the vicinity of momentum X which is more pronounced when using \mathcal{L} -interpolation compared to the Σ -, and M -interpolation. To make this more apparent, we show $A_{\mathbf{k}=X}(\omega)$ in Fig. 13. The reason why the Σ - and M -interpolated spectral functions are closer to the non-interpolated one is because the functions $\alpha_{\mathbf{k},\mathbf{K}}^{\text{mod}}$ resemble smeared-out step functions that never become negative. By contrast, the functions $\alpha_{\mathbf{k},\mathbf{K}}$, have a much stronger \mathbf{k} -dependence and do become negative, a property needed to preserve patch averages (cf. property (ii) on p. 11).

We elaborate this in Fig. 13, where we show a slice

of the spectral functions in Fig. 12 at momentum X , $A_X(\omega)$. There, Σ - and M -interpolation yield curves qualitatively similar to the non-interpolated one. The reason is that in the interpolation formula (58), $\mathbf{Q}_{\mathbf{k}}(\omega) = \sum_{\mathbf{K}} \alpha_{\mathbf{k},\mathbf{K}} \mathbf{Q}_{\mathbf{K}}(\omega)$, the ω -dependence on the left is linearly inherited from that on the right. By contrast, the \mathcal{L} -interpolated result differs from that of the other three significantly, because its ω -dependence is inherited non-linearly, via the different levels of the CFE.

Reducing the doping from the pseudogap phase to $\delta = 0.00$ yields the Mott phase. This case is the strong suit of the M -scheme, since the interpolation of the cumulant, which is inversely proportional to the self-energy, facilitates a reliable reconstruction of self-energy poles [38]. Specifically, the M -interpolation yields a clear gap along the path $\Gamma X M \Pi \Gamma$, while the Σ -interpolation struggles to fully extend the gap throughout \mathbf{k} -space, due to band tails reaching into the $\omega \sim 0$ regime. On the other hand, the \mathcal{L} -interpolation, similar to the M -scheme, shows a fully gapped Brillouin zone, with gap sizes comparable to the cluster result.

Note that M -interpolation yields a rather large gap throughout the path $\Gamma X M \Pi \Gamma$. This suggests that it may overestimate the gap at Π . For Σ -interpolation and M -interpolation the distribution of poles in the self-energy within the \mathbf{k} -space depends solely on the interpolation function $\alpha_{\mathbf{k},\mathbf{K}}$. By contrast, the \mathcal{L} -scheme resolves the self-energy poles in terms of multiple Liouvillian matrix elements, allowing the weight to accumulate in a more flexible distribution throughout \mathbf{k} -space—resulting

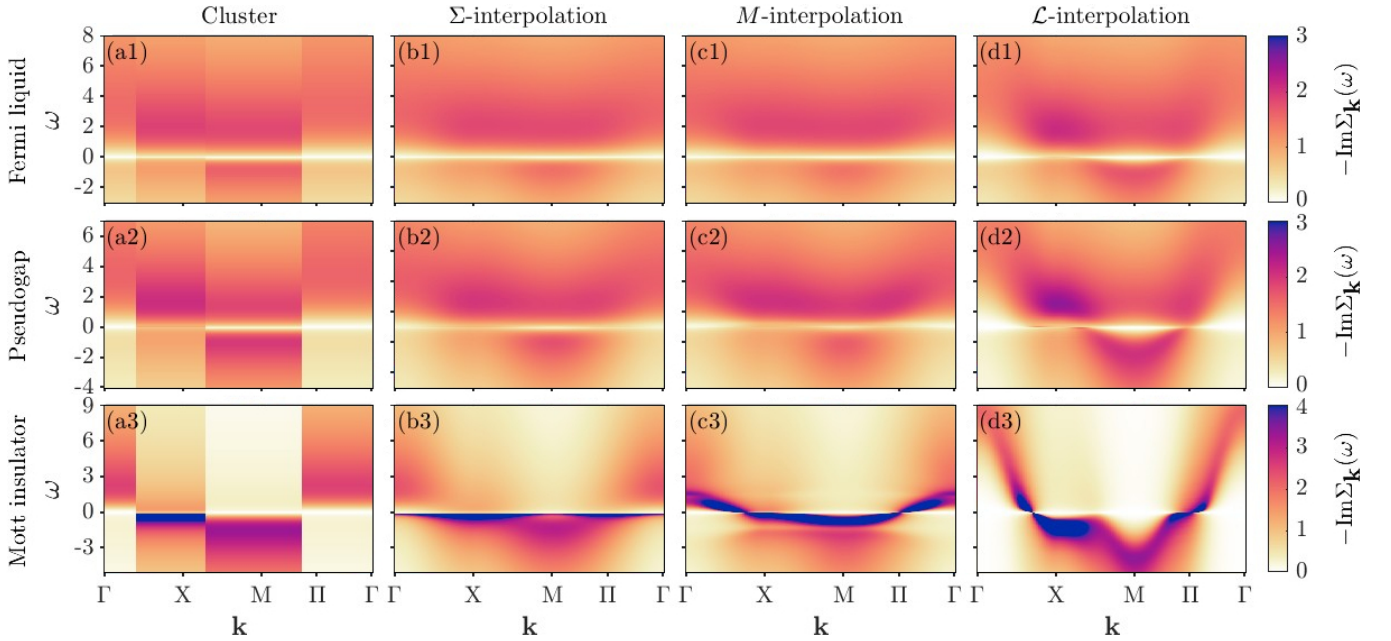


FIG. 14. Same as Fig. 12, but for the imaginary part of the self-energy $-\text{Im}\Sigma_{\mathbf{k}}(\omega)$.

in two differently sized gaps near X and Π .

Figure 14 shows the spectral part of the self-energy, $-\text{Im}\Sigma_{\mathbf{k}}(\omega)$, in the same manner as Fig. 12. All periodizations mimic the non-interpolated case, with the \mathcal{L} -scheme exhibiting a more structured intensity profile.

The Fermi liquid at $\delta = 0.25$ is already close to the pseudogap transition; hence, non-local (i.e. \mathbf{k} -dependent) effects are slightly enhanced compared to a FL at $\delta \gg 0.25$. Due to the faster-converging Fourier coefficients in the \mathcal{L} -scheme, we argue that these non-local contributions are better captured in this scheme—leading to the large self-energy at momentum X, where the pseudogap opens.

In the pseudogap phase, $-\text{Im}\Sigma_{\mathbf{k}}(\omega)$ exhibits a narrow peak near $\omega \sim 0$ in the anti-nodal patches (see Fig. 9). All interpolation schemes are able to resolve this peak. In the Σ - and M -interpolation, however, it is resolved in broad and flat structures around X and along $M\Gamma$ (these are not prominently visible in the second row of Fig. 14, due to the linear ω -scale.) By contrast, the \mathcal{L} -scheme connects these broad and flat structures to high-energy structures, resulting in a more prominently structured profile for $\Sigma_{\mathbf{k}}(\omega)$, i.e. more clearly defined bands. The appearance of such clearly defined bands suggests that \mathcal{L} -interpolation yields a more plausible representation of the pseudogap phase.

For the Mott insulator, Σ -interpolation fails to capture the self-energy divergence across (i.e. on both sides of) $\omega = 0$, resulting erroneously in some finite spectral weight of $A_{\mathbf{k}}(\omega)$ [Fig. 12(b3)] at $\omega = 0$ throughout the path $\Gamma X M \Pi \Gamma$. By contrast, M -interpolation yields a narrow self-energy band that lies close to $\omega = 0$ and crosses $\omega = 0$ two times, visible in Fig. 14(c3). This explains the large gaps in the corresponding spectral function of

Fig. 12(c3). \mathcal{L} -interpolation yields a similar self-energy band, however, it is much more dispersive [Fig. 12(d3)] due to the non-linear ω -dependence of the CFE. As mentioned above, this causes the weight of the self-energy around $\omega = 0$ to have a much stronger momentum dependence along $\Gamma X M \Pi \Gamma$, which yields a correspondingly strong variation for the gap size of the spectral function [Fig. 12(d3)]. This further demonstrates the advantage of its flexible weight distribution among multiple Liouvillian matrix elements.

We conclude this discussion with some remarks regarding the band-width of the self-energy pole. In a 2-dimensional Mott insulator, a dispersive self-energy pole, with a dispersion roughly proportional to $-\epsilon_{\mathbf{k}}$, is expected on general grounds [82]. Qualitatively, this hallmark feature is captured by both M and \mathcal{L} -interpolation, albeit with very different bandwidths. At intermediate coupling, as studied here ($U = 7t$), the bandwidth of the self-energy pole is usually somewhat larger than the electronic bandwidth, see for instance Fig. 5 of Ref. [83] ($U = 4t$) or Fig. 3 of Ref. [64] ($U = 7.5t$). Our electronic bandwidth is $8t$, and we find a self-energy pole bandwidth of $\simeq 11t$ with \mathcal{L} -interpolation, but only $\simeq 2t$ with M -interpolation. Thus \mathcal{L} -interpolation yields a self-energy pole bandwidth consistent with expectations, whereas M -interpolation severely underestimates it.

C. interpolation results at $\omega = 0$

An examination of the Fermi surface (FS) provides additional insight into the performance of the \mathcal{L} -scheme compared to other interpolation methods. Fig. 15

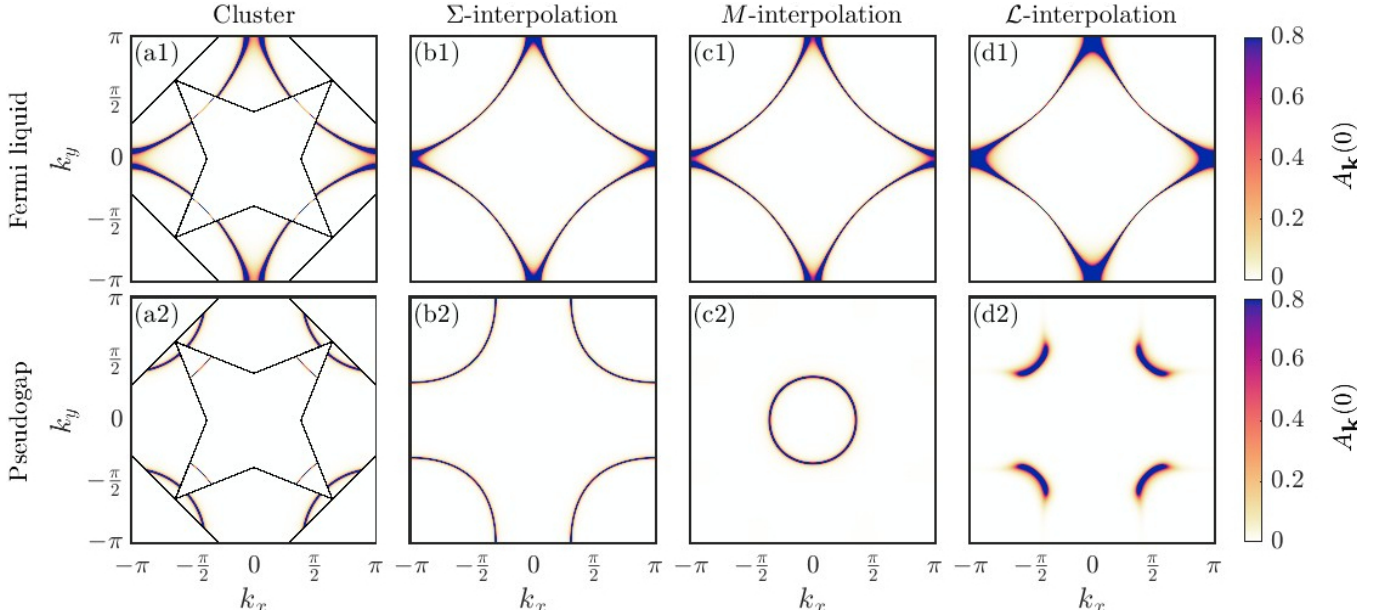


FIG. 15. Spectral function at zero frequency, $A_{\mathbf{k}}(0)$, for the same settings as in Fig. 12. Column (a): (non-periodized) cluster results, featuring discontinuities at the patch borders (straight black lines). Columns (b-d): results from Σ -, M -, and \mathcal{L} -interpolation. Rows 1 and 2 show results for doping $\delta = 0.25$ and $\delta = 0.21$, yielding a Fermi liquid and pseudogap, respectively.

presents a comparison of the Fermi surfaces via plots of the spectral function at zero frequency, $A_{\mathbf{k}}(0)$ for both the Fermi liquid and pseudogap phases. (The Mott insulator is not shown, as $A_{\mathbf{k}}(0) < 10^{-5}$, except for Σ -interpolation, which erroneously does not show a true Mott insulator.) Panels (a1–d1) display the FS of the Fermi liquid, while panels (a2–d2) show the FS in the pseudogap phase. In column (a), the straight black lines indicate the DCA patch boundaries.

The FS for the Fermi liquid is essentially identical across all scheme and mimics the non-interpolated result well. However, the \mathcal{L} -scheme has enhanced intensity at the anti-nodal points. Apparently, any interpolation works well for a simple Fermi liquid.

In the pseudogap phase, the cluster result [Fig. 15(a2)] features hole-like arcs cut off by the patch boundaries, without extending to the Brillouin zone (BZ) edge, leading to gaps around the four “antinodal” points $(\pm\pi, 0)$ and $(0, \pm\pi)$. This is because the $\mathbf{K} = (\pi, \pi)$ cluster patch carries no spectral weight. The traditional Σ - and M -schemes are unable to reproduce key aspects of the cluster result: the Σ -interpolated FS is hole-like but extends all the way to the opposite BZ edges without showing gaps near the edges, while the M -interpolated FS is electron-like.

The \mathcal{L} -scheme is the only interpolation that qualitatively captures all aspects of the cluster computation in the pseudogap phase. First, it preserves the hole-like characteristics; second it also accumulates spectral weight around the four “nodal” points at $(\pm\pi/2, \pm\pi/2)$ and $(\pm\pi/2, \mp\pi/2)$, similar to the cluster result but distributed more smoothly in the shape of Fermi arcs. These

are similar to those observed in photoemission spectra measured by ARPES experiments [37]. Third, \mathcal{L} -interpolation captures the spectral weight distribution along the Fermi surface far better than the other schemes, as discussed in more detail below (see Fig. 18).

At first glance, the Fermi-arc structures seem to imply a non-closed FS. However, additional details become apparent when using a logarithmic color scale, as done in the first row of Fig. 16: The M -scheme yields a slightly enhanced intensity near the BZ edge, in the regions where the Σ -scheme FS is located. The hole-like FS of the \mathcal{L} -scheme actually does close across the BZ edges, albeit with very small spectral weight there, while an electron-like ring with even less weight is also present. On a logarithmic color scale the \mathcal{L} -scheme thus displays structural features from both the Σ - and M -schemes.

The second row of Fig. 16 shows the imaginary part of the self-energy at zero frequency, $-\text{Im}\Sigma_{\mathbf{k}}(0)$, corresponding to the FS data in the first row. The Σ -interpolation closely resembles the nearly constant self-energy of the non-interpolated DCA calculation, showing no enhanced structures. The M -scheme produces Σ -pole rings around the nodal points; these are strongly modified in the \mathcal{L} -interpolation. The \mathcal{L} -scheme displays sharp pocket structures around X that suppress the FS near the BZ boundary. These pockets are connected by a less intense arc close to the FS intensity maximum. Note that for \mathcal{L} -interpolation, the peaks of the self-energy and the Green’s function occur very close to each other.

The last row in Fig. 16 presents the real part of the Green’s function at zero frequency, $\text{Re}G_{\mathbf{k}}(0)$. Here, a sudden blue-to-red change indicates a sign change of

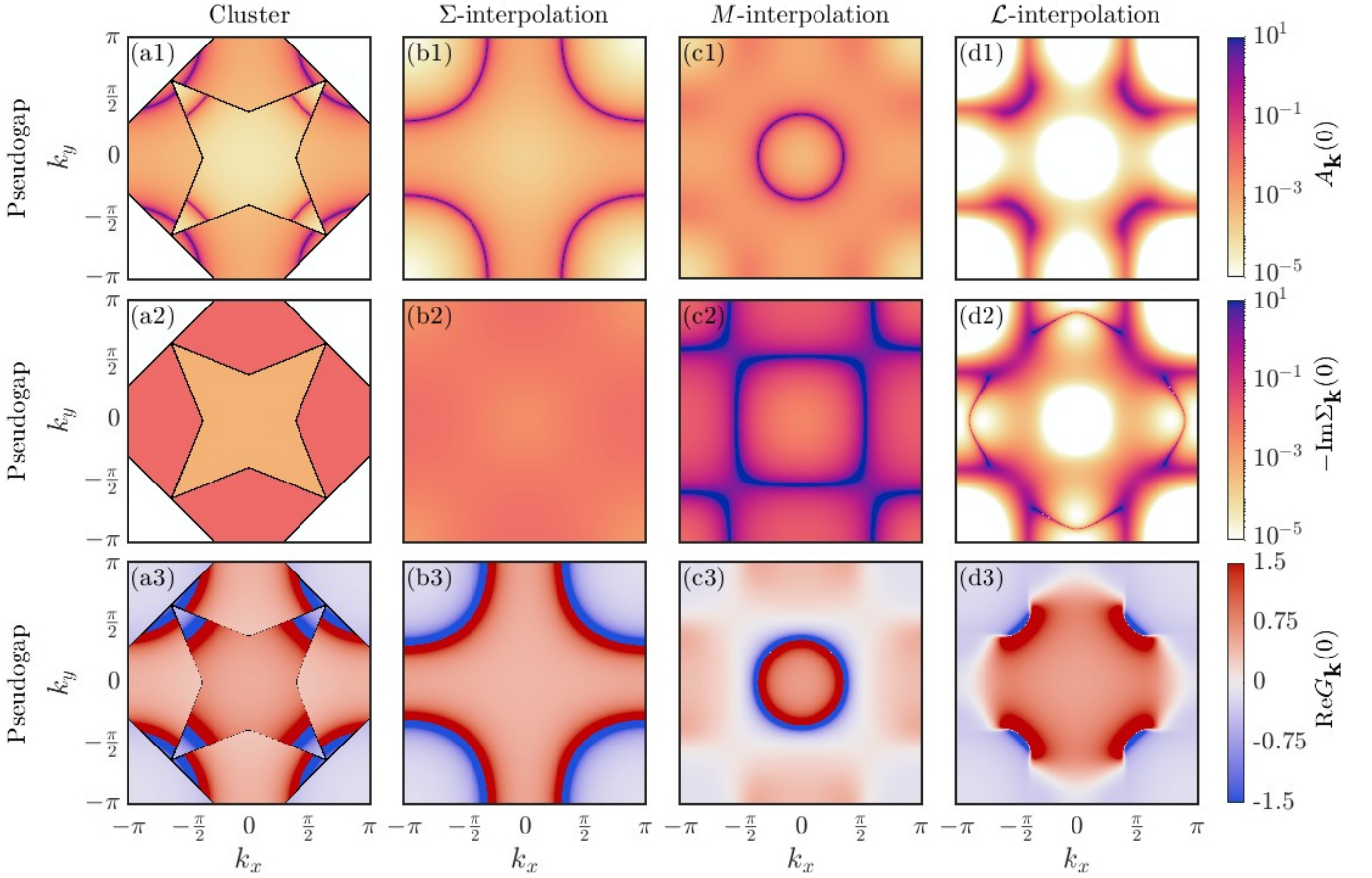


FIG. 16. DCA computation of the pseudogap phase at $\delta = 0.21$. Columns correspond to the same interpolation methods as in Fig. 15. The rows (1-3) depict, respectively, $A_{\mathbf{k}}(\omega = 0)$, $-\text{Im}\Sigma_{\mathbf{k}}(\omega = 0)$ and $\text{Re}G_{\mathbf{k}}(\omega = 0)$. Here row (1) shows the same data as row 2 of Fig. 15 but on a logarithmic color-scale.

$\text{Re}G_{\mathbf{k}}(0)$ via a divergence, i.e. a Fermi surface. By contrast, a gradual blue-to-white-to-red evolution, as seen in parts of panels (c3) and (d3), indicates a smooth evolution through zero, i.e. a Luttinger surface (LS).

The cluster result shows no true LS; instead, it shows small discontinuities at some patch edges. The Σ -scheme interpolates these to yield a hole-like FS. The M -scheme yields a closed, electron-like FS and a closed LS around the anti-nodal points. These are well separated and don't form arcs. The \mathcal{L} -scheme, which most faithfully captures the characteristic structures of the cluster result, yields Fermi and Luttinger arcs. Remarkably, these *smoothly* evolve into each other. We describe this evolution in more detail via the next three figures by showing how three key quantities, $\text{Re}G_{\mathbf{k}}(0)$, $A_{\mathbf{k}}(0)$ and $Z_{\mathbf{k}}$, evolve along the Fermi and Luttinger surfaces.

Figure 17 shows a series of slices of $\text{Re}G_{\mathbf{k}}(0)$, taken for panel (a) from non-interpolated cluster results, and for panel (b) from the corresponding \mathcal{L} -interpolations. Each slice follows a “ \mathbf{k} -ray” (straight-line \mathbf{k} -trajectory through the BZ) emanating from (π, π) at a fixed angle, $0 \leq \theta \leq \frac{\pi}{4}$, as indicated in the top-left insets of Figs. 17(a,b). The curves are plotted vs. $|\mathbf{k} - \mathbf{k}_0|$, where

\mathbf{k}_0 is the momentum where $\text{Re}G_{\mathbf{k}}(0)$ changes sign. For small θ , the non-interpolated curves in (a) change sign at the patch boundaries via small discontinuities. With increasing θ , the sign change shifts to within one of the patches and occurs via a divergence. The pole weight of the divergences is largest at $\theta = \pi/4$, when the \mathbf{k} -ray cuts the nodal point. The \mathcal{L} -scheme interpolates the small patch-boundary discontinuity to a flat zero crossing, i.e. a LS. With increasing θ , the curve crosses zero with increasing slope, *smoothly* evolving into a shape resembling a regularized divergence which is most prominent for $\theta = \pi/4$. The regularization arises through a small (non-divergent) imaginary part of the self-energy.

Figure 18 shows $\max[A_{\mathbf{k}(\theta)}(0)]$, the maximum value assumed by the zero-frequency spectral function along a \mathbf{k} -ray at fixed angle θ , plotted as a function of θ . This quantity corresponds to that measured in ARPES studies aiming to analyse the quasi-particle weight (see, e.g., Fig. 4 of [37]). The cluster result shows a step function profile (blue). The \mathcal{L} -scheme smooths out this step into a broader but still well-defined peak (red) whose flanks smoothly approach zero for $|\theta - \pi/4| \gtrsim \pi/8$. By contrast, the Σ - and M -profiles (green, yellow) show only a very

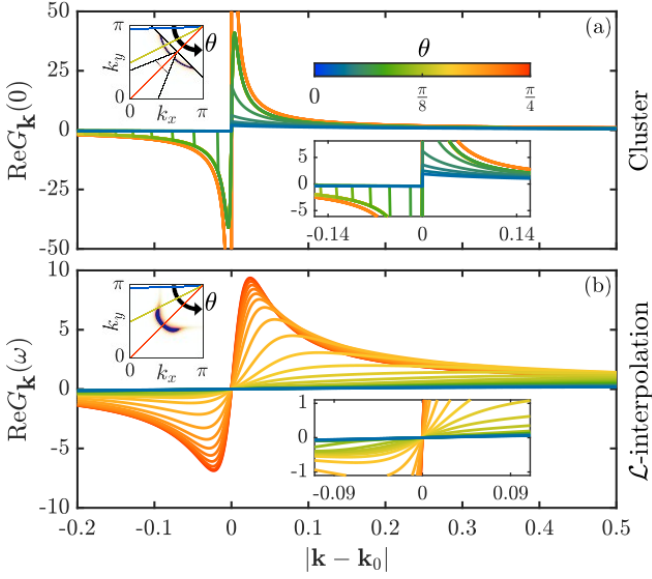


FIG. 17. Real part of the Green's function at zero frequency, $\text{Re}G_{\mathbf{k}}(0)$, computed (a) without interpolation and (b) with \mathcal{L} -interpolation. They are plotted along several \mathbf{k} -rays emanating from (π, π) at angles $0 \leq \theta \leq \frac{\pi}{4}$ (indicated by the color bar and defined in the top-left insets), as functions of $|\mathbf{k} - \mathbf{k}_0|$, where \mathbf{k}_0 is the momentum where $\text{Re}G_{\mathbf{k}}(0)$ changes sign. Bottom-right insets zoom in to small values of $|\mathbf{k} - \mathbf{k}_0|$.

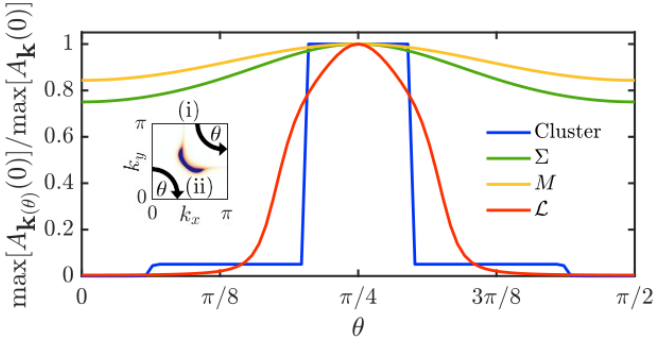


FIG. 18. Maximum of the zero-frequency spectral function along a \mathbf{k} -ray at angle θ , $\max[A_{\mathbf{k}(\theta)}(0)]$, plotted as function of θ and normalized, for ease of comparison, by its peak value at $\theta = \pi/4$. The angle θ , defined in the inset, characterizes \mathbf{k} -rays emanating (i) from (π, π) for Σ -, \mathcal{L} - and no interpolation, and (ii) from $(0, 0)$ for M -interpolation.

broad, weak maximum.

Finally, Fig. 19 shows the quasi-particle weight $Z_{\mathbf{k}_0} = (1 - \partial_{\omega}\text{Re}\Sigma_{\mathbf{k}_0}(0))^{-1}$ along the “sign-change trajectory” through the BZ (the \mathbf{k}_0 -points where $\text{Re}G_{\mathbf{k}}(0)$ changes sign), i.e. along the trajectory that defines the Fermi and Luttinger surfaces. We compute the slope $\partial_{\omega}\text{Re}\Sigma_{\mathbf{k}_0}(0)$ via a linear fit, adjusting the fitting range along the sign-change trajectory to match appropriate fitting ranges found for our cluster data ($\omega_{\text{fit}} \sim \pm 10^{-6}$ for $\mathbf{k}_0 \sim (0, \pi)$ and $\omega_{\text{fit}} \sim \pm 10^{-4}$ for $\mathbf{k}_0 \sim (\pi/2, \pi/2)$). The resulting $Z_{\mathbf{k}_0}$ is depicted along the sign-change trajectory using a

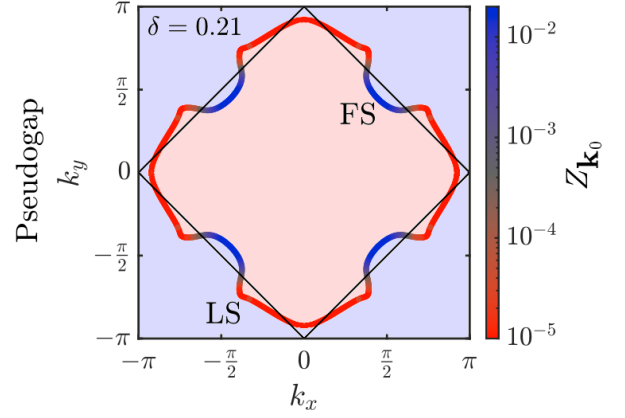


FIG. 19. Quasi-particle weight, $Z_{\mathbf{k}_0} = (1 - \partial_{\omega}\text{Re}\Sigma_{\mathbf{k}_0}(0))^{-1}$, for the pseudogap phase at $\delta = 0.21$, plotted along the “sign-change trajectory” in the BZ, i.e. along the locus of points \mathbf{k}_0 where $\text{Re}G_{\mathbf{k}}(0)$ changes sign. The color-scale shows the evolution from Fermi arcs (blue) to Luttinger arcs (red) and vice version when crossing the antiferromagnetic zone boundary (black lines). The light blue or red background shading indicates regions of the BZ with filling 1 or 0, respectively.

logarithmic red-to-blue color-scale. The blue portions of the trajectory correspond to a sign change via a divergence, i.e. a FS; the red portions correspond to a sign change via a smooth zero crossing, i.e. a LS. The evolution from Fermi arcs to Luttinger arcs and back occurs *smoothly*, in regions (shown in grey), that intersect the antiferromagnetic zone boundaries (straight black lines). (The reason why the quasi-particle weight is very small, $Z_{\mathbf{k}_0} \lesssim 0.02$, also along the FS parts of the sign-change trajectory is that $\delta = 0.21$ lies very close to a quantum phase transition, which will be the subject of a separate publication [67].)

To summarize: In the pseudogap regime, \mathcal{L} -interpolation, in contrast to Σ - and M -interpolation, yields a smooth evolution between hole-like Fermi arcs and Luttinger arcs, realizing these two concepts on one surface. The Fermi arcs lie within the AF zone boundaries, and the change to Luttinger arcs occurs while crossing these boundaries. In the literature, such a smooth FS-to-LS evolution has previously been found in a numerically demanding DGA study requiring the computation of two-particle quantities [84]. That this behavior can be obtained via \mathcal{L} -interpolation of computationally much cheaper DCA+NRG data constitutes a major result of our work. It illustrates that \mathcal{L} -interpolation is able to generate more intricate features than Σ - or M -interpolation, while preserving key qualitative properties of the cluster result, such as the hole-like character of the FS.

VI. SUMMARY AND OUTLOOK

In this paper, we introduced a scheme for interpolating CDMFT and DCA results through a suitable interpolation of single-particle irreducible Liouvillian matrix elements ϵ_n and \mathbf{t}_n . We showed (Sec. II) that these Liouvillian matrix elements are in fact coefficients of a continued fraction expansion of the dynamical part of the self-energy, $\Sigma^{\text{dyn}}(z)$ [Eq. (31)]. They can be obtained from the spectrum $\mathbf{W}(\omega)$ of the self-energy via a Lanczos scheme. The resulting matrix elements ϵ_n and \mathbf{t}_n are then interpolated (Sec. III) using a truncated Fourier ansatz to obtain $\epsilon_{\mathbf{K}n}$ and $\mathbf{t}_{\mathbf{K}n}$, which are inserted back to the CFE to obtain an interpolated self-energy, $\Sigma_{\mathbf{K}}(z)$.

Since the Liouvillian is independent of frequency, the same is true for its matrix elements ϵ_n and \mathbf{t}_n . Consequently, the interpolated version of the Liouvillian remains hermitian, which ensures causality. This poses an inherent advantage of our \mathcal{L} -scheme compared to traditional schemes, like Σ -, M -, and G -periodization.

To benchmark our \mathcal{L} -interpolation scheme (Sec. IV A), we considered the one-dimensional Hubbard model and computed its spectral function using TaSK [64], a numerically (almost) exact MPS method. We Fourier-transformed the TaSK results for G , Σ , M , and \mathcal{L} to position space and found that \mathcal{L} shows the most local behavior (its matrix elements decay most quickly with distance). Consequently, truncating the Fourier coefficients of \mathcal{L} by range yields a much more faithful representation of the true spectral function and self-energy than a corresponding truncation of Σ or M .

Next, we considered the same one-dimensional Hubbard model, but now treated with CDMFT for various cluster sizes, using TaSK [64] as an impurity solver (Sec. IV B). We compared the results obtained by interpolating its self-energy using the G -, Σ -, M -, and \mathcal{L} -schemes. We studied the convergence with cluster size of the interpolated CDMFT results to the benchmark TaSK results of Sec. IV A. For the 2-site cluster, \mathcal{L} -periodization arguably performed somewhat worse than G -periodization; but for 4- and 8-site clusters, \mathcal{L} -interpolation yielded smoother spectra that resembled the benchmark TaSK result much better.

Finally, we presented an example of DCA interpolation for the doped, two-dimensional t - t' Hubbard model, studied using four-patch DCA and an NRG impurity solver (Sec. V). We considered three choices of doping, yielding three distinct phases: a Fermi liquid, a pseudogap phase, and a Mott insulator. For each, we compared non-interpolated cluster result for the spectral function $A_{\mathbf{k}}(\omega)$ and self-energy $\Sigma_{\mathbf{k}}(\omega)$ to interpolated versions obtained via Σ -, M - and \mathcal{L} -interpolation.

We performed the CFE expansion of the DCA+NRG self-energy $\Sigma_{\mathbf{K}}(z)$ using a fast-slow splitting scheme (Sec. II H), implemented in such a manner that the resulting coefficients $\epsilon_{\mathbf{K}n}$, $\mathbf{t}_{\mathbf{K}n}$ and the fast-mode contributions $\mathbf{R}_{\mathbf{K}n}^{\text{F}}(z)$ decay exponentially with CFE depth n . The dependence of $\Sigma_{\mathbf{K}}(z)$ on the patch index \mathbf{K} is then mainly

encoded in the matrix elements $\epsilon_{\mathbf{K}n}$, $\mathbf{t}_{\mathbf{K}n}$, while the functions $\mathbf{R}_{\mathbf{K}n}^{\text{F}}(z)$ depend only weakly on \mathbf{K} and hence are easy to interpolate. Consequently, \mathcal{L} -interpolation yields better results than Σ - or M -interpolation: it produces more detailed structures with higher \mathbf{k} -space resolution, that better mimic key intrinsic features of the non-interpolated cluster results.

This is especially pronounced for Fermi surface properties (Sec. V C). Comparing the spectral functions $A_{\mathbf{k}}(\omega)$ obtained from the various interpolation schemes, we find that \mathcal{L} -interpolation resolves its structures most sharply. While all interpolations perform well for the Fermi liquid, the differences become strikingly apparent in the pseudogap phase. The \mathcal{L} -scheme interpolates the FS of the pseudogap phase to Fermi arcs, qualitatively similar to those observed in ARPES experiments. The \mathcal{L} -scheme also is the one that best mimics the non-interpolated cluster results, not only for the Fermi surface but also for the quasi-particle weight, as illustrated by tracking $\max[A_{\mathbf{k}}(0)]$ along the Fermi surface. Perhaps most remarkably, \mathcal{L} -interpolation yields a smooth evolution between Fermi and Luttinger surfaces, similar to that found previously using computationally much more costly DGA computations [84].

In summary, we presented a Liouvillian interpolation scheme for cluster DMFT data. Exploiting the fact that the spectral function and self-energy can be fully expressed through matrix elements of the Liouvillian, our key idea is to interpolate the latter. This yields causal results, because these matrix elements are independent of frequency. We interpolate them using a real-space-truncated Fourier expansion, exploiting the fact that the real-space matrix elements of the Liouvillian \mathcal{L} are more local than those of Green's function G , self-energy Σ or cumulant M . Liouvillian periodization yields results with better \mathbf{k} -space resolution than traditional periodization schemes, because it distributes \mathbf{k} -space information among a large number of Liouvillian matrix elements.

In this paper, we discussed interpolation as a post-processing tool, to be used after DMFT self-consistency has been achieved. This is to be distinguished from interpolation *within* cDMFT loops. The latter can yield non-causal hybridization functions if the standard self-consistency equations are used, but this causality issue has recently been solved with the generalized cavity construction of Ref. [85]. In future work, it would be interesting to set up within-cDMFT-interpolations that combine the generalized cavity construction with \mathcal{L} -interpolation.

Final remarks: Liouvillian interpolation can be used in any context requiring the interpolation of frequency-dependent dynamical response functions, making it relevant also for other quantum many-body embedding methods beyond cDMFT. Even more generally, the CFE representation of the Green's function or the self-energy through *Liouvillian* matrix elements, as described in Sec. II, constitutes a versatile tool that promises to be useful also in contexts other than interpolation.

Acknowledgements

We deeply thank André-Marie Tremblay and his group for providing their ED data to test our \mathcal{L} -interpolation scheme during early stages of this work. We also thank Benjamin Bacq-Labreuil, Pierre-Olivier Downey, Antoine Georges, Maurits Haverkort, Seung-Sup Lee, Gabriel Kotliar, André-Marie Tremblay and Aleksandrs Zacinskis for inspiring discussions. We acknowledge the Gauss Centre for Supercomputing e.V. (www.gauss-centre.eu) for funding this project by providing computing time on the GCS Supercomputer SUPERMUC-NG at Leibniz Supercomputing Centre (www.lrz.de). We also acknowledge additional computational resources provided by the Arnold Sommerfeld Center for theoretical physics (www.theorie.physik.uni-muenchen.de). This work was supported in part by the Deutsche Forschungsgemeinschaft under grants INST 86/1885-1 FUGG, LE 3883/2-2 and Germany's Excellence Strategy EXC-2111 (Project No. 390814868). It is part of the Munich Quantum Valley, supported by the Bavarian state government with funds from the Hightech Agenda Bayern Plus. The National Science Foundation supported JvD in part under PHY-1748958. AG acknowledges support from the Abrahams Postdoctoral Fellowship of the Center for Materials Theory at Rutgers University.

Appendix A: Operator inner product for $T = 0$

This appendix discusses subtleties arising in the definition of operator inner products at zero temperature.

The operator inner product $(|)$ of Eq. (5) is well-defined only if ρ has full rank, i.e. if $\langle \Psi | \rho | \Psi \rangle \neq 0$ for every state $|\Psi\rangle \in \mathbb{V}$; otherwise $|\Psi\rangle\langle\Psi|$ would have zero norm w.r.t $(|)$ despite being a nonzero operator. The thermal density matrix ρ does have full rank for $T \neq 0$. However, the zero-temperature density matrix, $\rho_G = \rho(T=0)$, does not have full rank, since $\langle \Psi | \rho_G | \Psi \rangle \neq 0$ only if $|\Psi\rangle \in \mathbb{V}_G$, the ground state subspace of \mathbb{V} . In this case, we restrict attention to $\mathbb{W}_G = \{O_G\}$, the space of all operators with the property that either O_G or O_G^\dagger does not annihilate all ground states. For any $|O\rangle \in \mathbb{W}$, its projection into \mathbb{W}_G is defined as $|O_G\rangle = \mathcal{P}_G|O\rangle = |O - \overline{P}_G O \overline{P}_G\rangle$. Here $\overline{P}_G = \mathbb{1} - P_G$, where P_G and \overline{P}_G respectively are projectors onto the ground state subspace \mathbb{V}_G and its complement, $\overline{\mathbb{V}}_G$, the space of excited states, defined such that $\mathbb{V} = \mathbb{V}_G \oplus \overline{\mathbb{V}}_G$. The projector property $\mathcal{P}_G^2 = \mathcal{P}_G$ is readily verified. For $T = 0$, the inner product is well-defined on \mathbb{W}_G : indeed, it yields

$$(O_G|O_G) = \text{Tr}[\rho_G\{O_G^\dagger, O_G\}] = \text{Tr}[\rho_G\{O^\dagger, O\}], \quad (\text{A1})$$

since $\rho_G \overline{P}_G = \overline{P}_G \rho_G = 0$. If $|O_G\rangle \neq 0$, then $O \neq \overline{P}_G O \overline{P}_G$, hence O or O^\dagger does not annihilate \mathbb{V}_G ; thus the right side of Eq. (A1), and hence also $(O_G|O_G)$, is nonzero.

Appendix B: Measures, the moment problem, and orthogonal polynomials

In this Appendix, we provide some background material on moment problems, measures, and their relation to orthogonal polynomials. This material is used implicitly in Sec. II on CFE representations of Liouvillian dynamics: it forms the basis for our statement there that the CFE coefficients for a Green's function $\mathbf{G}(z)$ or its self-energy $\Sigma(z)$ are the same, although their spectral functions, $\mathbf{A}(\omega)$ or $\mathbf{W}(\omega)$, generate two different sets of orthogonal polynomials. All the information presented below is well-established and can be found in numerous textbooks [86–92] and articles [93–98].

Let μ be a positive semidefinite, hermitian $M \times M$ matrix-valued Borel measure on \mathbb{R} ; that is, $\mu : \mathcal{B}(\mathbb{R}) \rightarrow \mathbb{C}^{M \times M}$ is countably additive and $\mu(B)$ is positive semidefinite for all Borel sets B . We write, distributionally,

$$\mu(d\omega) = \mathbf{A}(\omega)d\omega, \quad (\text{B1})$$

with a spectral function $\mathbf{A}(\omega) = \mathbf{A}_c(\omega) + \sum_\alpha \mathbf{A}_\alpha \delta(\omega - \omega_\alpha)$ that exhibits both a continuous part $\mathbf{A}_c(\omega)$ and point masses with weights \mathbf{A}_α , encoded by the δ -terms. We further assume the normalization

$$\mu(\mathbb{R}) = \int_{-\infty}^{\infty} d\omega \mathbf{A}(\omega) = \mathbf{1}, \quad (\text{B2})$$

where $\mathbf{1}$ is the $M \times M$ unit matrix.

The Stieltjes transform of μ is defined as

$$\mathbf{G}(z) = \int_{\mathbb{R}} \frac{\mu(d\omega)}{z - \omega}, \quad z \in \mathbb{C} \setminus \mathbb{R}. \quad (\text{B3})$$

The spectral function can be recovered from $\mathbf{G}(z)$ via

$$\mathbf{A}(\omega) = \frac{i}{2\pi} [\mathbf{G}(\omega^+) - \mathbf{G}(\omega^+)^{\dagger}], \quad (\text{B4})$$

with $\omega^+ = \omega + i0^+$.

The (equivalence classes of) square-integrable vector fields $f : \mathbb{R} \rightarrow \mathbb{C}^M$ with respect to μ form the Hilbert space $L^2(\mu)$, with inner product

$$\langle g, f \rangle = \int_{\mathbb{R}} g^\dagger(\omega) \mu(d\omega) f(\omega) \in \mathbb{C}. \quad (\text{B5})$$

In the following, we write $|f\rangle \in L^2(\mu)$ for the vector which is represented by the vector field $f(\omega)$. For later usage, we further define blocks of M vectors by a bold symbol $|\mathbf{f}\rangle = (|f_1\rangle, \dots, |f_M\rangle)$. Similarly, $\mathbf{f}(\omega) = (f_1(\omega), \dots, f_M(\omega)) \in \mathbb{C}^{M \times M}$ denotes the block of representing vector fields. Furthermore, $\langle \mathbf{g}, \mathbf{f} \rangle$ denotes a column vector with α -th entry $\langle g_\alpha, f \rangle$, $\langle \mathbf{f}, \mathbf{g} \rangle = \langle \mathbf{g}, \mathbf{f} \rangle^\dagger$ a corresponding row vector, and $\langle \mathbf{g}, \mathbf{f} \rangle$ a matrix with entries $\langle g_\alpha, f_\beta \rangle$. For a more formal treatment of matrix-valued measures and their L^2 spaces, see Ref. 92, pages 1337 and onward.

The (matrix) moments of μ are

$$\mathbf{m}_n = \int_{\mathbb{R}} \mu(d\omega) \omega^n, \quad (\text{B6})$$

with $n = 0, 1, 2, \dots$ and hermitian \mathbf{m}_n . Throughout, we assume that all moments in (B6) are finite.

The (matrix-valued) *moment problem* asks: given a sequence of hermitian matrices $\{\mathbf{m}_n\}_{n \geq 0}$, (i) does there exist a positive semidefinite, hermitian matrix-valued Borel measure μ on \mathbb{R} with moments (B6); and (ii) if so, is it unique? In our setting we start from μ (equivalently, from the spectral function $\mathbf{A}(\omega)$) and compute $\{\mathbf{m}_n\}$, so existence is automatic. Uniqueness, however, is not guaranteed: if exactly one representing measure has the moments (B6), the problem is determinate; otherwise, it is indeterminate.

A sufficient condition for a unique measure (determinate moment problem) is either a compact support of the spectral function $\mathbf{A}(\omega)$, or an exponential decay at large $|\omega|$. Spectral functions of finite-size fermionic systems, even if macroscopically large, fulfill these conditions. We therefore assume that the moment problem is determinate in our work, i.e., the spectral function $\mathbf{A}(\omega)$ having these moments is unique.

In the determinate case, Eq. (B6) can be used to generate a set of orthonormal polynomials that form a complete orthonormal basis of $L^2(\mu)$ (c.f. Eq. (B7) below): every $|f\rangle \in L^2(\mu)$ admits a unique L^2 -expansion in these polynomials. By contrast, in the indeterminate case, there exist representing measures μ for which the orthonormal polynomials are *not* a complete basis of $L^2(\mu)$. For example, this is the case for a log-Gaussian spectral function. Nevertheless, the same moment sequence admits a family of representing measures (the Nevanlinna-extremal measures) for which the corresponding orthonormal block polynomials *are* a complete orthonormal basis of $L^2(\mu)$, see, for instance, Refs. 97 and 99.

We caution that some popular broadening kernels used in DMFT computations spoil determinacy or even moment existence. The log-Gaussian kernel, a standard kernel used to broaden discrete NRG spectra, has indeterminate moments, see Sec. 11.2 of Ref. 91. The Lorentzian kernel, a common choice for broadening discrete finite-size spectra, has no finite moments of order > 1 . In such cases, one should either work with the underlying discrete data when possible, or use the slow-fast mode splitting described in Sec. E2. In these cases, the loss of determinacy is an artifact of the long high-frequency tails of the broadening kernel and is unrelated to the underlying physics.

The block Lanczos algorithm described in Eq. (38) can be used to construct an orthonormal polynomial basis,

$$\langle \mathbf{p}_n, \mathbf{p}_{n'} \rangle = \int_{\mathbb{R}} d\omega \mathbf{p}_n^\dagger(\omega) \mathbf{A}(\omega) \mathbf{p}_{n'}(\omega) = \delta_{nn'} \mathbf{1}. \quad (\text{B7})$$

Here, every column of $\mathbf{p}_n(\omega)$ is a degree n polynomial \mathbb{C}^M vector field. The Lanczos algorithm also generates

the hermitian matrices ϵ_n and positive semidefinite hermitian matrices \mathbf{t}_n . The polynomials $\mathbf{p}_n(\omega)$ obey a three-term recursion relation

$$\omega \mathbf{p}_n(\omega) = \mathbf{p}_n(\omega) \epsilon_n + \mathbf{p}_{n+1}(\omega) \mathbf{t}_{n+1} + \mathbf{p}_{n-1}(\omega) \mathbf{t}_n, \quad (\text{B8})$$

with initial conditions $\mathbf{p}_{-1}(\omega) = \mathbf{0}$ and $\mathbf{p}_0(\omega) = \mathbf{1}$.

While the Lanczos procedure takes a given measure μ as input to generate polynomials satisfying the recursion relation (B8), one may ask, conversely: given such a recursion relation, are the polynomials generated from it orthonormal w.r.t. some measure? The answer is yes: Favard's theorem guarantees that polynomials that obey the three-term recursion (B8), with initial condition $\mathbf{p}_{-1}(\omega) = \mathbf{0}$ and $\mathbf{p}_0(\omega) = \mathbf{1}$, are orthogonal w.r.t. at least one measure μ . The measure is unique if its moment problem is determinate, a property that can also be determined from the coefficients ϵ_n and \mathbf{t}_n [94–96].

The three-term recursion can be used to generate an infinite-depth CFE for $\mathbf{G}(z)$, the Stieltjes transform of $\mathbf{A}(\omega)$, of the form (with $\mathbf{z}_n = \mathbf{z} - \epsilon_n$)

$$\mathbf{G}(z) = \frac{1}{\mathbf{z}_0 - \mathbf{t}_1 \frac{1}{\mathbf{z}_1 - \mathbf{t}_2 \frac{1}{\mathbf{z}_2 - \dots}}}. \quad (\text{B9})$$

Another set of matrix polynomials, called *associated polynomials of the first kind* and denoted $\mathbf{p}_n^{(1)}(\omega)$, is obtained if the recursion relation Eq. (B8) (with the same coefficients ϵ_n and \mathbf{t}_n) is initialized with the initial conditions $\mathbf{p}_{-1}^{(1)}(\omega) = \mathbf{0}$, $\mathbf{p}_0^{(1)}(\omega) = \mathbf{0}$ and $\mathbf{p}_1^{(1)}(\omega) = \mathbf{1}$. Then, $\mathbf{p}_n^{(1)}(\omega)$ is a polynomial of degree $n - 1$. The $\mathbf{p}_n^{(1)}(\omega)$ and $\mathbf{p}_n(\omega)$ polynomials are related via the integral

$$\mathbf{p}_n^{(1)}(\omega) = \int_{\mathbb{R}} d\omega' \mathbf{t}_1 \mathbf{A}(\omega') \frac{\mathbf{p}_n(\omega) - \mathbf{p}_n(\omega')}{\omega - \omega'}, \quad (\text{B10})$$

as follows readily by induction using Eq. (B8). Now, Favard's theorem tells us that there is at least one measure w.r.t. which these polynomials are orthonormal, say $\mu^{(1)}$, with $\mu^{(1)}(d\omega) = \mathbf{A}^{(1)}(\omega) d\omega$. Moreover, since we have assumed that the moment problem of μ is determinate, the same is true for the measure $\mu^{(1)}$, which therefore is unique.

The three-term recursion relation also tells us that the Stieltjes transform of $\mu^{(1)}$, say $\mathbf{G}^{(1)}(z)$, has the infinite-depth CFE

$$\mathbf{G}^{(1)}(z) = \frac{1}{\mathbf{z}_1 - \mathbf{t}_2 \frac{1}{\mathbf{z}_2 - \mathbf{t}_3 \frac{1}{\mathbf{z}_3 - \dots}}}, \quad (\text{B11})$$

involving the *same* CFE coefficients $\epsilon_{n \geq 1}$, $\mathbf{t}_{n \geq 2}$ as $\mathbf{G}(z)$ of Eq. (B9). Therefore, $\mathbf{G}^{(1)}(z)$ and $\mathbf{G}(z)$ are related by

$$\mathbf{G}(z) = \frac{1}{\mathbf{z}_0 - \mathbf{t}_1 \mathbf{G}^{(1)}(z) \mathbf{t}_1}, \quad (\text{B12a})$$

$$\mathbf{G}^{(1)}(z) = \mathbf{t}_1^{-1} [\mathbf{z}_0 - \mathbf{G}^{-1}(z)] \mathbf{t}_1^{-1}. \quad (\text{B12b})$$

The spectral density $\mathbf{A}^{(1)}(\omega)$ of $\mathbf{G}^{(1)}(z)$ can be obtained explicitly, if needed, by inserting Eq. (B12b) into a relation analogous to Eq. (B4).

The above framework is directly relevant for our discussion in Sec. IID. Identifying the functions $\mathbf{G}(z)$ and $\mathbf{A}(\omega)$ discussed above with the epimous Green's function and spectral function there, and Eq. (B12a) with the Dyson equation (9), we note that $\mathbf{G}^{(1)}(z)$ and $\mathbf{A}^{(1)}(\omega)$ correspond to the functions $\mathbf{S}(z)$ and $\mathbf{W}(\omega)$ characterizing the dynamical part of the self-energy, $\Sigma^{\text{dyn}}(z) = \mathbf{t}_1 \mathbf{S}(z) \mathbf{t}_1^\dagger$. Thus, the two sets of orthogonal block polynomials generated from measures involving the spectral functions $\mathbf{A}(\omega)$ or $\mathbf{W}(\omega)$ of the Green's function or its self-energy, respectively, are related; the polynomials generated from $\mathbf{W}(\omega)$ are associated polynomials of the first kind w.r.t. to the polynomials generated from $\mathbf{A}(\omega)$. (That is why we put the superscript on $\mathbf{p}_n^{(1)}$ in Sec. IID.) Moreover, the coefficients $\epsilon_{n \geq 1}$ and $\mathbf{t}_{n \geq 2}$ generated using either $\mathbf{W}(\omega)$ or $\mathbf{A}(\omega)$ are identical. We also note that the computational steps involved in obtaining the CFE (B9) for $\mathbf{G}(z)$ are entirely analogous to those presented in Sec. IIE for obtaining the CFE (31) for $\mathbf{S}(z)$, with $\mathbf{W}(\omega)$ there now replaced by $\mathbf{A}(\omega)$.

Appendix C: Matrix elements of inverse matrices

This appendix collects elementary identities, needed in the main text, expressing the 11-blocks of inverses of block matrices through Schur complements. All (block) matrix inverses appearing below are assumed to exist.

Let $A = \begin{pmatrix} A_{11} & A_{12} \\ A_{21} & A_{22} \end{pmatrix}$ be an invertible 2×2 block matrix, then the 11-block of its inverse is given by

$$(A^{-1})_{11} = [A/A_{22}]^{-1}, \quad (\text{C1a})$$

$$[A/A_{22}] = A_{11} - A_{12}(A_{22})^{-1}A_{21}. \quad (\text{C1b})$$

$[A/A_{22}]$ is known as the Schur complement of A w.r.t. block A_{22} . Equations (C1) can be used to obtain similar expressions for the 11-blocks of larger block matrices. Let A be a 3×3 block matrix and B a 2×2 submatrix,

$$A = \begin{pmatrix} A_{11} & A_{12} & A_{13} \\ A_{21} & A_{22} & A_{23} \\ A_{31} & A_{32} & A_{33} \end{pmatrix}, \quad B = \begin{pmatrix} A_{22} & A_{23} \\ A_{32} & A_{33} \end{pmatrix}, \quad (\text{C2})$$

then the 11-block of A^{-1} , found using Eq. (C1) with A_{22} replaced by B and A_{12} by (A_{12}, A_{13}) , etc., is given by

$$(A^{-1})_{11} = [A/B]^{-1}, \quad (\text{C3a})$$

$$[A/B] = A_{11} - (A_{12}, A_{13}) (B)^{-1} \begin{pmatrix} A_{21} \\ A_{31} \end{pmatrix}. \quad (\text{C3b})$$

If $A_{23} = A_{32} = 0$, the Schur complement $[A/B]$ becomes

$$[A/B] = A_{11} - A_{12}(A_{22})^{-1}A_{21} - A_{13}(A_{33})^{-1}A_{31}. \quad (\text{C4})$$

If instead $A_{13} = A_{31} = 0$, we have

$$[A/B] = A_{11} - A_{12}(B^{-1})_{22}A_{21}. \quad (\text{C5})$$

Finally, let A be an invertible $N \times N$ tridiagonal block matrix, defined recursively, with $n = 1, \dots, N-1$:

$$A = (\bar{A}_{11}), \quad \bar{A}_{nn} = \begin{pmatrix} A_{nn} & A_{n,n+1} & 0 & \dots & 0 \\ A_{n+1,n} & & & & \\ 0 & & \bar{A}_{n+1,n+1} & & \\ \vdots & & & & \\ 0 & & & & \end{pmatrix}. \quad (\text{C6})$$

Then, recursive use of Eq. (C5) yields (with $n' = n+1$):

$$(A^{-1})_{11} = [\bar{A}_{11}/\bar{A}_{22}]^{-1}, \quad (\text{C7a})$$

$$[\bar{A}_{nn}/\bar{A}_{n'n'}]^{-1} = A_{nn} - A_{nn'}(\bar{A}_{n'n'})_{11}^{-1}A_{n'n}, \quad (\text{C7b})$$

This leads to a CFE for the 11-block of A^{-1} :

$$\left(\frac{1}{A}\right)_{11} = \frac{1}{A_{11} - A_{12} \frac{1}{A_{22} - \dots - A_{N-1,N} \frac{1}{A_{NN}} A_{N,N-1}}}. \quad (\text{C8})$$

Appendix D: Finding the residual function $\mathbf{R}_N(z)$

In this appendix, we provide technical details underlying two results stated in the main text, for (i) the CFE representations of $\mathbf{G}(z)$ (see Eq. (46)), and (ii) the residual functions terminating these CFEs (see Eqs. (43)).

We consider the space, $L^2(\boldsymbol{\mu})$, of functions that are square integrable against a measure $\boldsymbol{\mu}$, that is such that $L^2(\boldsymbol{\mu})$ contains block polynomials of arbitrary degree. For definiteness, we consider the case $\boldsymbol{\mu}^{(1)}(d\omega) = \mathbf{W}(\omega)d\omega$, where $\mathbf{W}(\omega)$, the normalized spectral function of the dynamical part of the self-energy $\Sigma^{\text{dyn}}(z)$, is assumed to be known analytically or numerically. (An analogous discussion applies for $\boldsymbol{\mu}(d\omega) = \mathbf{A}(\omega)d\omega$, where $\mathbf{A}(\omega)$ is the spectral function of $\mathbf{G}(\omega)$.) In this space, the Liouvillian $\hat{\mathcal{L}}$ acts on functions $\mathbf{f} \in L^2(\boldsymbol{\mu})$ according to $\hat{\mathcal{L}}\mathbf{f}(\omega) = \omega \mathbf{f}(\omega)$ (cf. Eq. (14b)). Since $\hat{\mathcal{L}}$ is self-adjoint and therefore has a real spectrum, $(z - \hat{\mathcal{L}})$ with $\text{Im } z \neq 0$ is a normal operator that is invertible.

In Sec. IIE, a Lanczos scheme is used to generate blocks of vector-valued polynomials, $\{\mathbf{p}_n^{(1)}(\omega), n = 1, \dots, N\}$, that are orthogonal w.r.t. $\boldsymbol{\mu}^{(1)}$ (cf. Eq. (37a)). These polynomials span an NM -dimensional subspace of $L^2(\boldsymbol{\mu})$, the space of vector-valued polynomials with degree $\leq N-1$. We call the projector onto this space \mathcal{P}_N , while $\bar{\mathcal{P}}_N$ projects onto its orthonormal complement (such that $\mathcal{P}_N + \bar{\mathcal{P}}_N = \mathbb{1}$). In the polynomial basis, the single-particle irreducible Liouvillian $\hat{\mathcal{L}}_{\bar{\mathcal{P}}_N}$ is represented by an $N \times N$ block-tridiagonal matrix (cf. Eq. (37b)). This block-tridiagonal structure implies a block-CFE for $\mathbf{S}(z) = \langle \mathbf{p}_1^{(1)}, (z - \hat{\mathcal{L}}_{\bar{\mathcal{P}}_N})^{-1} \mathbf{p}_1^{(1)} \rangle$, which is terminated by a residual function, $\mathbf{R}_N(z)$, that ensures the representation is exact (cf. Eq. (42)). With Eqs. (43), we provided a formula for this residual function. Below, we derive this

formula. The explicit construction of $\mathbf{R}_N(z)$ (i) shows its existence, and (ii) will also show that there exists a measure μ_N such that

$$\mathbf{R}_N(z) = \int \frac{\mu_N(d\omega)}{z - \omega}. \quad (\text{D1})$$

Following the notation of Sec. II, we denote projections onto \mathcal{P}_N and $\bar{\mathcal{P}}_N$ by indices p and \bar{p} , and blocks of matrix representations by square brackets with indices \mathbf{p} and $\bar{\mathbf{p}}$, respectively. By applying formula (C1), we find

$$\begin{aligned} [(z - \hat{\mathcal{L}}_{\bar{c}\bar{c}})^{-1}]_{\mathbf{p}\mathbf{p}} &= \\ &= (z - [\hat{\mathcal{L}}]_{\mathbf{p}\mathbf{p}} - [\hat{\mathcal{L}}_{p\bar{p}}(z - \hat{\mathcal{L}}_{\bar{p}\bar{p}})^{-1}\hat{\mathcal{L}}_{\bar{p}p}]_{\mathbf{p}\mathbf{p}})^{-1}. \end{aligned} \quad (\text{D2})$$

Here, $[\hat{\mathcal{L}}]_{\mathbf{p}\mathbf{p}}$, represented in the polynomial basis \mathbf{p}_n , is the tridiagonal matrix Eq. (37b). From the three-term recursion for the polynomials \mathbf{p}_n [Eq. (39)], it follows that

$$\bar{\mathcal{P}}_N \hat{\mathcal{L}} \mathbf{p}_n^{(1)}(\omega) = \delta_{nN} \mathbf{p}_{N+1}^{(1)}(\omega) \mathbf{t}_{N+1}. \quad (\text{D3})$$

For $[\hat{\mathcal{L}}_{p\bar{p}}(z - \hat{\mathcal{L}}_{\bar{p}\bar{p}})^{-1}\hat{\mathcal{L}}_{\bar{p}p}]_{nn'}$, with $n, n' \leq N$, this implies

$$\langle \mathbf{p}_n^{(1)}, \hat{\mathcal{L}}_{p\bar{p}}(z - \hat{\mathcal{L}}_{\bar{p}\bar{p}})^{-1}\hat{\mathcal{L}}_{\bar{p}p} \mathbf{p}_{n'}^{(1)} \rangle = \delta_{nN} \delta_{n'N} \mathbf{R}_N(z), \quad (\text{D4a})$$

$$\mathbf{R}_N(z) = \mathbf{t}_{N+1} (\mathbf{p}_{N+1}^{(1)}, (z - \hat{\mathcal{L}}_{\bar{p}\bar{p}})^{-1} \mathbf{p}_{N+1}^{(1)}) \mathbf{t}_{N+1}. \quad (\text{D4b})$$

Equation (D4a) shows by explicit construction that the only nonzero block of $\hat{\mathcal{L}}_{p\bar{p}}(z - \hat{\mathcal{L}}_{\bar{p}\bar{p}})^{-1}\hat{\mathcal{L}}_{\bar{p}p}$ is its NN block; we denote it by $\mathbf{R}_N(z)$. Equation (D4b) expresses it through the $N+1, N+1$ block of $(z - \hat{\mathcal{L}}_{\bar{p}\bar{p}})^{-1}$, exploiting Eq. (D3), whose left side provides a link (the only one available!) between the $\bar{\mathcal{P}}_N$ and \mathcal{P}_N sectors. Further, Eq. (D1) immediately follows from an explicit construction of the measure,

$$\mu_N(d\omega) = \mathbf{t}_{N+1} \langle \mathbf{p}_{N+1}, \delta(\omega - \hat{\mathcal{L}}_{\bar{p}\bar{p}}) \mathbf{p}_{N+1} \rangle \mathbf{t}_{N+1} d\omega. \quad (\text{D5})$$

To arrive at Eq. (43) for the residual function, we consider the inverse of the matrix in Eq. (D2), which is a block-tridiagonal matrix:

$$[[(z - \hat{\mathcal{L}}_{\bar{c}\bar{c}})^{-1}]_{\mathbf{p}\mathbf{p}}]^{-1} = \begin{pmatrix} \mathbf{z}_1 & \mathbf{t}_2 & \cdots & \mathbf{0} & \mathbf{0} & \mathbf{0} \\ \mathbf{t}_2 & \mathbf{z}_2 & \cdots & \mathbf{0} & \mathbf{0} & \mathbf{0} \\ \vdots & \vdots & \ddots & \vdots & \vdots & \vdots \\ \mathbf{0} & \mathbf{0} & \cdots & \mathbf{z}_{N-2} & \mathbf{t}_{N-1} & \mathbf{0} \\ \mathbf{0} & \mathbf{0} & \cdots & \mathbf{t}_{N-1} & \mathbf{z}_{N-1} & \mathbf{t}_N \\ \mathbf{0} & \mathbf{0} & \cdots & \mathbf{0} & \mathbf{t}_N & \tilde{\mathbf{z}}_N \end{pmatrix}. \quad (\text{D6})$$

Here, $\mathbf{z}_n(z) = \mathbf{z} - \epsilon_n$ and $\tilde{\mathbf{z}}_N(z) = \mathbf{z}_N - \mathbf{R}_N(z)$. The NN block contains an extra term, the residual function $\mathbf{R}_N(z)$ of Eqs. (D4).

Using $[[(z - \hat{\mathcal{L}}_{\bar{c}\bar{c}})^{-1}]_{\mathbf{p}\mathbf{p}}]^{-1} [(z - \hat{\mathcal{L}}_{\bar{c}\bar{c}})^{-1}]_{\mathbf{p}\mathbf{p}} = \mathbb{1}_{\mathbf{p}\mathbf{p}}$, where $\mathbb{1}_{\mathbf{p}\mathbf{p}}$ is the identity in the pp block, and exploiting the tridiagonal form of $[[(z - \hat{\mathcal{L}}_{\bar{c}\bar{c}})^{-1}]_{\mathbf{p}\mathbf{p}}]^{-1}$ (cf. Eq. (D6)),

we arrive at the equations

$$\begin{aligned} \left([[(z - \hat{\mathcal{L}}_{\bar{c}\bar{c}})^{-1}]_{\mathbf{p}\mathbf{p}}]^{-1} [(z - \hat{\mathcal{L}}_{\bar{c}\bar{c}})^{-1}]_{\mathbf{p}\mathbf{p}} \right)_{NN-1} &= \\ \mathbf{t}_N \mathbf{G}_N(z) + \tilde{\mathbf{z}}_N \tilde{\mathbf{F}}_N^L(z) &= \mathbf{0}, \end{aligned} \quad (\text{D7a})$$

$$\begin{aligned} \left([[(z - \hat{\mathcal{L}}_{\bar{c}\bar{c}})^{-1}]_{\mathbf{p}\mathbf{p}}]^{-1} [(z - \hat{\mathcal{L}}_{\bar{c}\bar{c}})^{-1}]_{\mathbf{p}\mathbf{p}} \right)_{NN} &= \\ \tilde{\mathbf{F}}_N^R(z) + \tilde{\mathbf{z}}_N \tilde{\mathbf{I}}_N(z) &= \mathbf{1}. \end{aligned} \quad (\text{D7b})$$

Here, we have used the definitions

$$\mathbf{G}_N(z) = [(z - \hat{\mathcal{L}})^{-1}]_{N-1N-1} \quad (\text{D8a})$$

$$\tilde{\mathbf{F}}_N^L(z) = [(z - \hat{\mathcal{L}})^{-1}]_{NN-1} \quad (\text{D8b})$$

$$\tilde{\mathbf{F}}_N^R(z) = [(z - \hat{\mathcal{L}})^{-1}]_{N-1N} \quad (\text{D8c})$$

$$\tilde{\mathbf{I}}_N(z) = [(z - \hat{\mathcal{L}})^{-1}]_{NN}. \quad (\text{D8d})$$

By rearranging Eq. (D7), we arrive at the relation

$$\tilde{\mathbf{z}}_N^{-1} = \tilde{\mathbf{I}}_N - \tilde{\mathbf{F}}_N^L \mathbf{G}_N^{-1} \tilde{\mathbf{F}}_N^R. \quad (\text{D9})$$

Now, the 00-element of the inverse of Eq. (D6) is explicitly presented by a CFE that is terminated at level $N-1$ by $\mathbf{z}_{N-1} - \mathbf{t}_N \tilde{\mathbf{z}}_N^{-1} \mathbf{t}_N$. Equating this to $\mathbf{z}_{N-1} - \mathbf{R}_{N-1}$ and using (D9) yields

$$\mathbf{R}_{N-1} = \mathbf{t}_N (\tilde{\mathbf{I}}_N - \tilde{\mathbf{F}}_N^L \mathbf{G}_N^{-1} \tilde{\mathbf{F}}_N^R) \mathbf{t}_N. \quad (\text{D10})$$

Defining $\mathbf{I}_N = \mathbf{t}_N \tilde{\mathbf{I}}_N \mathbf{t}_N$, $\mathbf{F}_N^L = \mathbf{t}_N \tilde{\mathbf{F}}_N^L$, $\mathbf{F}_N^R = \tilde{\mathbf{F}}_N^R \mathbf{t}_N$, and using $\mathbf{p}_N^{(1)} \mathbf{t}_N = \mathbf{p}_N^{(1)\perp}$, we get Eq. (43) of the main text.

To conclude this appendix, we note that the residual functions can also be computed recursively: By equating two exact CFEs for $\Sigma^{\text{dyn}}(z)$ of the form (42), having depth $N-1$ or N , we obtain a recursion relation for the residual functions:

$$\mathbf{R}_N(z) = \mathbf{z}_N - \mathbf{t}_N \mathbf{R}_{N-1}^{-1}(z) \mathbf{t}_N. \quad (\text{D11})$$

Starting from $\mathbf{R}_0(z) = \Sigma^{\text{dyn}}(z)$, this equation can in principle be used recursively to compute the residual functions to any required depth. However, using Eq. (D11) turns out to be numerically less stable than using Eq. (D10). Though both involve a difference between two terms, one of which involves a matrix inversion, the quotient of z -dependent functions $\mathbf{F}_N(z) \mathbf{G}_N^{-1}(z) \mathbf{F}_N(z)$ turns out to have better numerical stability than $\mathbf{t}_N \mathbf{R}_{N-1}^{-1}(z) \mathbf{t}_N$, involving just one z -dependent function in the denominator. One reason for the improved stability of Eq. (D10) is that its right side falls off with z^{-1} at large $|z|$ by construction, while Eq. (D11) relies on precise cancellations at high frequencies to produce z^{-1} behavior.

Finally, we note that an equation structurally similar to Eq. (D10) was obtained by Kugler [66] (see his Eq. (12)) in the context of computing self-energies via symmetric improved estimators. He gives a detailed discussion of the numerical stability of this construction.

Appendix E: Numerical computation of the continued fraction expansion

We compute single-particle irreducible Liouvillian matrix elements by constructing a continued fraction expansion of the self-energy through iterative application of the Liouvillian to the initial state, as described in Sec. II. This section outlines our numerical implementation, designed to construct the CFE of any function of form (22).

1. Liouvillian matrix elements

Our numerical implementation constructs the orthonormal polynomial basis $\{\mathbf{p}(\omega)\}_{1,\dots,N}$ of Sec. II E, using the spectrum of the self-energy as input. A pseudocode for our algorithm is presented in Alg. 1.

Note that a discrete system yields polynomials of discrete frequencies. Due to the discrete nature of the spectrum, the dimension of the Liouvillian and corresponding Krylov space, N , equals the number of discrete energies. As a result, the Lanczos procedure terminates after N steps exactly representing the discrete self-energy without any rest function $\mathbf{R}_N(z)$.

If the spectrum is not discrete, the rest function $\mathbf{R}_N(z)$ can be computed using Eqs. (43). Note that this requires first computing the polynomial $\mathbf{p}_{N+1}^{(1)}(\omega)$.

2. Rest function and F/S-modes

After terminating the Lancos scheme at step N and evaluating the rest function, it has to be interpolated together with the matrix elements ϵ_N and \mathbf{t}_N . However, to gain an advantage compared to standard interpolation schemes, the rest function must have a much weaker \mathbf{k} -dependence than the Liouvillian matrix elements. A weak \mathbf{k} -dependence is not guaranteed *a priori* for any termination point N . Additionally, the broadening of the CFE to obtain a smooth function of frequency is entirely governed by the rest function (unless poles at individual CFE steps are broadened by hand, which we prefer to avoid). A strategy addressing these issues is to split the rest function into slow and fast modes, as described next.

Our solution is based on the open Wilson chain approach of Ref. 61, as mentioned in the main text (Sec. II H). For convenience, we repeat here our choice for the splitting function $w_n^{S/F}(\omega)$, that fulfill $w_n^F(\omega) + w_n^S(\omega) = 1$. Our choice is a box function,

$$w_n^S(\omega) = \frac{1}{1 + |\omega/\Omega_n|^\tau}, \quad (\text{E1})$$

with half-bandwidth $\Omega_n = \Omega_{\max}\Lambda^{1-n}$ (where $\Lambda > 1$) that ranges between a minimal and maximal frequency, respectively, Ω_{\min} and Ω_{\max} . The parameter $\tau > 2$ is adjustable and controls the sharpness of the defined box functions. How to choose these parameters is explained

Algorithm 1: CFE coefficients

Input: Self-energy $\Sigma(z)$

Output: Matrix elements ϵ_n, \mathbf{t}_n

Computation: We use the same subscripts as in main text, but in code, only ϵ_n and \mathbf{t}_n are saved as vectors.

Initialization:

Compute $\Sigma''(\omega) \leftarrow \frac{i}{2\pi} [\Sigma(z) - \Sigma^\dagger(z)]$ and set up $\mathbf{W}(\omega) = \mathbf{t}_1^{-1} \Sigma''(\omega) \mathbf{t}_1^{-1}$, where

$$\mathbf{t}_1 \mathbf{t}_1 = \int d\omega \Sigma''(\omega)$$

Iteration: Perform a N -step Lanczos scheme to set up an orthonormal polynomial basis $\{\mathbf{p}_n^{(1)}(\omega)\}_{n=1,\dots,N}$ with starting polynomial $\mathbf{p}_1^{(1)}(\omega) = \mathbf{1}$:

for $n = 1, \dots, N$

(a) Set $\tilde{\mathbf{p}}_{n+1}^{(1)}(\omega) \leftarrow \omega \mathbf{p}_n^{(1)}(\omega)$

(b) Compute

$$\epsilon_n = \int d\omega \mathbf{p}_n^{(1)\dagger}(\omega) \mathbf{W}(\omega) \tilde{\mathbf{p}}_{n+1}^{(1)}(\omega)$$

(c) Orthogonalize by

$$\begin{aligned} \mathbf{p}_{n+1}^{(1)\perp}(\omega) &\leftarrow \tilde{\mathbf{p}}_{n+1}^{(1)}(\omega) \\ &- \sum_i \mathbf{p}_i^{(1)}(\omega) \int d\omega \mathbf{p}_i^{(1)\dagger}(\omega) \mathbf{W}(\omega) \tilde{\mathbf{p}}_{n+1}^{(1)}(\omega) \end{aligned}$$

(d) Normalize $\mathbf{p}_{n+1}^{(1)}(\omega) = \mathbf{p}_{n+1}^{(1)\perp}(\omega) \mathbf{t}_{n+1}^{-1}$, where

$$\mathbf{t}_{n+1} \mathbf{t}_{n+1} = \int d\omega [\mathbf{p}_{n+1}^{(1)\perp}(\omega)]^\dagger \mathbf{W}(\omega) \mathbf{p}_{n+1}^{(1)\perp}(\omega)$$

Here, steps (c) and (d) should be repeated for improved numerical stability.

end

in detail in App. E 3. Figure 20 depicts $w_n^S(\omega)$ for ten values of n , yielding logarithmically spaced values of Ω_n . The slow/fast splitting strategy yields an exponential decay with n of the modes $\mathbf{R}_n^F(z) \sim \Lambda^{-n}$ and the matrix elements $\epsilon_n \sim \Lambda^{-n}$ and $\mathbf{t}_n \sim \Lambda^{-n}$, as discussed in the main text (cf. Fig. 10).

A pseudocode for our computation of CFE coefficients is given in Alg. 2. At each iteration n the spectral part of the slow modes $\mathbf{R}_n^{S''}(\omega)$ serves as new input function, while the fast modes $\mathbf{R}_n^F(z)$ are kept in the respective CFE step, where their imaginary parts in effect act as scale-dependent broadening functions. The starting point of fast and slow mode splitting can be set at arbitrary n , yielding a general expression for a CFE of the self-energy, where the exponential decay sets in at the corresponding n .

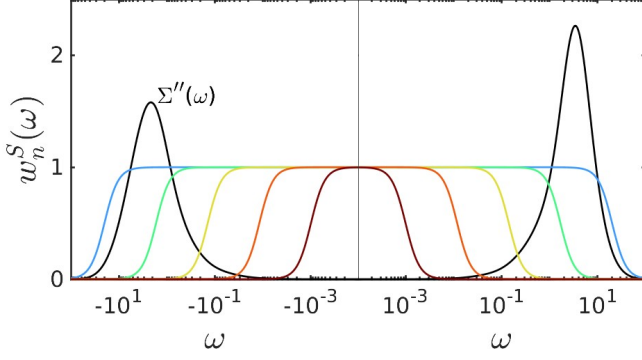


FIG. 20. Exemplary splitting functions $w_n^S(\omega)$ [Eq. (E1)], plotted for $\tau = 3$ and 5 values of n , resulting in logarithmically spaced box widths Ω_n . The black line shows a spectral part of an arbitrary self-energy.

3. Dependency on splitting function $w_n^{S/F}(\omega)$ and CFE length N

The shape of the splitting function $w_n^S(\omega)$ of Eq. (E1) is governed by the two numerical parameters τ and Λ . We now illustrate how the choice of these parameters affects the results obtained from \mathcal{L} -interpolation of DCA data.

a. Sharpness of splitting function

The frequency values of the turning point of the distribution for each CFE step, $\Omega_n \sim \Lambda^{-n}$, are logarithmically spaced between a minimal and a maximal frequency, Ω_{\min} and Ω_{\max} . We set the minimal frequency $\Omega_{\min} = 10^{-9}$ to capture the numerical accuracy of the NRG impurity solver. (For smaller values $\Omega_{\min} \lesssim 10^{-9}$ numerical errors appear at scales below Ω_{\min} , due to reaching machine precision within the computation.) The parameter Ω_{\max} is chosen large enough to capture the full spectral weight of the cluster Green's function $\mathbf{A}(\omega)$:

$$\mathbf{1} - \sum_{|\omega_i| < \Omega_{\max}} \mathbf{A}_{\text{disc}}(\omega_i) < \delta \mathbf{1}, \quad (\text{E2})$$

Here, $\mathbf{A}_{\text{disc}}(\omega_i)$ is the discrete spectral function output of our NRG impurity solver and δ is an accuracy tolerance. We set it to $\delta = 10^{-5}$ for our DCA examples. We cut off over-broadened tails of $w_1^F(\omega)$, thereby regularizing the spectral part of the self-energy, to ensure that the measure $\mathbf{W}(\omega)d\omega$ is not indeterminate.

The parameter $\tau > 2$ controls the sharpness of $w_n^S(\omega)$. It tunes the overlap between successive fast modes and determines the smoothness of the continuous spectrum represented by the resulting CFE. The top row of Fig. 21 illustrates this effect by showing $A_{\mathbf{k}}(0)$ in the pseudogap regime for four values of τ . Correspondingly, Fig. 22(a) displays a frequency slice at momentum $\mathbf{X} = (0, \pi)$ for the same values.

Algorithm 2: CFE with F/S splitting

Input: Self-energy $\Sigma(z)$ and splitting function parameters Ω_{\min} , Ω_{\max} , Λ and τ .

Output: CFE coefficients ϵ_n , \mathbf{t}_n , fast modes $\mathbf{R}_n^F(z)$.

Computation: We use the same subscripts as in main text, but in the code, only ϵ_n , \mathbf{t}_n and \mathbf{R}_n^F are saved as vectors.

Initialization:

CFE length $N = 1 + \ln(\Omega_{\max}/\Omega_{\min})/\ln \Lambda$ and the self-energy spectrum $\Sigma''(\omega) \leftarrow \frac{i}{2\pi} [\Sigma(z) - \Sigma^\dagger(z)]$.

Iteration: Perform N one-step Lanczos schemes: for $n = 1, \dots, N$

(a) Normalize $\Sigma''(\omega)$ to obtain \mathbf{t}_n and \mathbf{W}_{n-1} :

$$\mathbf{t}_n \mathbf{t}_n = \int d\omega \Sigma''(\omega),$$

$$\mathbf{W}_{n-1}(\omega) \leftarrow \mathbf{t}_n^{-1} \Sigma''(\omega) \mathbf{t}_n^{-1}.$$

(b) Compute $\epsilon_n = \int d\omega \mathbf{W}_{n-1}(\omega) \omega$

(c) Compute $\mathbf{R}_n(\omega)$ via Eqs. (43):

$$\mathbf{G}_2(z) \leftarrow \int d\omega \frac{\mathbf{W}_{n-1}(\omega)}{z - \omega}$$

$$\tilde{\mathbf{F}}_2^L(z) \leftarrow \int d\omega (\omega \mathbf{1} - \epsilon_n) \frac{\mathbf{W}_{n-1}(\omega)}{z - \omega}$$

$$\tilde{\mathbf{F}}_2^R(z) \leftarrow \int d\omega \frac{\mathbf{W}_{n-1}(\omega)}{z - \omega} (\omega \mathbf{1} - \epsilon_n)$$

$$\tilde{\mathbf{I}}_2(z) \leftarrow \int d\omega (\omega \mathbf{1} - \epsilon_n) \frac{\mathbf{W}_{n-1}(\omega)}{z - \omega} (\omega \mathbf{1} - \epsilon_n)$$

$$\mathbf{R}_n(z) \leftarrow \tilde{\mathbf{I}}_2(z) - \tilde{\mathbf{F}}_2^L(z) [\mathbf{G}_2(z)]^{-1} \tilde{\mathbf{F}}_2^R(z)$$

(d) Define splitting functions: $\Omega_n = \Omega_{\max} \Lambda^{1-n}$, $w_n^S(\omega) \leftarrow (1 + |\omega/\Omega_n|^\tau)^{-1}$, $w_n^F(\omega) \leftarrow 1 - w_n^S(\omega)$.

Split $\mathbf{R}_n(z)$, reset $\Sigma''(\omega)$ for next iteration:

$$\mathbf{R}_n''(\omega) \leftarrow \frac{i}{2\pi} [\mathbf{R}_n(z) - \mathbf{R}_n^\dagger(z)]$$

$$\mathbf{R}_n^F(z) = \int d\omega \frac{w_n^F(\omega) \mathbf{R}_n''(\omega)}{z - \omega}$$

$$\Sigma''(\omega) \leftarrow w_n^S(\omega) \mathbf{R}_n''(\omega)$$

For the last step N , don't split $\mathbf{R}_n(z)$.

end

The impact of decreasing τ is clearly visible: while $\tau = 10$ yields a slightly underbroadened interpolation, reducing τ gradually removes the wiggles and, at the same time, sharpens the main features. However, for τ too small (e.g. $\tau \simeq 2$), the fast modes retain significant weight at low frequencies and the slow modes retain substantial high-frequency tails, i.e. $\mathbf{R}_n^{F''}(\omega)$ and $\mathbf{R}_n^{S''}(\omega)$ overlap significantly and don't achieve a clean scale separation between fast and slow modes. We find that this causes them to also retain a strong \mathbf{k} -dependence. This is undesirable, since Liouvillian interpolation works best if the \mathbf{k} -dependence is encoded entirely (or as much as possible) in the Liouvillian matrix elements ϵ_n and \mathbf{t}_n . For

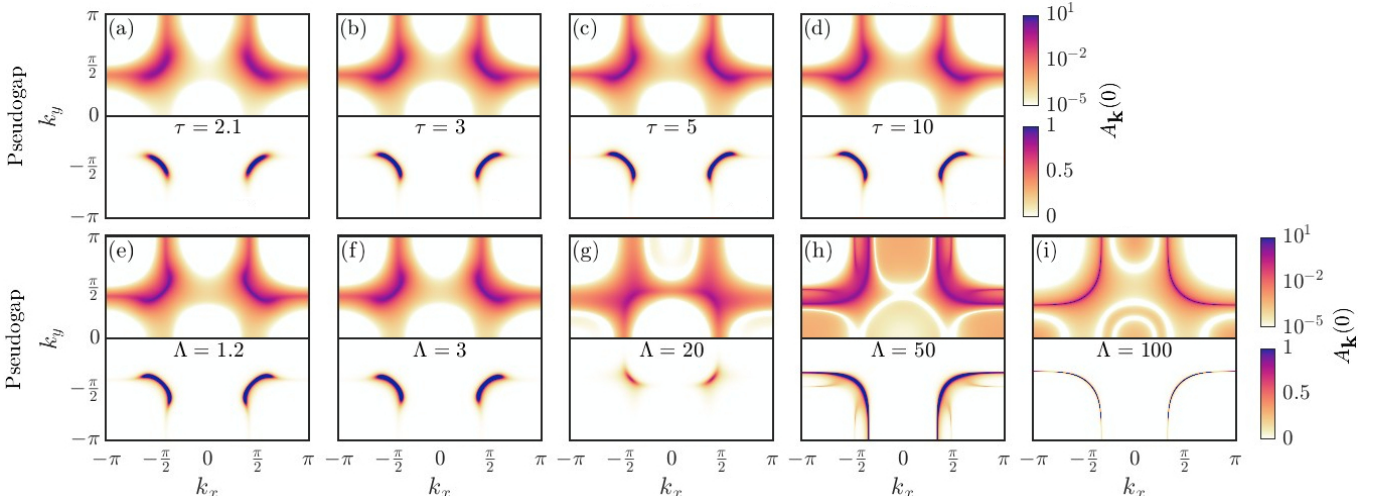


FIG. 21. \mathcal{L} -interpolated DCA results for $A_{\mathbf{k}}(0)$ in the pseudogap phase, computed for the same model parameters as in Fig. 12, shown (a-d) for four values of the parameter τ in Eq. (E1), with $\Lambda = 1.2$ throughout, and (e-i) for five values of the parameter Λ in Eq. (E1), with $\tau = 5$ throughout. The top and bottom rows of each panel show the upper and lower halves of the BZ using logarithmic and linear color scales, respectively.

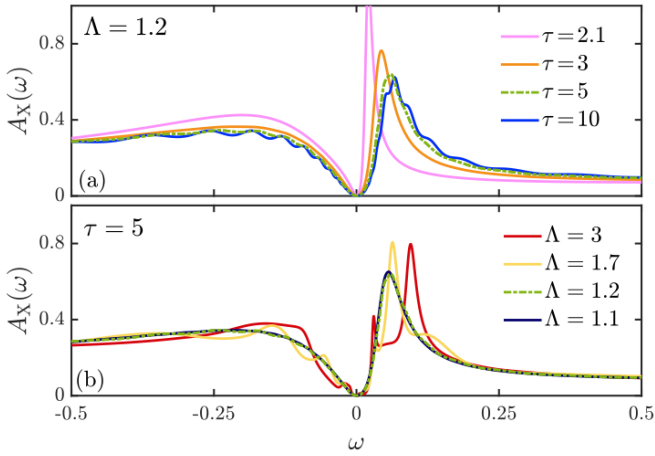


FIG. 22. Spectral function as function of ω at $\mathbf{k} = \mathbf{X} = (0, \pi)$, (a) for the four values of τ used for Figs. 21(a-d), and (b) for four values of Λ in the range used for Figs. 21(e-f) or smaller.

$\tau \leq 2$, we even observe a breakdown of tail regularization: sufficient weight remains in the tails after splitting such that $\epsilon_n \approx \Lambda^{-n}$, $\mathbf{t}_n \approx \Lambda^{-n}$, and $\mathbf{R}_n^F(z) \approx \Lambda^{-n}$.

Conversely, increasing τ reduces the fast-mode overlap, yielding cleaner scale separation and a more stable interpolation. However, a too large τ leads to underbroadening, exemplified by the wiggles in the $\tau = 10$ curve of Fig. 22(a). The optimal choice of τ is therefore the largest value at which, upon decreasing τ , these wiggles have just disappeared. We therefore choose $\tau = 5$.

b. CFE length with rest function

Due to the exponential decrease $\Omega_n \sim \Lambda^{-n}$ with n , the quantities ϵ_n , \mathbf{t}_n , and $\mathbf{R}_n^F(z)$ also decay exponentially and eventually reach the scale of numerical floating-point errors. As a result, the CFE exhibits artificial convergence. Increasing the CFE length N , or equivalently decreasing the logarithmic discretization factor Λ (while keeping $\Lambda > 1$), increases the number of matrix elements in the CFE representation.

The second row of Fig. 21 shows \mathcal{L} -interpolated results for $A_{\mathbf{k}}(0)$ in the pseudogap regime for several values of Λ , where panels (e)–(i) correspond to a progressively shorter CFE. Figure Fig. 22(b) presents a frequency slice at momentum $\mathbf{X} = (0, \pi)$ for four values with $\Lambda \leq 3$. Smaller Λ increases the number of Liouvillian matrix elements and thus the number of bands contributing to the interpolated spectrum. Encoding the \mathbf{k} -dependence through more matrix elements improves the interpolation of a continuous spectrum.

Comparing the lower row of Fig. 21 with Fig. 22(b) shows that the low-energy regime converges more rapidly ($\Lambda \lesssim 3$) than the high-energy regime as Λ decreases, reflecting the logarithmic discretization. Accurately resolving high-energy features requires a higher matrix element density, i.e., even smaller Λ . In our calculations, convergence at high energies is achieved for $\Lambda \lesssim 1.2$, as shown in Fig. 22(b).

Since we interpolate the fast modes using $\alpha_{\mathbf{k}, \mathbf{K}}$ (not $\alpha_{\mathbf{k}, \mathbf{K}}^{\text{mod}}$), causality issues begin to arise for $\Lambda \gtrsim 3$, foreshadowing the fact that in the limit $\Lambda \gg 1$, \mathbf{R}_n^F -interpolation has similar issues as Σ -interpolation. This behavior originates from the enhanced \mathbf{k} -dependence of the fast modes when fewer matrix elements are retained. We therefore choose $\Lambda = 1.2$ as a good compromise between a man-

ageable log-CFE depth and an accurate representation of the $\Lambda \rightarrow 1$ limit. Note that decreasing Λ allows for larger values of τ while maintaining numerical stability.

Appendix F: Lattice harmonics

This appendix gives some background on lattice harmonics and their symmetry properties [100, 101], evoked in Sec. III B on canonical DCA interpolation.

Lattice harmonics are functions of \mathbf{k} that transform according to irreducible representations (irreps) of the symmetry point group, say G , of the model's real-space Bravais lattice and its BZ. (For a symmetry-broken phase, let G describe the remaining symmetry.) Let Γ be an irrep of G , with dimension d_Γ and matrix representation D^Γ . Lattice harmonics forming a \mathbf{k} -space basis for Γ can be constructed by projecting the plane wave function $e^{-i\mathbf{k}\cdot\mathbf{r}}$, for some fixed seed vector \mathbf{r} from the real-space lattice, onto Γ using the standard group-theory projector:

$$[\phi_{\mathbf{k}}^\Gamma]_\alpha = \frac{d_\Gamma}{|G|} \sum_{g \in G} [D^\Gamma(g)]_{\alpha 1} e^{-i\mathbf{k}\cdot g(\mathbf{r})}. \quad (\text{F1})$$

The D^Γ matrices can always be chosen such that the resulting functions $[\phi_{\mathbf{k}}^\Gamma]_\alpha$ are real, and we assume this to be the case in this work. For $\mathbf{r} = \mathbf{0}$, Eq. (F1) yields a \mathbf{k} -independent function; for seed vectors of increasing length $|\mathbf{r}|$, it yields lattice harmonics with an increasingly complex dependence on \mathbf{k} .

Consider, for example, a 2-dimensional square lattice, invariant under $G = C_{4v}$, the group of reflections about the x - and y -axes and of multiples-of- $\pi/2$ rotations about the origin. Then, the lattice harmonics obtained for seed vectors with $|\mathbf{r}| = 1$ are linear combinations of cosine and sine functions, and those obtained for $|\mathbf{r}| > 1$ can include nonlinear combinations of cosine and sine functions.

For a given DCA patching scheme, let G_p be that subgroup of G which leaves every patch individually invariant, i.e. for every patch $V_{\mathbf{K}}$, if $\mathbf{k} \in V_{\mathbf{K}}$ then $g(\mathbf{k}) \in V_{\mathbf{K}}$ for all $g \in G_p$. A subset of all lattice harmonics of G are invariant under G_p (i.e. transform trivially under G_p). In the main text (Sec. III B), we denote them by $\phi_{\mathbf{k},j}$, where $j = 1, 2, 3, \dots$ enumerates them in order of increasing complexity, with $\phi_{\mathbf{k},1} = 1$. By definition, these functions obey $\phi_{g(\mathbf{k}),j} = \phi_{\mathbf{k},j}$ for all $g \in G_p$.

In Sec. V of the main text, we consider a 2-dimensional square lattice with point group symmetry C_{4v} , and a DCA scheme with $N_p = 4$ patches arranged in a star geometry, see Fig. 8. These patches are invariant under $G_p = C_{2v}$, the group of reflections about the x - and y -axes (but not under $\pi/2$ rotations about the origin). Since C_{4v} contains C_{2v} as a subgroup, all C_{4v} irreps are also C_{2v} irreps, and since C_{2v} is abelian, all its irreps are one-dimensional. This means that *all* C_{4v} irreps transform trivially under C_{2v} . We therefore simply choose the $\phi_{\mathbf{k},j}$ functions to be the first N_p irreps of C_{4v} , enumerated

in order of increasing complexity:

$$\begin{aligned} \phi_{\mathbf{k},1} &= 1, & \phi_{\mathbf{k},3} &= \cos k_x - \cos k_y, \\ \phi_{\mathbf{k},2} &= \cos k_x + \cos k_y, & \phi_{\mathbf{k},4} &= \cos k_x \cos k_y. \end{aligned} \quad (\text{F2})$$

Remark: These functions are linearly related to the lattice harmonics of the patch-symmetry group $G_p = C_{2v}$,

$$\begin{aligned} \phi'_{\mathbf{k},1} &= 1, & \phi'_{\mathbf{k},3} &= \cos k_y, \\ \phi'_{\mathbf{k},2} &= \cos k_x, & \phi'_{\mathbf{k},4} &= \cos k_x \cos k_y. \end{aligned} \quad (\text{F3})$$

These follow from a version of Eq. (F1) appropriate for abelian groups,

$$\phi'_{\mathbf{k},j} = \frac{1}{|G_p|} \sum_{g \in G_p} e^{-i\mathbf{k}\cdot g(\mathbf{r}_j)} = \frac{1}{N_j} \sum_{\mathbf{r} \in O_j} e^{-i\mathbf{k}\cdot\mathbf{r}}, \quad (\text{F4})$$

seeded by $\mathbf{r}_1 = (0, 0)$, $\mathbf{r}_2 = (1, 0)$, $\mathbf{r}_3 = (0, 1)$, $\mathbf{r}_4 = (1, 1)$. On the right, the sum is over all points in the orbit O_j seeded by \mathbf{r}_j , i.e. the set of distinct points obtained by acting with all elements of G_p on \mathbf{r}_j , and N_j is the number of points in orbit O_j (here: $N_1 = 1$, $N_2 = N_3 = 2$, $N_4 = 4$). We regard N_j as a measure of the non-locality of the Fourier modes contributing to $\phi'_{\mathbf{k},j}$ and $\phi_{\mathbf{k},j}$. The modified form factors $\alpha_{\mathbf{k},\mathbf{K}}^{\text{mod}}$ of Eq. (65) aim to ameliorate non-causality issues by reducing the weight of these non-local Fourier modes by an extra factor $1/N_j$.

To conclude this appendix, we remark that the interpolation Ansatz of Eqs. (58) and (59) for $\mathbf{Q}_{\mathbf{k}}(z)$ and $\alpha_{\mathbf{k},\mathbf{K}}$ can be expressed as a truncated Fourier expansion of the form of Eq. (2): by Eq. (F1), lattice harmonics are symmetry projections of Fourier factors $e^{-i\mathbf{k}\cdot\mathbf{r}}$, and those used for $\phi_{\mathbf{k},j \leq N_p}$ are lattice harmonics of low complexity, for which $|\mathbf{r}|$ is of limited range, say $|\mathbf{r}| \leq R$.

Appendix G: Pseudogap of cellular DMFT+ED

In this appendix we perform another test of \mathcal{L} -interpolation, based on CDMFT+ED results for the pseudogap phase in the 2D Hubbard model. These results were kindly provided to us by the authors of Ref. 33. Their results were computed for $t = 1$, $t' = -0.3t$, $t'' = 0.2t$, $U = 8t$ and a doping level of $x = 0.065$, and include broadening with $\eta = 0.1$. For further details regarding the numerical methodology, we refer the reader to Refs. [33, 102].

The rationale for testing the \mathcal{L} -scheme with an exact diagonalization (ED) impurity solver stems from the discrete nature of the pole spectrum produced by this method. Since the spectrum is both finite and discrete, the continued fraction expansion (CFE) is likewise finite, with its length dictated by the number of poles, thereby eliminating the necessity for a rest function.

We start from CDMFT+ED results for the discrete spectrum of the impurity Green's function $\mathbf{G}_{\text{dd}}(z)$, computed for a given hybridization function $\mathbf{\Delta}(z)$ having a discrete spectrum of $\mathbf{\Delta}(z)$ of the form

$$\mathbf{\Delta}''(\omega) = \sum_{\ell} \mathbf{\Delta}_{\ell} \delta(\omega - \xi_{\ell}). \quad (\text{G1})$$

To we extract the discrete spectrum of the self-energy $\Sigma(z)$ we first invert the Dyson equation (cf. Eq. (48)),

$$\mathbf{G}_{\text{dd}}(z) = \frac{1}{z - \epsilon - \mathbf{\Delta}(z) - \mathbf{\Sigma}(z)}, \quad (\text{G2})$$

using a strategy explained in Ref. 60. This provides us with the spectrum of $\mathbf{\Delta}(z) + \mathbf{\Sigma}(z)$, obtained in the form

$$\mathbf{\Delta}''(\omega) + \mathbf{\Sigma}''(\omega) = \sum_i [\mathbf{\Delta} + \mathbf{\Sigma}]_i \delta(\omega - \tilde{\omega}_i). \quad (\text{G3})$$

We then extract $\mathbf{\Sigma}''(\omega)$ from Eq. (G3) by subtracting $\mathbf{\Delta}''(z)$ via the pole-subtraction strategy of Ref. 103: we identify matching energies ξ_ℓ and $\tilde{\omega}_\ell$ (for every ξ_ℓ , we always found a unique $\tilde{\omega}_\ell$ with $|\xi_\ell - \tilde{\omega}_\ell| < 10^{-8}$), and subtract the corresponding $\mathbf{\Delta}_\ell$ to obtain

$$\mathbf{\Sigma}_\ell = \begin{cases} [\mathbf{\Delta} + \mathbf{\Sigma}]_\ell - \mathbf{\Delta}_\ell & \text{if } \exists \xi_\ell : |\xi_\ell - \tilde{\omega}_\ell| < \varepsilon \\ [\mathbf{\Delta} + \mathbf{\Sigma}]_\ell & \text{otherwise.} \end{cases} \quad (\text{G4})$$

We found $\mathbf{\Sigma}_\ell \simeq 0$ whenever $|\xi_\ell - \tilde{\omega}_\ell| < \varepsilon$, signifying a clean subtraction of the hybridization function poles.

Let us now compare the results of applying M - and \mathcal{L} -interpolation to this data. For M -interpolation we broaden the self-energy using Gaussian broadening (with standard deviation $\sigma = 0.15$) and compute the cumulant from the Gaussian broadened the self-energy spectrum. For \mathcal{L} -interpolation we construct the CFE (41) of the discrete self-energy represented by $\{\mathbf{\Sigma}_\ell, \omega_\ell\}$, periodize the resulting ω -independent Liouvillian matrix elements, and broaden the reconstructed $\mathbf{\Sigma}_\mathbf{k}(\omega_\ell)$ for individual \mathbf{k} -points using CFE+Gaussian broadening (following Ref. 64, Sec. S-2.2).

In Figure 23, we present the comparison between the \mathcal{L} -scheme and the M -scheme for the spectral function $A_\mathbf{k}(\omega = 0)$. The left panel corresponds to the M -scheme, while the right panel shows the \mathcal{L} -scheme results.

The M -interpolation produces a hole-like Fermi surface, however, the spectral weight decays strongly towards the BZ boundary. In contrast, the \mathcal{L} -scheme unveils a more refined structure: rather than arcs, it reveals an intersected arc suggestive of a hole pocket. This result highlights the \mathcal{L} -scheme's ability to capture finer details of the Fermi surface, including potential hole pockets that may be overlooked by other interpolation methods.

The second row of Fig. 23 shows the spectral function $A_\mathbf{k}(\omega)$ along the path $\Gamma\text{XMI}\Gamma$ in the BZ, corresponding to the first row. The \mathcal{L} -interpolation produces a clear gap at X and $\omega = 0$ compared to M -interpolation. These plots highlight how the individual CFE bands accumulate, ultimately approximating the full spectral band. The cuts in band structure are attributed to finite size effects of the ED impurity solver and missing poles. This results in a resolution of the jagged ED structure within the interpolation even with a relatively large broadening. Even though we are able to resolve hole pockets, the finite size effects of make it hard to decipher if this structure is the correct one.

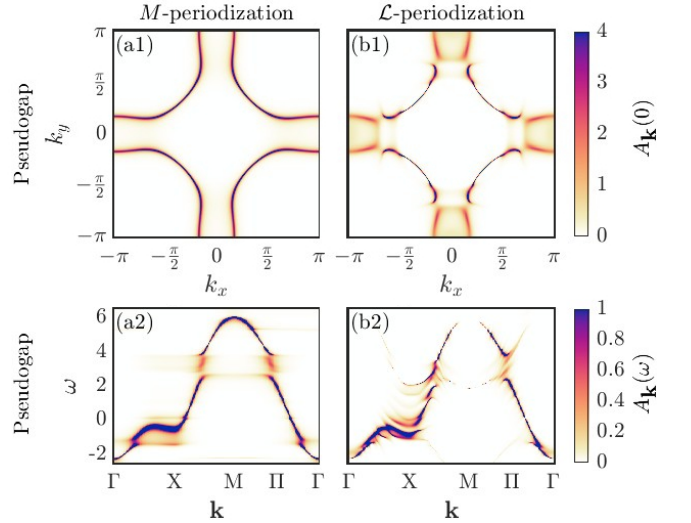


FIG. 23. Interpolated CDMFT+ED results for a 4-site cluster impurity with $t = 1$, $t' = -0.3t$, $t'' = 0.2t$, and $U = 8t$, in the pseudogap phase at doping $\delta = 0.065$. (a1,b1) The spectral function at the Fermi surface, $A_\mathbf{k}(\omega = 0)$, and (a2,b2) the spectral function along the path $\Gamma\text{XMI}\Gamma$, $A_\mathbf{k}(\omega)$ obtained via (a) M - and (b) \mathcal{L} -periodization.

Although the \mathcal{L} -scheme successfully resolves the hole pocket-like structure, it remains uncertain whether this feature is fully accurate due to the finite size effects inherent in ED. Nevertheless, these results suggest that the \mathcal{L} -scheme provides a more detailed and potentially more accurate interpolation of the spectral function compared to the M -scheme.

Appendix H: Details on TaSK calculations

The MPS results on the 1D Hubbard model presented in Sec. IV A were obtained using the tangent space Krylov (TaSK) scheme recently proposed in Ref. 64. The CDMFT results of Sec. IV B were obtained by applying TaSK to impurity models, following Ref. 104. Here, we discuss some aspects specific to our present TaSK computations that are not discussed those two references.

1. Hubbard chain

We consider a 1D Hubbard chain of $L = 50$ sites, with $U = 5$ and $\mu = -U/2$ (half-filling). To compute the spectral function $A_k(\omega)$ of the correlator $G_k(t)$ of Eq. (73), we use the k -dependent single-particle operator

$$c_k = \frac{1}{\sqrt{L}} \sum_{\ell=1}^L e^{-ik\ell} c_\ell, \quad (\text{H1})$$

where we treat k as a continuous variable to achieve finer k resolution. We exploit $U(1) \times SU(2)$ charge and spin

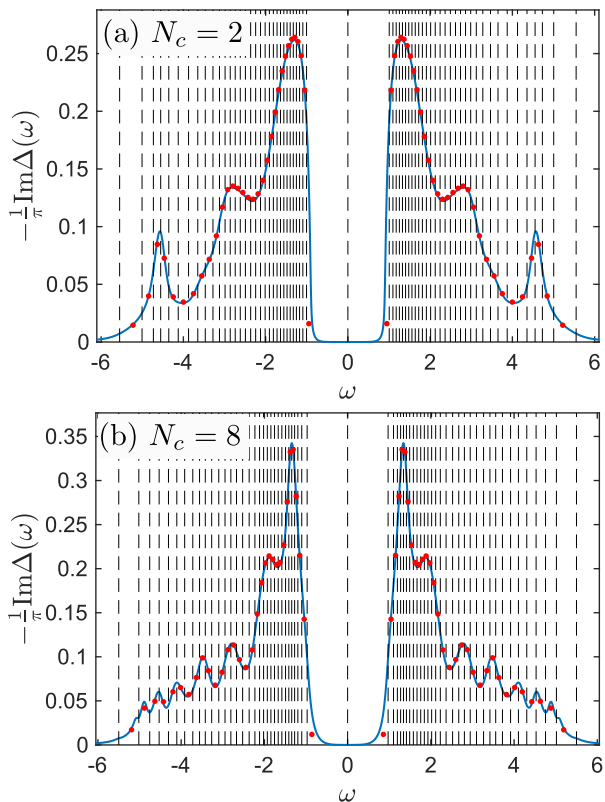


FIG. 24. Hybridization functions (blue lines) at self-consistency for (a) $N_c = 2$ and (b) $N_c = 8$. The black dashed lines mark the boundaries between the 64 frequency intervals used for discretization. The discretized hybridization function is plotted as red dots. Their ω positions are the frequency of the delta peaks, their height is the weight of the delta peak normalized by the size of the corresponding frequency interval.

symmetries. We compute the ground state using state-of-the-art single-site DMRG [105, 106] with bond expansion [107–109]. The bond dimension of our ground state is $D^* = 500$ SU(2) multiplets.

We choose 51 equally spaced values for k between 0 and π , and for each momentum point use TaSK to compute a discrete version, $A_k^{\text{disc}}(\omega)$, of the spectral function, comprising 204 discrete δ -peaks. We then compute the CFE coefficients ϵ_{kn} and t_{kn} (shown in Fig. 3) from $A_k^{\text{disc}}(\omega)$ (known at 51 k -values). To obtain a spectrum for arbitrary k , we interpolate $A_k^{\text{disc}}(\omega)$ for k -values between our chosen 51 ones by linear interpolation of the CFE coefficients ϵ_{kn} and t_{kn} . To obtain the continuous-in-frequency spectra shown in Fig. 1(a), we use the CFE+Gaussian broadening scheme of Sec. S-2 of Ref. [64], with broadening parameter $\sigma = 0.3$ and $\mathcal{N}_{\text{CFE}} = 2$ there. For the lattice model, this is equivalent to broadening the discrete self-energy with $\sigma = 0.3$ and $\mathcal{N}_{\text{CFE}} = 1$.

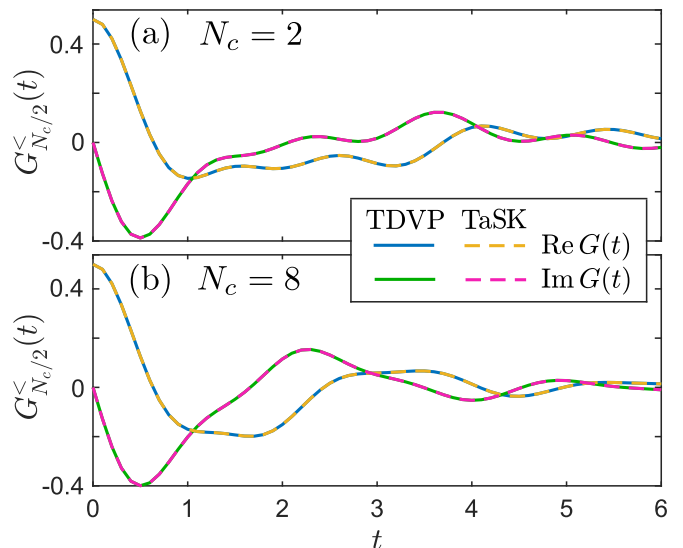


FIG. 25. Lesser Green's function $G_{N_c/2}^<(t)$ computed via TDVP (solid lines) and TaSK (dashed lines) for (a) $N_c = 2$ and (b) $N_c = 8$. For TDVP, we have used a time step $\delta t = 0.1$ and a third-order integrator; the bond dimension is allowed to grow to ensure a numerically exact result. With TaSK, we compute the spectrum of $G_{N_c/2}^<(t)$ and Fourier transform to the time domain.

2. Impurity solver for cellular DMFT

In Sec. IV B, we presented CDMFT results for the 1d Hubbard model. (For details on CDMFT for the 1d Hubbard model, see for instance Ref. [110].) The impurity solver we employ for this purpose closely follows the implementation presented in Ref. 104. The impurity model consists of an N_c -site Hubbard chain, whose outermost sites hybridize with left and right spinful baths described by two identical hybridization functions $\Delta_L(\omega) = \Delta_R(\omega)$. In contrast to Ref. 104, we discretize our baths using a linear grid generated via the mean method of Ref. 65. For the data shown in this manuscript, we use 64 spinful orbitals per bath. The discretization intervals, level positions and hybridization weights at self-consistency are illustrated in Fig. 24 for $N_c = 2$ and $N_c = 8$. Each of the discretized baths is mapped to the chain geometry depicted in Fig.2 (b) of Ref. [111]. Since only the boundary sites of the cluster couple to the bath, we arrange our system such that the 64 left-most sites belong to the bath coupling to the left-most cluster orbital, followed by the N_c cluster sites and finally the 64 bath sites that belong to the bath hybridizing with the right-most cluster site. Again, we compute the ground state using single-site DMRG with bond expansion [108]. For the impurity solver, we truncate by singular values, using a truncation threshold of 2×10^{-8} . We then compute the discrete self-energy ($N_c \times N_c$ matrix valued) of this impurity model using a strategy described in Ref. [60]. The spectral functions necessary for that are calculated using TaSK, see Ref. 104 for specifics about using TaSK for

impurity models. Within the self-consistency cycle, the self-energy is then broadened using the CFE+Gaussian scheme of Ref. [64], using $\sigma = 0.3$ and $\mathcal{N}_{\text{CFE}} = 1$.

To gauge whether TaSK provides accurate impurity spectral functions for the impurity model at hand we also conduct an independent benchmark test, formulated in the time domain. We use the single-site time-dependent variational principle (TDVP) [112] with bond expansion [113] to compute the lesser Green's function,

$$G_{N_c/2}^<(t) = \langle \Psi_0 | c_{N_c/2\sigma}^\dagger e^{i(H-E_0)t} c_{N_c/2\sigma} | \Psi \rangle \quad (\text{H2})$$

for short times. Here, $c_{N_c/2\sigma}$ is the spin- σ annihilation operator at cluster site $N_c/2$, $|\Psi_0\rangle$ the ground state and E_0 its energy. We then compare the TDVP result for $G_{N_c/2}^<(t)$ with the TaSK result, which can be easily computed from the discrete spectra. The result of this comparison is shown in Fig. 25, for $N_c = 4, 8$. The time-dependent data obtained from both methods agree very well, which shows that our TaSK spectra are reliable.

-
- [1] T. Maier, M. Jarrell, T. Pruschke, and M. H. Hettler, Quantum cluster theories, *Rev. Mod. Phys.* **77**, 1027 (2005).
- [2] G. Kotliar, S. Y. Savrasov, G. Pálsson, and G. Biroli, Cellular dynamical mean field approach to strongly correlated systems, *Phys. Rev. Lett.* **87**, 186401 (2001).
- [3] M. H. Hettler, A. N. Tahvildar-Zadeh, M. Jarrell, T. Pruschke, and H. R. Krishnamurthy, Nonlocal dynamical correlations of strongly interacting electron systems, *Phys. Rev. B* **58**, R7475 (1998).
- [4] M. H. Hettler, M. Mukherjee, M. Jarrell, and H. R. Krishnamurthy, Dynamical cluster approximation: Nonlocal dynamics of correlated electron systems, *Phys. Rev. B* **61**, 12739 (2000).
- [5] T. A. Maier, T. Pruschke, and M. Jarrell, Angle-resolved photoemission spectra of the hubbard model, *Phys. Rev. B* **66**, 075102 (2002).
- [6] P. Staar, T. Maier, and T. C. Schulthess, Dynamical cluster approximation with continuous lattice self-energy, *Phys. Rev. B* **88**, 115101 (2013).
- [7] U. R. Hähner, T. A. Maier, and T. C. Schulthess, Continuous momentum dependence in the dynamical cluster approximation, *Phys. Rev. B* **101**, 195114 (2020).
- [8] D. Sénéchal, D. Perez, and D. Plouffe, Cluster perturbation theory for Hubbard models, *Phys. Rev. B* **66**, 075129 (2002).
- [9] G. Biroli and G. Kotliar, Cluster methods for strongly correlated electron systems, *Phys. Rev. B* **65**, 155112 (2002).
- [10] G. Biroli, O. Parcollet, and G. Kotliar, Cluster dynamical mean-field theories: Causality and classical limit, *Phys. Rev. B* **69**, 205108 (2004).
- [11] T. D. Stanescu and G. Kotliar, Fermi arcs and hidden zeros of the Green function in the pseudogap state, *Phys. Rev. B* **74**, 125110 (2006).
- [12] S. Sakai, G. Sangiovanni, M. Civelli, Y. Motome, K. Held, and M. Imada, Cluster-size dependence in cellular dynamical mean-field theory, *Phys. Rev. B* **85**, 035102 (2012).
- [13] S. Verret, J. Roy, A. Foley, M. Charlebois, D. Sénéchal, and A.-M. S. Tremblay, Intrinsic cluster-shaped density waves in cellular dynamical mean-field theory, *Phys. Rev. B* **100**, 224520 (2019).
- [14] M. Potthoff, Cluster extensions of dynamical mean-field theory, in *DMFT: From Infinite Dimensions to Real Materials Modeling and Simulation*, *Forschungszentrum Jülich*, edited by E. Pavarini, E. Koch, D. Vollhardt, and A. Lichtenstein (2018).
- [15] A. Georges, G. Kotliar, W. Krauth, and M. J. Rozenberg, Dynamical mean-field theory of strongly correlated fermion systems and the limit of infinite dimensions, *Rev. Mod. Phys.* **68**, 13 (1996).
- [16] S. Sakai, S. Blanc, M. Civelli, Y. Gallais, M. Cazayous, M.-A. Méasson, J. S. Wen, Z. J. Xu, G. D. Gu, G. Sangiovanni, Y. Motome, K. Held, A. Sacuto, A. Georges, and M. Imada, Raman-scattering measurements and theory of the energy-momentum spectrum for underdoped $\text{Bi}_2\text{Sr}_2\text{CaCuO}_{8+\delta}$ superconductors: Evidence of an s -wave structure for the pseudogap, *Phys. Rev. Lett.* **111**, 107001 (2013).
- [17] S. Sakai, Y. Motome, and M. Imada, Evolution of electronic structure of doped Mott insulators: Reconstruction of poles and zeros of Green's function, *Phys. Rev. Lett.* **102**, 056404 (2009).
- [18] S. Sakai, Y. Motome, and M. Imada, Doped high- T_c cuprate superconductors elucidated in the light of zeros and poles of the electronic Green's function, *Phys. Rev. B* **82**, 134505 (2010).
- [19] F. Krien, P. Worm, P. Chalupa-Gantner, *et al.*, Explaining the pseudogap through damping and antidamping on the Fermi surface by imaginary spin scattering, *Commun. Phys.* **5**, 336 (2022).
- [20] C. Walsh, M. Charlebois, P. Sémon, A.-M. S. Tremblay, and G. Sordi, Superconductivity in the two-dimensional Hubbard model with cellular dynamical mean-field theory: A quantum impurity model analysis, *Phys. Rev. B* **108**, 075163 (2023).
- [21] L. De Leo, M. Civelli, and G. Kotliar, Cellular dynamical mean-field theory of the periodic Anderson model, *Phys. Rev. B* **77**, 075107 (2008).
- [22] L. De Leo, M. Civelli, and G. Kotliar, $T = 0$ heavy-fermion quantum critical point as an orbital-selective Mott transition, *Phys. Rev. Lett.* **101**, 256404 (2008).
- [23] A. Gleis, S.-S. B. Lee, G. Kotliar, and J. von Delft, Emergent properties of the periodic Anderson model: A high-resolution, real-frequency study of heavy-fermion quantum criticality, *Phys. Rev. X* **14**, 041036 (2024).
- [24] W. Wú, X. Wang, and A.-M. Tremblay, Non-Fermi liquid phase and linear-in-temperature scattering rate in overdoped two-dimensional Hubbard model, *Proceedings of the National Academy of Sciences* **119** (2022).
- [25] J. Fournier, P.-O. Downey, C.-D. Hébert, M. Charlebois, and A.-M. Tremblay, Two T -linear scattering-rate regimes in the triangular lattice Hubbard model, *Sci-*

- Post Physics **17** (2024).
- [26] A. Gleis, S.-S. B. Lee, G. Kotliar, and J. von Delft, Dynamical scaling and Planckian dissipation due to heavy-fermion quantum criticality, *Phys. Rev. Lett.* **134**, 106501 (2025).
- [27] A. Hardy, O. Parcollet, A. Georges, and A. A. Patel, Enhanced strange metallicity due to Hubbard- U Coulomb repulsion, *Phys. Rev. Lett.* **134**, 036502 (2025).
- [28] Y. Nomura, S. Sakai, and R. Arita, Nonlocal correlations induced by Hund's coupling: A cluster DMFT study, *Phys. Rev. B* **91** (2015).
- [29] P. Sémon, K. Haule, and G. Kotliar, Validity of the local approximation in iron pnictides and chalcogenides, *Phys. Rev. B* **95**, 195115 (2017).
- [30] Y. Nomura, S. Sakai, and R. Arita, Multiorbital cluster dynamical mean-field theory with an improved continuous-time quantum Monte Carlo algorithm, *Phys. Rev. B* **89**, 195146 (2014).
- [31] M. Harland, A. I. Poteryaev, S. V. Streltsov, and A. I. Lichtenstein, Electronic correlations and competing orders in multiorbital dimers: A cluster DMFT study, *Phys. Rev. B* **99**, 045115 (2019).
- [32] M. Klett, N. Wentzell, T. Schäfer, F. Simkovic, O. Parcollet, S. Andergassen, and P. Hansmann, Real-space cluster dynamical mean-field theory: Center-focused extrapolation on the one- and two particle-levels, *Phys. Rev. Res.* **2**, 033476 (2020).
- [33] S. Verret, A. Foley, D. Sénéchal, A.-M. S. Tremblay, and M. Charlebois, Fermi arcs versus hole pockets: Periodization of a cellular two-band model, *Phys. Rev. B* **105**, 035117 (2022).
- [34] T. Das, R. S. Markiewicz, A. Bansil, and A. V. Balatsky, Visualizing electron pockets in cuprate superconductors, *Phys. Rev. B* **85**, 224535 (2012).
- [35] Y. Li, W. Tabis, Y. Tang, G. Yu, J. Jaroszynski, N. Barišić, and M. Greven, Hole pocket-driven superconductivity and its universal features in the electron-doped cuprates, *Science Advances* **5**, eaap7349 (2019).
- [36] A. Damascelli, Z. Hussain, and Z.-X. Shen, Angle-resolved photoemission studies of the cuprate superconductors, *Rev. Mod. Phys.* **75**, 473 (2003).
- [37] T. Reber, N. Plumb, Z. Sun, T. J. Reber, N. C. Plumb, Z. Sun, Q. Cao, Y. nd Wang, K. McElroy, H. Iwasawa, . Arita, J. S. Wen, Z. J. Xu, G. Gu, . Yoshida, H. Eisaki, Y. Aiura, and D. S. Dessau, The origin and non-quasiparticle nature of Fermi arcs in $\text{Bi}_2\text{Sr}_2\text{CaCu}_2\text{O}_{8+\delta}$, *Nature Phys.* **8**, 606 (2012).
- [38] T. D. Stanescu, M. Civelli, K. Haule, and G. Kotliar, A cellular dynamical mean field theory approach to Mottness, *Ann. Phys.* **321**, 1682 (2006), special Issue.
- [39] K.-Y. Yang, T. M. Rice, and F.-C. Zhang, Phenomenological theory of the pseudogap state, *Phys. Rev. B* **73**, 174501 (2006).
- [40] H. Mori, A continued-fraction representation of the time-correlation functions, *Progress of Theoretical Physics* **34**, 399 (1965).
- [41] R. Haydock, The recursive solution to the Schrodinger equation, *Solid state physics* **35**, 215.
- [42] V. S. Viswanath and G. Müller, *The Recursion Method* (Springer Berlin, Heidelberg, 1994).
- [43] P. E. Dargel, A. Honecker, R. Peters, R. M. Noack, and T. Pruschke, Adaptive Lanczos-vector method for dynamic properties within the density matrix renormalization group, *Phys. Rev. B* **83**, 161104 (2011).
- [44] P. E. Dargel, A. Wöllert, A. Honecker, I. P. McCulloch, U. Schollwöck, and T. Pruschke, Lanczos algorithm with matrix product states for dynamical correlation functions, *Phys. Rev. B* **85**, 205119 (2012).
- [45] A. C. Tiegel, S. R. Manmana, T. Pruschke, and A. Honecker, Matrix product state formulation of frequency-space dynamics at finite temperatures, *Phys. Rev. B* **90**, 060406 (2014).
- [46] J.-P. Julien and R. C. Albers, Extended recursion in operator space (EROS), a new impurity solver for the single impurity Anderson model, [arXiv:0810.3302 \[cond-mat.str-el\]](https://arxiv.org/abs/0810.3302) (2008).
- [47] A. Auerbach, Hall number of strongly correlated metals, *Phys. Rev. Lett.* **121**, 066601 (2018).
- [48] A. Auerbach, Equilibrium formulae for transverse magnetotransport of strongly correlated metals, *Phys. Rev. B* **99**, 115115 (2019).
- [49] A. Foley, Liouvillian recursion method for the electronic Green's function, (2024), [arXiv:2401.02527 \[cond-mat.str-el\]](https://arxiv.org/abs/2401.02527).
- [50] M.-D. Choi, Positive linear maps on C^* -algebras, *Canadian Journal of Mathematics* **24**, 520–529 (1972).
- [51] A. Jamiołkowski, Linear transformations which preserve trace and positive semidefiniteness of operators, *Reports on Mathematical Physics* **3**, 275 (1972).
- [52] To keep the notation simple in the main text, we assumed $U(1)$ charge symmetry, i.e. the absence of superconductivity. As a result, we focused on representing \mathcal{L} in \mathbb{W}_1 , the dynamically relevant subspace of operators with charge $+1$. The representation of \mathcal{L} in \mathbb{W}_{-1} , the dynamically relevant space of operators with charge -1 , follows from $[H, c_\alpha^\dagger]^\dagger = -[H, c_\alpha]$. In the presence of mean-field superconductivity, H_{int} also contains $c^\dagger c^\dagger$ and cc terms. Then, the block of single-particle operators has to be extended to include both creation and annihilation operators, $|\mathbf{c}^\dagger, \mathbf{c}\rangle = (|c_1^\dagger\rangle, \dots, |c_M^\dagger\rangle, |c_1\rangle, \dots, |c_M\rangle)$, since both the Green's function and self-energy will exhibit non-zero anomalous components. With this generalization, the strategy described in our paper can also be applied in the presence of mean-field superconductivity.
- [53] For a simple example of charge-1 operators that are not in \mathbb{W}_1 , consider a free-fermion system. Since its Hamiltonian is quadratic, acting with \mathcal{L} on single-particle operators again yields single-particle operators. Thus $\mathbb{W}_c = \mathbb{W}_1$ and the single-particle irreducible subspace $\mathbb{W}_{\bar{c}}$ is empty. Therefore, any operator with charge $+1$ that is not single-particle, e.g. $|c_\alpha^\dagger c_\beta c_\gamma^\dagger\rangle$, is not in \mathbb{W}_1 .
- [54] Here, we exploited the fact that exchange symmetry requires $U_{\alpha\gamma, \delta\beta} = -U_{\gamma\alpha, \delta\beta} = U_{\gamma\alpha, \beta\delta}$.
- [55] E. Koch, The Lanczos method, in *The LDA+DMFT approach to strongly correlated materials*, *Forschungszentrum Jülich*, edited by E. Pavarini, E. Koch, D. Vollhardt, and A. Lichtenstein (2011).
- [56] C. Lanczos, An iteration method for the solution of the eigenvalue problem of linear differential and integral operators, *Journal of Research of the National Bureau of Standards* **45**, 255 (1950).
- [57] D. Boley and G. Golub, The Lanczos-Arnoldi algorithm and controllability, *Systems & Control Letters* **4**, 317 (1984).
- [58] G. Pinna, O. Lunt, and C. von Keyserlingk, Approximation theory for Green's functions via the Lanczos algorithm, (2025), [arXiv:2505.00089 \[quant-ph\]](https://arxiv.org/abs/2505.00089).

- [59] F. B. Kugler, Improved estimator for numerical renormalization group calculations of the self-energy, *Phys. Rev. B* **105**, 245132 (2022).
- [60] A. Zacinskas, M. Pelz, F. T. Ebel, F. Kugler, J. von Delft, K. Held, M. Haverkort, and A. Gleis, Symmetric estimator for discrete self-energy of discretized quantum impurity models, to be published.
- [61] B. Bruognolo, N.-O. Linden, F. Schwarz, S.-S. B. Lee, K. Stadler, A. Weichselbaum, M. Vojta, F. B. Anders, and J. von Delft, Open Wilson chains for quantum impurity models: Keeping track of all bath modes, *Phys. Rev. B* **95**, 121115 (2017).
- [62] M. Ferrero, P. S. Cornaglia, L. De Leo, O. Parcollet, G. Kotliar, and A. Georges, Pseudogap opening and formation of Fermi arcs as an orbital-selective Mott transition in momentum space, *Phys. Rev. B* **80**, 064501 (2009).
- [63] S. Okamoto, A. J. Millis, H. Monien, and A. Fuhrmann, Fictive impurity models: An alternative formulation of the cluster dynamical mean-field method, *Phys. Rev. B* **68**, 195121 (2003).
- [64] O. Kovalska, J. von Delft, and A. Gleis, [Tangent space krylov computation of real-frequency spectral functions: Influence of density-assisted hopping on 2d mott physics](#) (2025), [arXiv:2510.07279 \[cond-mat.str-el\]](#).
- [65] I. de Vega, U. Schollwöck, and F. A. Wolf, How to discretize a quantum bath for real-time evolution, *Phys. Rev. B* **92**, 155126 (2015).
- [66] F. B. Kugler, Improved estimator for numerical renormalization group calculations of the self-energy, *Phys. Rev. B* **105**, 245132 (2022).
- [67] M. Pelz, A. Gleis, and J. von Delft, Quantum criticality in the two dimensional hubbard model, to be published.
- [68] E. Gull, M. Ferrero, O. Parcollet, A. Georges, and A. J. Millis, Momentum-space anisotropy and pseudogaps: A comparative cluster dynamical mean-field analysis of the doping-driven metal-insulator transition in the two-dimensional Hubbard model, *Phys. Rev. B* **82**, 155101 (2010).
- [69] S.-S. B. Lee and A. Weichselbaum, Adaptive broadening to improve spectral resolution in the numerical renormalization group, *Phys. Rev. B* **94**, 235127 (2016).
- [70] S.-S. B. Lee, J. von Delft, and A. Weichselbaum, Doublon-holon origin of the subpeaks at the Hubbard band edges, *Phys. Rev. Lett.* **119**, 236402 (2017).
- [71] K. G. Wilson, The renormalization group: Critical phenomena and the Kondo problem, *Rev. Mod. Phys.* **47**, 773 (1975).
- [72] H. R. Krishna-murthy, J. W. Wilkins, and K. G. Wilson, Renormalization-group approach to the Anderson model of dilute magnetic alloys. I. Static properties for the symmetric case, *Phys. Rev. B* **21**, 1003 (1980).
- [73] F. B. Anders and A. Schiller, Real-time dynamics in quantum-impurity systems: A time-dependent numerical renormalization-group approach, *Phys. Rev. Lett.* **95**, 196801 (2005).
- [74] R. Bulla, T. A. Costi, and T. Pruschke, Numerical renormalization group method for quantum impurity systems, *Rev. Mod. Phys.* **80**, 395 (2008).
- [75] A. Weichselbaum, Non-Abelian symmetries in tensor networks: A quantum symmetry space approach, *Annals of Physics* **327**, 2972 (2012).
- [76] A. Weichselbaum, Tensor networks and the numerical renormalization group, *Phys. Rev. B* **86**, 245124 (2012).
- [77] A. Weichselbaum, X-symbols for non-Abelian symmetries in tensor networks, *Phys. Rev. Res.* **2**, 023385 (2020).
- [78] A. Weichselbaum, QSpace - An open-source tensor library for Abelian and non-Abelian symmetries, *SciPost Phys. Codebases* , 40 (2024).
- [79] A. Weichselbaum, Codebase release 4.0 for QSpace, *SciPost Phys. Codebases* , 40 (2024).
- [80] A. K. Mitchell, M. R. Galpin, S. Wilson-Fletcher, D. E. Logan, and R. Bulla, Generalized wilson chain for solving multichannel quantum impurity problems, *Phys. Rev. B* **89**, 121105 (2014).
- [81] K. M. Stadler, A. K. Mitchell, J. von Delft, and A. Weichselbaum, Interleaved numerical renormalization group as an efficient multiband impurity solver, *Phys. Rev. B* **93**, 235101 (2016).
- [82] N. Wagner, L. Crippa, A. Amaricci, P. Hansmann, M. Klett, E. J. König, T. Schäfer, D. D. Sante, J. Cano, A. J. Millis, A. Georges, and G. Sangiovanni, Mott insulators with boundary zeros, *Nature Communications* **14**, 7531 (2023).
- [83] P. Pudleiner, T. Schäfer, D. Rost, G. Li, K. Held, and N. Blümer, Momentum structure of the self-energy and its parametrization for the two-dimensional Hubbard model, *Phys. Rev. B* **93**, 195134 (2016).
- [84] P. Worm, M. Reitner, K. Held, and A. Toschi, Fermi and luttinger arcs: Two concepts, realized on one surface, *Phys. Rev. Lett.* **133**, 166501 (2024).
- [85] S. Backes, J.-H. Sim, and S. Biermann, Nonlocal correlation effects in fermionic many-body systems: Overcoming the noncausality problem, *Phys. Rev. B* **105**, 245115 (2022).
- [86] M. E. H. Ismail, *Classical and quantum orthogonal polynomials in one variable*, edited by W. V. Assche, Encyclopedia of mathematics and its applications No. 98 (Cambridge University Press, Cambridge ;, 2005) includes bibliographical references (p. [661]-696) and indexes.
- [87] G. Szegő, *Orthogonal polynomials*, online-ausg. ed., AMS ebook collection (American mathematical society, New York city, 2012) "List of references": p. 378-393. - Electronic reproduction; Providence, Rhode Island; American Mathematical Society; 2012. - Description based on print version record.
- [88] T. S. Chihara, *An introduction to orthogonal polynomials*, first published ed. (Dover Publications, Inc., Mineola, 2011) this Dover edition, first published in 2011, is an unabridged republication of the work originally published in 17978 by Gordon and Breach, Science Publisher, Inc., New York.
- [89] B. Simon, *Orthogonal polynomials on the unit circle*, Colloquium Publications No. Volume 54, Part 1 (American Mathematical Society, Providence, Rhode Island, 2005) includes bibliographical references and indexes. Description based on online resource; title from PDF title page (ebrary, viewed April 11, 2017).
- [90] N. I. Achiezer, *The classical moment problem and some related questions in analysis*, edited by N. Kemmer, Classics in applied mathematics No. 82 (Society for Industrial and Applied Mathematics, Philadelphia, Pennsylvania, 2021).
- [91] J. M. Stojanov, *Counterexamples in probability*, 3rd ed., Dover books on mathematics (Dover Publ., Mineola, NY, 2014) includes bibliographical references (pages

- 317-364) and index.
- [92] N. Dunford and J. T. Schwartz, *Linear Operators, Part 2: Spectral Theory, Self Adjoint Operators in Hilbert Space*, Vol. 2 (Wiley Interscience Publ., New York, 1988).
- [93] A. J. Duran, On orthogonal polynomials with respect to a positive definite matrix of measures, *Canadian Journal of Mathematics* **47**, 88 (1995).
- [94] T. S. Chihara, Hamburger moment problems and orthogonal polynomials, *Transactions of the American Mathematical Society* **315**, 189 (1989).
- [95] B. Simon, The classical moment problem as a self-adjoint finite difference operator, *Advances in Mathematics* **137**, 82 (1998).
- [96] A. J. Duran and P. Lopez-Rodriguez, N-extremal matrices of measures for an indeterminate matrix moment problem, *Journal of Functional Analysis* **174**, 301 (2000).
- [97] P. Lopez-Rodriguez, The Nevanlinna parametrization for a matrix moment problem, *Mathematica Scandinavica* **89**, 245 (2001).
- [98] D. Damanik, A. Pushnitski, and B. Simon, *The analytic theory of matrix orthogonal polynomials* (2008), [arXiv:0711.2703 \[math.CA\]](https://arxiv.org/abs/0711.2703).
- [99] C. Berg, Indeterminate moment problems and the theory of entire functions, *Journal of Computational and Applied Mathematics* **65**, 27 (1995).
- [100] S. L. Altmann and A. P. Cracknell, Lattice harmonics I. Cubic groups, *Rev. Mod. Phys.* **37**, 19 (1965).
- [101] S. L. Altmann and C. J. Bradley, Lattice harmonics ii. hexagonal close-packed lattice, *Rev. Mod. Phys.* **37**, 33 (1965).
- [102] A. Foley, S. Verret, A.-M. S. Tremblay, and D. Sénéchal, Coexistence of superconductivity and antiferromagnetism in the Hubbard model for cuprates, *Phys. Rev. B* **99**, 184510 (2019).
- [103] Y. Lu, M. Höppner, O. Gunnarsson, and M. W. Haverkort, Efficient real-frequency solver for dynamical mean-field theory, *Phys. Rev. B* **90**, 085102 (2014).
- [104] F. D. Picoli, M. Huang, A. Gleis, and J. von Delft, Tangent-space krylov solver for quantum impurity models, to be published.
- [105] S. R. White, Density matrix formulation for quantum renormalization groups, *Phys. Rev. Lett.* **69**, 2863 (1992).
- [106] U. Schollwöck, The density-matrix renormalization group in the age of matrix product states, *Annals of Physics* **326**, 96 (2011), january 2011 Special Issue.
- [107] A. Gleis, J.-W. Li, and J. von Delft, Projector formalism for kept and discarded spaces of matrix product states, *Phys. Rev. B* **106**, 195138 (2022).
- [108] A. Gleis, J.-W. Li, and J. von Delft, Controlled bond expansion for density matrix renormalization group ground state search at single-site costs, *Phys. Rev. Lett.* **130**, 246402 (2023).
- [109] A. Gleis, J.-W. Li, and J. von Delft, *Reply to comment on "controlled bond expansion for density matrix renormalization group ground state search at single-site costs"* (2025), [arXiv:2501.12291 \[cond-mat.str-el\]](https://arxiv.org/abs/2501.12291).
- [110] C. J. Bolech, S. S. Kancharla, and G. Kotliar, Cellular dynamical mean-field theory for the one-dimensional extended hubbard model, *Phys. Rev. B* **67**, 075110 (2003).
- [111] L. Kohn and G. E. Santoro, Quench dynamics of the anderson impurity model at finite temperature using matrix product states: entanglement and bath dynamics, *Journal of Statistical Mechanics: Theory and Experiment* **2022**, 063102 (2022).
- [112] J. Haegeman, J. I. Cirac, T. J. Osborne, I. Pizorn, H. Verschelde, and F. Verstraete, Time-dependent variational principle for quantum lattices, *Phys. Rev. Lett.* **107**, 070601 (2011).
- [113] J.-W. Li, A. Gleis, and J. von Delft, Time-dependent variational principle with controlled bond expansion for matrix product states, *Phys. Rev. Lett.* **133**, 026401 (2024).